

# **Critical Phenomena in Bilayer Excitonic Condensates**

**Von der Fakultät Mathematik und Physik der Universität Stuttgart zur  
Erlangung der Würde eines Doktors der Naturwissenschaften  
(Dr. rer. nat.) genehmigte Abhandlung**

**von**

**XUTING HUANG**

**geboren am 20.12.1982  
in Guang Dong, China**

<b>Hauptberichter:</b>	<b>Prof. Dr. Klaus VON KLITZING</b>
<b>Mitberichter:</b>	<b>Prof. Dr. Tilman PFAU</b>
<b>Vorsitzender:</b>	<b>Prof. Dr. Alejandro MURAMATSU</b>
<b>Tag der mündlichen Prüfung:</b>	<b>20. Dezember 2012</b>

**MAX-PLANCK-INSTITUT FÜR FESTKÖRPERFORSCHUNG  
STUTTGART, 2012**



# Contents

<b>Abbreviations, Symbols and Physical Constants</b>	<b>7</b>
<b>1 Introduction</b>	<b>11</b>
<b>2 Quantum Hall Effects</b>	<b>15</b>
2.1 Integer Quantum Hall Effect . . . . .	15
2.1.1 Transport in Electromagnetic Fields . . . . .	15
2.1.2 Quantized Hall Resistances . . . . .	18
2.1.3 Current-Induced Breakdown of the IQHE . . . . .	24
2.2 Fractional Quantum Hall Effect . . . . .	28
<b>3 Bilayer Quantum Hall State at <math>\nu_T = 1</math></b>	<b>31</b>
3.1 Electron Bilayer Systems . . . . .	31
3.2 Correlated $\nu_T = 1$ State in Weakly Coupled Bilayers . . . . .	33
3.2.1 $\nu_T = 1$ Ground State . . . . .	35
3.2.2 Low Energy Excitations . . . . .	39
3.3 Transport at the $\nu_T = 1$ State . . . . .	41
3.4 Critical Josephson Current at $\nu_T = 1$ . . . . .	46
<b>4 Quantum Hall Breakdown in Interlayer Tunneling</b>	<b>51</b>
4.1 Measurement Results . . . . .	51
4.2 Data Analysis and Discussion . . . . .	57
4.3 Conclusions . . . . .	67
<b>5 Josephson Currents in Corbino Bilayers</b>	<b>69</b>
5.1 Interlayer and Interedge Transport . . . . .	70
5.1.1 Measurement Results . . . . .	70
5.1.2 Data Analysis and Discussion . . . . .	72
5.2 Applying a Second Josephson Tunneling Current . . . . .	78
5.2.1 Measurement Results . . . . .	78

5.2.2	Data Analysis and Discussion . . . . .	81
5.3	Conclusions . . . . .	88
<b>6</b>	<b>Corbino-Counterflow at the <math>\nu_T = 1</math> State</b>	<b>91</b>
6.1	Series Counterflow . . . . .	92
6.1.1	Measurement Results . . . . .	93
6.1.2	Data Analysis and Discussion . . . . .	93
6.2	Drag Counterflow . . . . .	98
6.2.1	Measurement Results . . . . .	98
6.2.2	Data Analysis and Discussion . . . . .	99
6.3	Conclusions . . . . .	108
<b>7</b>	<b>Summary</b>	<b>111</b>
<b>8</b>	<b>Deutsche Zusammenfassung</b>	<b>115</b>
<b>A</b>	<b>Additional Measurements</b>	<b>119</b>
<b>B</b>	<b>Sample Fabrication and Measurement Setup</b>	<b>125</b>
B.1	Sample Fabrication . . . . .	125
B.1.1	Sample Structure . . . . .	125
B.1.2	Fabrication Process . . . . .	126
B.2	Measurement Setup . . . . .	132
B.3	Sample Fabrication Parameters . . . . .	137
B.4	Wafer Growth Parameters . . . . .	137
<b>C</b>	<b>Calculation of <math>\Delta_{SAS}</math></b>	<b>141</b>
	<b>References</b>	<b>146</b>

Der erste Trunk aus dem Becher der Naturwissenschaft macht  
atheistisch, aber auf dem Grund des Bechers wartet Gott.

Werner Heisenberg (1901-1976), deutscher Physiker



# Abbreviations, symbols and physical constants

2DES	two-dimensional electronsystem
2DEG	two-dimensional electrongas
$\tau$	scattering time
$e$	electron charge
$m$	electron mass
$m^*$	effective electron mass
$n_e$	electron density
<b>E</b>	electric field strength
<b>B</b>	magnetic field strength
$\mathbf{e}_{i=x,y,z}$	unit vector in x,y,z direction
<b>p</b>	momentum
$\omega_c$	cyclotron frequency
$E_c$	cyclotron energy
$\sigma$	conductivity
$\sigma_0$	specific conductivity
$G$	conductance
$G_0$	conductance at B=0
$\Gamma$	level broadening
$\rho$	resistivity
GaAs	gallium arsenide
AlAs	aluminum arsenide
AlGaAs	aluminum gallium arsenide
$R_{xx}$	longitudinal resistance
$R_{xy}$	transversal resistance
$R_H$	Hall resistance
$\mu$	mobility
DOS	density of states

$\Phi$	total electron wave function
A	magnetic flux
$\varepsilon_i$	confinement energy of the i-th level
$k_B$	Boltzmann constant
$\nu$	filling factor
$\nu_T$	total filling factor
$E_F$	Fermi level
$v_F$	Fermi velocity
$\lambda$	wave length
QHE	quantized Hall effect
IQHE	integer quantized Hall effect
FQHE	fractional quantized Hall effect
MBE	Molecular Beam Epitaxy
$ \uparrow\rangle,  \downarrow\rangle$	spin-up, spin-down wave function
$\Delta_{SAS}$	symmetric-antisymmetric energy gap
$E_C$	Coulomb energy
$E_{inter}$	interlayer energy
$E_{intra}$	intralayer energy
d	interlayer spacing
$l_B$	magnetic length
$\Delta$	activation energy gap (of a QHE)
BCS	Bardeen-Cooper-Schrieffer model
BEC	Bose-Einstein condensate
$E_Z$	Zeeman energy
QHF	quantum Hall ferromagnetism
KT	Kosterlitz-Thouless (transition)
$T_{KT}$	Kosterlitz-Thouless transition temperature
$\rho_s$	pseudospin stiffness
$B_{\perp}$	perpendicular magnetic field
$B_{\parallel}$	parallel magnetic field
$I_c$	critical current
DC	direct current
AC	alternating current
$\xi$	coherence length
$\lambda_J$	Josephson length
$I_t$	tunneling current
$I^{EX}$	excitonic counterflow current



---

$I^{QP}$	quasi-particle current
$L_d$	size of coherent domain
$\epsilon$	dielectric constant
LC	inductor-capacitor circuit
HB	Hall bar
CR	Corbino ring
I-V	current voltage (characteristic)
$I_{drive}$	current flowing through the drive layer
$I_{drag}$	current flowing through the drag layer
$I_S$	layer symmetric current
$I_{AS}$	layer antisymmetric current
$I_{total}$	total current
AR	Andreev-reflection
$I_{in}$	current measured at the inner edge
$I_{out}$	current measured at the outer edge
NDR	negative differential resistance
$I_R$	current detected using a shunt resistance
$I_{GND}$	current flowing to the ground
$I^{TU}$	interlayer tunneling current
$I_{cir}$	circular current
$V_{interedge}$	intralayer voltage between the outer and inner edge of a Corbino ring device
FFP	Fronius-Fischer-Ploog etching method
MOCVD	Metal-Oxide Chemical Vapor Deposition
LT-GaAs	low temperature GaAs
PMMA	Poly(methyl methacrylate)
$He^3$	helium-III
$He^4$	helium-IV



# Chapter 1

## Introduction

The revolution of physics from the classical to quantum mechanical view angle, ignited by a number of discoveries from the past century such as the photoelectric effect by Heinrich Hertz as well as the quantum hypothesis by Max Planck, has continued to flourish in the second half of the 20th century. One of the most intensively studied topics is the phenomenon of spontaneous symmetry breaking, which is present in both particle physics and condensed matter physics. In particle physics, the most prominent example is the mechanism leading to the prediction of a gauge boson called Higgs boson, which should give the exchange bosons for the weak interaction, the W and Z bosons, their mass. In condensed matter physics, a similar spontaneous symmetry breaking is observed in ferromagnetism and superconductivity. When a ferromagnet is cooled down to below its Curie temperature, the magnetic moments are aligned giving rise to a finite magnetization and the rotational symmetry to any axis perpendicular to the direction of magnetization is spontaneously broken. In superconductivity, similar effect occurs when a collective field breaks the electromagnetic gauge symmetry and gives rise to the superconducting energy gap.

There is also another type of symmetry breaking which leads to formation of energy gaps. In two-dimensional charge systems, the most prominent effect is the quantized Hall effect which arises due to the breaking of time-reversal symmetry: the Lorentz-force acting on traveling charge carriers turns the cyclotron orbit in two different directions under time-reversal. Further examples include topological insulators, the quantum Spin Hall effect and the anticipated quantum anomalous Hall effect.

Strikingly, spontaneous symmetry breaking can also lead to an effect which combines some of the effects above: in closely spaced double quantum well systems, interlayer coherence can be induced when adjusting the Coulomb interaction within each layer to be similar to that between the two layers. This can be done by controlling the magnetic field, the charge carrier density in both layers as well as by the distance between the layers. At the state, in which both quantum wells exhibit a filling factor of  $\frac{1}{2}$ , a quantum Hall state of the combined filling factor  $\nu_T =$

1 is formed. In terms of the pseudospin, a *which layer* degree of freedom assigned to each electron in the bilayers, the pseudospin vectors are aligned in the system's ground state, forming a pseudospin quantum Hall ferromagnet. Since the quantum wells are half-filled, occupied and vacant states can also be thought as indirect conduction band excitons which are condensed into a BCS-like condensate giving rise to a Josephson-like interlayer tunneling up to a critical current, strongly resembling the Josephson junctions of conventional superconductors.

In this work, phenomena concerning the critical currents, both out of plane and in the plane, are studied in double-well structures. After this introductory chapter, the rest of this thesis is structured as follows:

- Chap. 2 introduces the physics of two-dimensional electron systems (2DES) and the integer quantum Hall effect. Starting with the classical Drude model, the edge state picture will be discussed in detail under the light of Landau quantization. It will be extended by distinguishing between the compressible and the incompressible strips of a 2DEG, which results in different Hall potential distribution of a single quantum Hall plateau. This chapter is terminated with the fractional quantum Hall effect.
- Chap. 3 gives an introduction to the underlying theory of the ground state as well as low energy excited states of the  $\nu_T = 1$  bilayer state. Three types of ground state wave functions, which are mathematically equivalent, will be presented. In the low energy excitations, the concept of merons will be introduced. Finally, different types of transport including the interlayer tunneling, in-plane transport and excitonic counterflow will be discussed.
- Chap. 4 opens the experimental part of this thesis and deals with the interplay between the quantum Hall breakdown and the Josephson-like interlayer tunneling. Three Hall bar samples which only differ in their interlayer spacing will be presented in terms of their critical Josephson currents. Two of them will be further investigated in order to clarify the role of in-plane transport in the interlayer tunneling.
- Chap. 5 uses Corbino ring devices to study the transport in different configurations. In particular, interlayer tunneling at different edges of one Corbino sample will be compared in order to study the effect of edge and area. Furthermore, two Josephson interlayer currents will be applied simultaneously to investigate the interplay between these two circuits which are separated.
- Chap. 6 presents two measurement setups to study the excitonic counterflow at  $\nu_T = 1$ : series and drag counterflow. For series counterflow, one Corbino sample is used while two Corbino samples are used for the drag counterflow, from which one sample will be tilted in order to introduce a parallel magnetic field component on the 2DES.

These chapters are followed by a summarizing chapter which also points at existing questions and further possibilities to complete the understanding of this topic. Three appendices are provided for interested readers to know about the materials and fabrication procedures used in this work in more details.

The results from this thesis can be partially found in the following publication:

- X. Huang, W. Dietsche, M. Hauser, and K. von Klitzing, *Coupling of Josephson Currents in Quantum Hall Bilayers*, Phys. Rev. Lett. 109, 156802 (2012)



# Chapter 2

## Quantum Hall Effects

### 2.1 Integer Quantum Hall Effect

#### 2.1.1 Transport in Electromagnetic Fields

The transport phenomena of electrons in two-dimensional systems are complex and will be approached starting with classical models. The Drude model gives both reasonable results for the classical Hall effect and useful information for the quantized case. Hence, it will be explained as an introduction into the physics of the QHE in the following. Then, in addition to the quantization of energy of motion perpendicular to the plane of the 2DES, the electronic states are quantized into discrete levels at high magnetic fields. This quantization greatly affects the charge transport.

#### Drude Model

A typical conductor with a rectangular geometry with length  $L$ , width  $W$  and thickness  $d$ , is shown in Fig. 2.1. In the Drude model, electrons are treated as quasi-free massive particles with vanishing size. Interactions between electrons and the crystal environment such as scattering processes with charged impurities, crystal defects as well as phonons are included through the scattering time  $\tau$ , a phenomenological quantity which denotes the average time between two collisions of an electron with the above mentioned scattering centers. Electron-electron interactions are not taken into account.

By applying this model to an electron with charge  $-e$  and effective mass  $m^*$  in a conductor with electron density  $n_e$ , the equation of motion in a uniform electric field  $\mathbf{E} = E\mathbf{e}_x$  and a uniform magnetic field  $\mathbf{B} = B\mathbf{e}_z$  can be written in the following form

$$\mathbf{F} = \left( \frac{d\mathbf{p}}{dt} \right)_{scattering} + \left( \frac{d\mathbf{p}}{dt} \right)_{fields} = \frac{m\mathbf{v}}{\tau} - e(\mathbf{E} + \mathbf{v} \times \mathbf{B}) \quad (2.1)$$

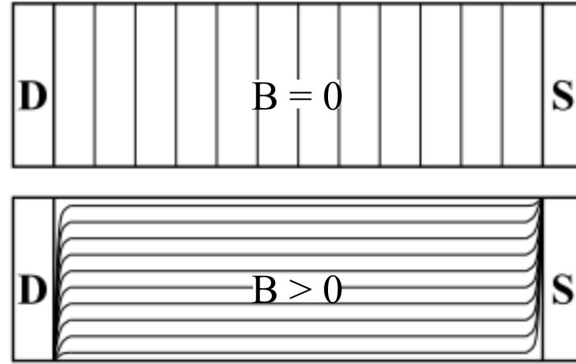


**Fig. 2.1:** Typical Hall bar sample with length  $L$  and width  $W$ . Upper panel: at vanishing magnetic fields, the equipotential lines point in the direction perpendicular to current; lower panel: at sufficiently large magnetic fields (i.e. in the quantum regime characterized by  $\omega_c\tau \ll 1$ ), the equipotential lines point in the direction parallel to current and merge at the hot spots.

which yields under the equilibrium condition  $\frac{d}{dt}\langle\mathbf{v}\rangle = 0$  a solution in matrix form

$$\begin{pmatrix} E_x \\ E_y \end{pmatrix} = \begin{bmatrix} m/e\tau & -B \\ B & m/e\tau \end{bmatrix} \begin{pmatrix} v_x \\ v_y \end{pmatrix}. \quad (2.2)$$

Using the cyclotron frequency  $\omega_c = \frac{eB}{m^*}$ <sup>1</sup>, together with the specific conductivity  $\sigma_0 = \frac{e^2 n_e \tau}{m^*}$  and the current density  $\mathbf{j} = e\langle\mathbf{v}\rangle n_e$ , Eq. 2.2 can be rewritten in the form of the Ohm's law  $\mathbf{E} = \rho\mathbf{j}$  with the resistivity tensor<sup>2</sup>  $\rho$

$$\begin{pmatrix} E_x \\ E_y \end{pmatrix} = \underbrace{\sigma_0^{-1} \begin{bmatrix} 1 & -\omega_c\tau \\ \omega_c\tau & 1 \end{bmatrix}}_{\equiv \rho} \begin{pmatrix} j_x \\ j_y \end{pmatrix}. \quad (2.3)$$

The  $x$ -component of the electric field drives a steady current in the  $x$  direction along the strip and a  $y$ -component of  $\mathbf{E}$  must appear to balance the Lorentz force on the electron. In this equilibrium, the current can only flow in the  $x$ -direction, hence  $j_y = 0$ . Matrix multiplication therefore yields

$$E_y = \frac{1}{n_e e} B j_x \equiv R_H B j_x, \quad (2.4)$$

<sup>1</sup>For the simplified case, i.e. the Fermi surface is assumed to be a sphere, the cyclotron mass is approximately equal to the effective mass. This is valid for GaAs.

<sup>2</sup>Under matrix inversion  $\rho = \sigma^{-1}$ , one can also formulate the Ohm's law  $\mathbf{j} = \sigma\mathbf{E}$  using the conductivity tensor

$$\sigma = \sigma_0 \begin{bmatrix} \frac{1}{1+\omega_c^2\tau^2} & \frac{\omega_c\tau}{1+\omega_c^2\tau^2} \\ -\frac{\omega_c\tau}{1+\omega_c^2\tau^2} & \frac{1}{1+\omega_c^2\tau^2} \end{bmatrix}.$$



which means that the transverse electric field is proportional to the current applied in the longitudinal direction and the perpendicular magnetic field via a coefficient called Hall constant. Experimentally, the Hall constant can be determined using the Hall bar geometry by measuring the dependence of the transverse resistance  $R_{xy}$  on the magnetic field, since

$$R_{xy} = \frac{V_H}{I} = R_H B. \quad (2.5)$$

Eq. 2.4 and Eq. 2.5 give the two-dimensional electron density

$$n_e = \frac{IB}{V_H e}. \quad (2.6)$$

On the other hand, the measurement of the longitudinal resistance gives

$$R_{xx} = \frac{V_L}{I} = \frac{L}{W} \rho_{xx} = \frac{L}{n_e e \mu W}. \quad (2.7)$$

Here,  $\mu = \frac{e\tau}{m^*}$  is the mobility of the electron in the conductor and can be calculated from Eq. 2.7. For the case  $\omega_c \tau \ll 1$ , one has  $\sigma_{xx} = \frac{1}{\sigma_0} = \frac{1}{\rho_{xx}}$  and  $\sigma_{xy} = -\sigma_0^2 \rho_{yx}$ . However, this does not hold for  $\omega_c \tau \gg 1$ , where

$$\sigma_{xx} \rightarrow \frac{\sigma_0}{(\omega_c \tau)^2} = \left( \frac{en_e}{B} \right)^2 \frac{1}{\sigma_0} \propto \rho_{xx} \quad (2.8)$$

$$\sigma_{xy} = -\rho_{yx}^{-1} = \frac{en_e}{B} \quad (2.9)$$

Large magnetic fields also lead to the change in the distribution of the equipotential lines. At low or zero magnetic field, as shown in the upper panel of Fig. 2.1, the equipotential lines align in the direction perpendicular to the current flow. At high magnetic fields, the electron trajectory is determined rather by the magnetic field than by the electric field between source and drain, which in the case of finite sample width leads to a large Hall voltage. Thus  $j_y = 0$  can no longer be assumed for the whole sample when solving the equation of motion. The equipotential lines in this case will look like illustrated in the lower panel of Fig. 2.1. Almost all the equipotential lines merge together and become dense at the corners of the sample called *hot spots*, which have been experimentally observed [1]. In this case, the source-drain voltage becomes equal to the Hall voltage ( $U_H = U_{SD}$ ).

## Corbino Effect

The classical Hall effect has been not only observed in a rectangular or topologically equivalent devices, but also in a conductor with a disk geometry. Fig. 2.2 illustrates such a device. Without magnetic field, a voltage difference between the two edges leads to a pure radial current. In presence of a magnetic field perpendicular to the plane of the disk, the Lorentz force will bend

the electron trajectory to form spiral paths before the electrons reach the drain side. When the magnetic field is strong enough ( $\omega_c\tau \gg 1$ ), almost no radial current flows anymore between the two edges but a circular current is assumed to flow within the disk which is associated with the Hall constant via Eq. 2.5 [2]. While in a rectangular (Hall bar) device the resistivity can be measured, a Corbino disk provides information about the conductivity in the longitudinal direction,  $\sigma_{xx}$ , thus a complementary method to study the magnetotransport.

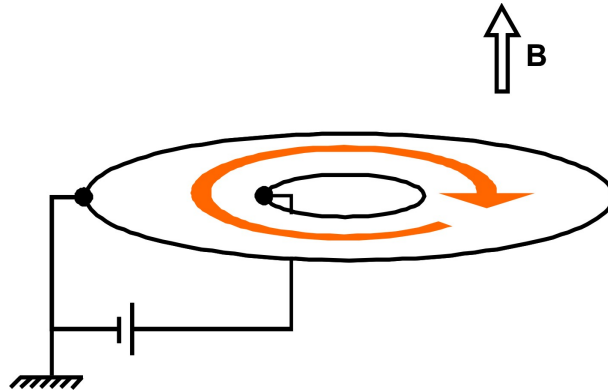


**Fig. 2.2:** The Corbino effect in a conductor with disk geometry. Applying a bias voltage between the two edges will give rise to a circulating current (red) when a perpendicular magnetic field is applied.

### 2.1.2 Quantized Hall Resistances

In two-dimensional systems, when probing the longitudinal resistivity of a Hall bar under varied magnetic field and low temperatures, one can observe resistivity minima which go down to almost zero and are separated by finite magneto resistance. The finite magneto resistance is known as the Shubnikov-de Haas oscillation while the resistivity minima, which coincide with the quantized transversal (Hall) resistance, is characteristic of the quantum Hall effect. In the following, the physical origin of the quantization of Hall resistance—the Landau quantization, will be explained. This will be extended by the effects of disorder-induced localization as well as electron–electron interaction. Finally, a brief introduction will be given on the breakdown of the integer quantum Hall effect.

#### Landau Quantization

In order to study the effects of high magnetic fields on the electron transport in a 2D system, it is essential to calculate the electronic density of states (DOS) under such a magnetic field quantum mechanically. When electrons are brought into a 2DES—heterostructures or quantum wells, their

motion is confined in the growth direction, which leads to a case similar to the *particle in a box*, as shown in Fig. 2.3.

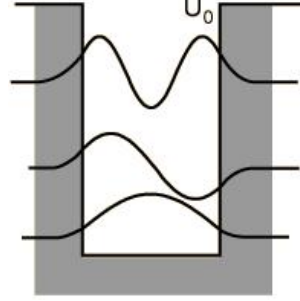


**Fig. 2.3:** Particle in a box with a finite wall height. The wave functions correspond to the subbands' confinement energies.

The Schrödinger-equation for an electron in a 2DES in an external magnetic field  $\mathbf{B} = \nabla \times \mathbf{A}$  is

$$\hat{H}\Phi = \left[ -\frac{\hbar^2}{2m^*} \left( \nabla - \frac{e\mathbf{A}}{i\hbar} \right)^2 \right] \Phi = E\Phi \quad (2.10)$$

For a perpendicular magnetic field  $\mathbf{B} = B\mathbf{e}_z$ , the vector potential  $\mathbf{A}$  can be written using the Landau gauge as  $\mathbf{A} = (0, Bx, 0)$ . It is intuitive to separate the motion along the  $z$  axis from that within the  $xy$  plane, which yields the following electronic wave function

$$\Phi(x, y, z) = \zeta(x, y)\xi(z) \quad (2.11)$$

Eq. 2.10 can thus be separated into an equation concerning the  $z$  motion and a second one concerning the  $xy$  motion. Taking into account the boundary conditions for the  $z$  motion under the assumption of infinite barrier potentials, i.e.  $\xi_{z=0} = \xi_{z=d} = 0$ , the solution to the Schrödinger equation for the  $z$ -motion are the standing waves in this direction with quantized energy eigenvalues (subbands)

$$\varepsilon_i = \frac{\hbar^2 \pi^2 i^2}{2m^* d^2} \quad (2.12)$$

Here,  $i$  denotes the index of the confinement energy level. At low temperatures, the electron motion is nearly completely quenched along the  $z$  direction due to the large distance between the Fermi level and the second subband relative to the thermal energy given by  $k_B T$ <sup>1</sup>. This

<sup>1</sup>For a GaAs quantum well with  $m^* = 0.067m_0$  ( $m_0$  is the mass of a free electron) and a width of 10 nm, the energy distance between the ground state and the second subband corresponds to a temperature of nearly 2000 K.

gives rise to a 2DES even though the quantum well is non-ideal by having a finite thickness. With the Landau gauge, the wave function for the  $xy$  motion can be written in the form

$$\zeta(x, y) = e^{-ik_y y} \psi(x). \quad (2.13)$$

Under the substitution  $x_0 \equiv \frac{\hbar k_y}{eB}$ , Eq. 2.13 transforms the Schrödinger equation for  $x$  and  $y$  into a one-dimensional Schrödinger equation

$$-\frac{\hbar^2}{2m^*} \frac{\partial^2 \psi(x)}{\partial x^2} + \frac{m^*}{2} \omega_c^2 (x - x_0)^2 \psi(x) = E \psi(x). \quad (2.14)$$

This is the Schrödinger equation of a one-dimensional harmonic oscillator in which the potential is centered at  $x_0$ , which can be solved by a product of Hermitian polynomials and an exponential function as ansatz. The eigenvalues of Eq. 2.14 are the so-called Landau levels

$$\varepsilon_j = \hbar \omega_c \left( j + \frac{1}{2} \right) \quad (2.15)$$

with  $j$  as the quantum number of the Landau levels<sup>2</sup>. This means that the DOS in a 2D system under the magnetic field is no longer constant but discrete. The total energy of an electron is thus

$$E_{i,j} = \frac{\hbar^2 \pi^2 i^2}{2m^* d^2} + \hbar \omega_c \left( j + \frac{1}{2} \right). \quad (2.16)$$

Each Landau level can accommodate a certain number of electrons per unit area, which is equal to the number of magnetic flux quanta  $\phi_0 = \frac{h}{e}$  per unit area

$$n = \frac{B}{\phi_0} = \frac{eB}{h}. \quad (2.17)$$

Without taking the Zeeman-splitting into account, the filling factor  $\nu$ , which is defined as the number of fully occupied Landau levels, can be expressed as

$$\nu = \frac{n_e}{n} = \frac{n_e h}{eB}. \quad (2.18)$$

## Microscopic Picture

Soon after the quantized Hall effect was discovered by K. von Klitzing in 1980, efforts have been made to develop a theory to understand this effect. Büttiker et al. found that a model involving transport channels at the edges of a sample can elegantly explain the quantized Hall resistances [3]. This model takes into account that the Landau quantization leads to discrete energetic levels in the bulk. Such as illustrated in Fig. 2.4 b), such energy levels are bent at

<sup>2</sup>The Zeeman splitting due to electron spin isn't taken into account.

the sample edges and the number of current carrying edge channels corresponds to the number of fully occupied Landau levels in the bulk. It can be shown that one can elegantly reach the quantized values of Hall resistance in the frame of this picture.

Nevertheless, the edge channel picture is not reflecting any microscopic detail of the quantum Hall effect. In particular, it does not take into account how the Hall potential is distributed inside the 2DES. Hence, details about the current distribution within and beyond the quantum Hall plateaus is not discernable using this simplified picture.

In order to understand the quantized Hall effect at a microscopic level, local measurements deploying a scanning probe microscope (SPM) have been carried out to study the chemical potential of the 2DES at QHE [4]. From these measurements, it is concluded that the Hall potential distribution across the sample width (along the transversal axis) varies significantly, depending on the exact filling factor. In the mean time, the plateau values of the quantized Hall resistances remain unaffected (Fig. 2.5 a)). It is claimed that this effect is a consequence of the existence of compressible and incompressible strips running along the edges of the 2DES, which are predicted in several theoretical works [5] [6] [7].

The compressible/incompressible strips theory will be briefly explained in the following. Generally speaking, it takes not only the chemical potential but also the electrostatic potential, hence the electrochemical potential, into account. It is based on the assumption that the electrochemical potential,  $\mu_{elch}(\mathbf{r}) = -e\phi(\mathbf{r}) + \mu_{ch}(\mathbf{r})$ , is constant through the entire 2DES. Fig. 2.4 (d)-(e) shows the result of self-consistent calculation of the chemical, electrostatic potential as well as the density distribution in the vicinity of the edge of a 2DES. Compared to the result of single electron edge picture, shown in (a)-(c), the self-consistent result yields two alternating strips: the metal-like compressible and the insulator-like incompressible strips. The simplified physical explanation for the formation of such strips is that the electron density would rather undergo a gradual increase and then remain constant, thereby paying a small amount of chemical energy, than jumping abruptly which costs a considerable amount of electrostatic energy. In the incompressible region, the Landau levels below the Fermi energy are fully filled and the electrons cannot rearrange themselves to screen the electrostatic potential variations. As consequence, there is no conductivity in the direction of an electric field. In the compressible region, the Landau levels below the Fermi energy are only partially filled. Hence, the electrons can rearrange themselves at the Fermi energy, thus are able to screen any electrostatic potential variations, resulting in a flat electrostatic potential.

Now it will be shown that the quantized Hall resistances can be understood in the framework of the compressible/incompressible strips. Under the Hall condition which has been elaborated in Sec. 2.1.1, one has the relation

$$E_x(x) = \rho_H(x)j_y(x). \quad (2.19)$$

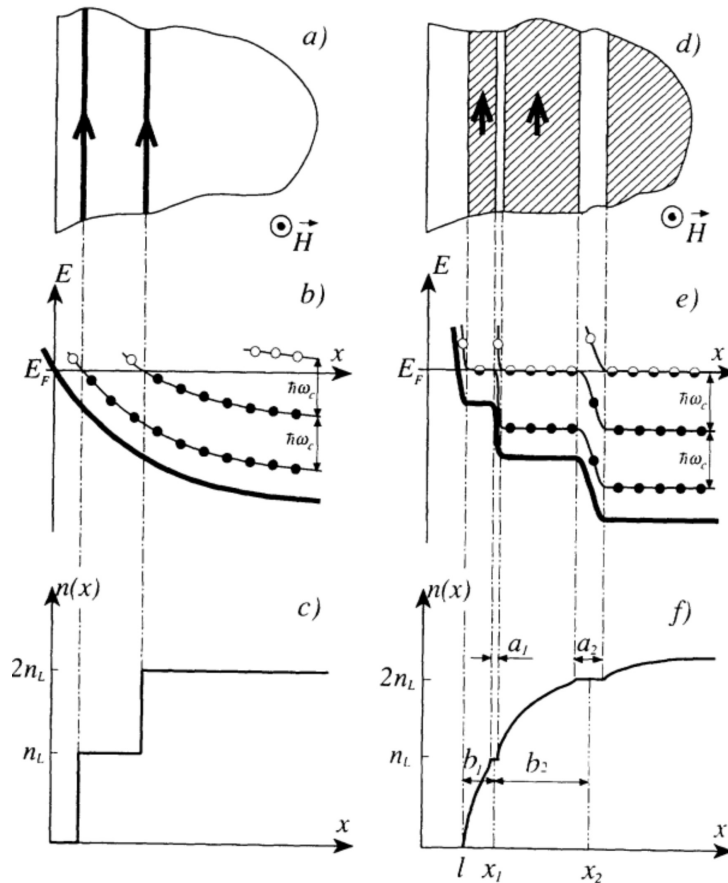


**Fig. 2.4:** Compressible and incompressible strips. (a-c) shows the single particle edge channel picture with corresponding Landau levels and density profile. (d-e) shows the result by taking both the chemical and electrostatic potential into account. In (d), the compressible strips are the dashed area and the incompressible strips are the blank area. From [5].

Here,  $\rho_H(x) = \frac{B}{en(x)}$ . Apparently, this relations hold even without the Landau quantization. Taking the two-dimensionality of the electronic system into account, one has to consider the Landau quantization. It is crucial to stress that according to the compressible/incompressible strips theory, the incompressible region has an integer filling factor since here the Fermi level lies between two Landau levels, whilst in the compressible region the Fermi level lies at a partially filled Landau level [8] [9]. From Eq. 2.17 from the previous section, we know the relation between the carrier density and the filling factor. Furthermore, the current should flow completely in the innermost incompressible strip [8] [9]. Therefore, the filling factor in such region is an integer which is denoted  $\nu$  and one can write

$$\rho_H(x) = \frac{h}{\nu e^2}. \quad (2.20)$$

Combining all the three statements (Hall condition, Landau quantization, current carried by the innermost incompressible strip), one obtains for the total imposed current in a Hall bar with width  $2d$

$$I = \int_{-d}^d j_y(x) dx = \int_{-d}^d \frac{E_x(x)}{\rho_H(x)} dx \quad (2.21)$$

so that

$$\Rightarrow U_H = \int_{-d}^d E_x(x) dx = \rho_H(x)I = \frac{h}{\nu e^2}I. \quad (2.22)$$

Besides giving the correct quantized Hall resistances, there are two other important features about the compressible/incompressible strips theory. The first feature is that it identifies the innermost incompressible strip as the current carrying region in the sample. This is the microscopical reason of the exact quantization of Hall resistance. The incompressible strips, in which the Landau levels below the Fermi energy are fully filled, can conduct a Hall current, i.e. a current flowing in the longitudinal direction which is induced by a Hall voltage. In fact, only the incompressible strips are carrying the Hall current. This is because if the compressible strips would also contribute to current, one would expect a voltage drop in the longitudinal direction in the vicinity of QHE. The reason for this is that in the compressible strips, the Landau levels below the Fermi energy are partially filled and provide states in which electrons can be scattered. In other words, the Hall potential drops across the innermost incompressible strip.

The second feature is that it clarifies why both the longitudinal and the Hall traces are not perfectly symmetric around the center of each filling factor. This has to do with the different dominating transport mechanisms in the two magnetic field regions within one quantized Hall state. In Fig. 2.5 b), the evolution of the compressible and incompressible landscape within the 2DES over a quantum Hall plateau is illustrated. At the lower magnetic field side of a quantum Hall plateau, the current carrying incompressible strips are located at the sample edge

while these strips are extended over the sample width at the higher magnetic field side. In the latter case, a bulk current is flowing through a single incompressible strip which include compressible droplets. The asymmetry is a consequence of the difference in the role of disorder. In the following, the role of disorder will be elaborated.

## Extended and Localized States

In the previous calculations, the quantized Hall resistances have been obtained for a clean system. This is consistent with the compressible/incompressible strips theory that even in an absolutely clean system, electron-electron interaction will lead to strip formation at the sample edges and finally the quantized Hall resistances. In reality, however, 2DES samples contain defects which can be treated as disorder potentials. In fact, such defects are supportive for the quantum Hall effect, since disorder increases the width of quantum Hall plateau. Disorder potentials will lead to local potential fluctuations followed by the Landau levels and the incompressible strip will then include compressible islands [10], while the quantized Hall resistances remain unaffected.

Such defects can also have strong impacts on the density of states in a 2DES. The Landau levels in the bulk can no longer be pictured as sharp lines such as in Fig. 2.4 b), but are smeared out. Fig. 2.6 shows such broadened Landau level consisting of two types of states: the extended states close to the center of the Landau levels and the localized states in the tails. The Hall current is carried by the extended states below  $E_F$ . In the incompressible strips, the Landau levels below the Fermi energy are fully filled. This means that the preceding calculation of the quantized Hall resistances in the frame of the compressible/incompressible strips theory is only valid for non-ideal systems, when the Fermi energy lies within the localized states in the incompressible region of the sample.

### 2.1.3 Current-Induced Breakdown of the IQHE

Shortly after the discovery of the quantum Hall effects, the physical limits of the QHEs have attracted strong interest. Besides its potential for basic research, studying the QHE at elevated currents is also crucial as for high precision measurements, the sample current should be as high as possible, without exceeding its critical limit. At such a critical current, it has been observed that the longitudinal and Hall resistances,  $\rho_{xx}$  and  $\rho_{xy}$ , start to deviate from their low current values. In particular,  $\rho_{xx}$  increases suddenly to the order of  $h/e^2$  once the sample current exceeds a certain limit. This phenomenon, shown in Fig. 2.7, is called the breakdown of QHE.

Two aspects have been found to play an important role in the breakdown of QHE: the current distribution and the dependence of the breakdown current on the sample width. For a long time, it was believed that at QHE breakdown, current is confined at the sample edges. However, mea-



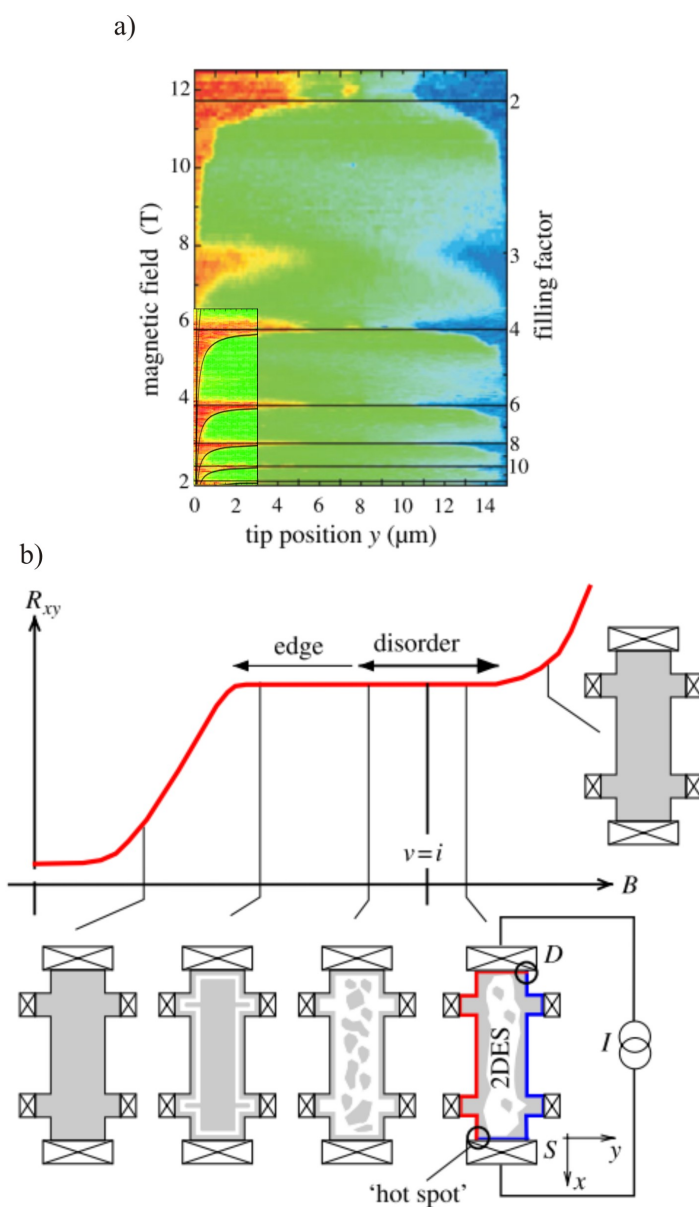


**Fig. 2.5:** Scanning probe microscopy (SPM) measurement of Hall potential. In a), the Hall potential profile is shown as a function of the sample width. Entering any integer quantum Hall state from the lower magnetic field side, the Hall potential changes mainly at the edges of the sample. Approaching the higher field end of the quantum Hall plateau, the Hall potential drops across the entire sample edge. On the left corner, theoretical estimation of the center of incompressible strips is shown as black curves. This two regimes are discussed in b), where it is shown that on the lower magnetic field side, the Hall current is carried by incompressible strips at the edges, while in the higher magnetic field side the entire bulk of the sample is incompressible, but disorder induced compressible puddles can form and strongly vary the local Hall potential. Modified from [10]

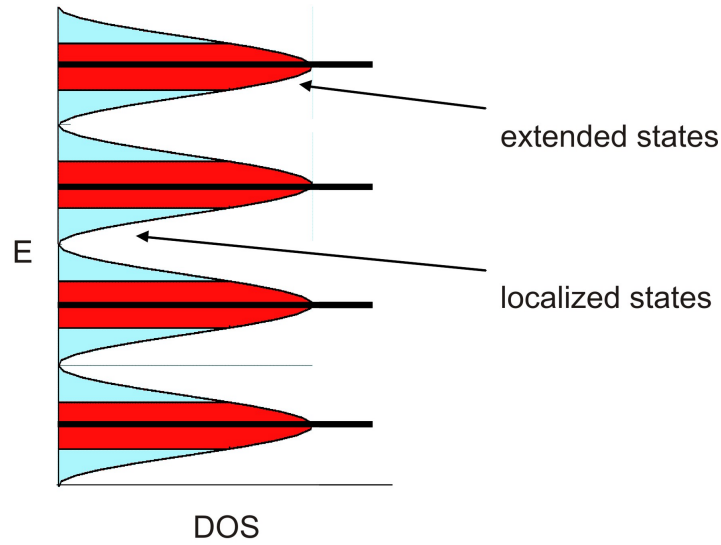


**Fig. 2.6:** Landau quantization of a spinless 2DES. Taking the disorder potentials into account, the Landau levels can no longer be represented by sharp lines but strips with a finite width known as extended states which are broadened by the localized states.

measurements utilizing a scanning force microscope have shown that the formation of compressible-incompressible strips continue to exist even in the onset of breakdown of QHE [12]. Depending on the exact magnetic field or filling factor, the incompressible strips are confined at the edges or established along the bulk. This result suggests that the QHE breakdown is not primarily an edge or bulk effect, but depends on sample properties and geometry. The width dependence of the breakdown current can be approached using a percolative model which takes density fluctuations due to inhomogeneities in the doping layer into account. Such inhomogeneities can be described by a characteristic length called inhomogeneity length  $l_{in}$ . It has been shown that the breakdown current  $I_{BD}$  increases monotonically with the sample width  $w$  [13] [14]. The exact dependency on the width depends on the range of fluctuations in the 2DES. For short-range fluctuations ( $l_{in} \ll w$ ), the percolation paths are densely distributed and leads to a linear dependence of the breakdown current  $I_c$  on the sample width  $w$  [11]. For long-range fluctuations of the order of the sample width, a sublinear dependence is seen, which is attributed to more effective screening of short-range fluctuations by illumination or by increasing the mobility.

Up to date, no conclusive model is known which describes the underlying mechanism of the breakdown of QHE. There are, nonetheless, a number of proposed mechanisms, including quasi-elastic inter-Landau level scattering (Quills) and the hot electron model. The Quills model successfully describes breakdown of QHE in samples with small width ( $1 \sim 10 \mu\text{m}$ ). Within such a small width, the current distribution is assumed to be homogeneous. At high input currents,

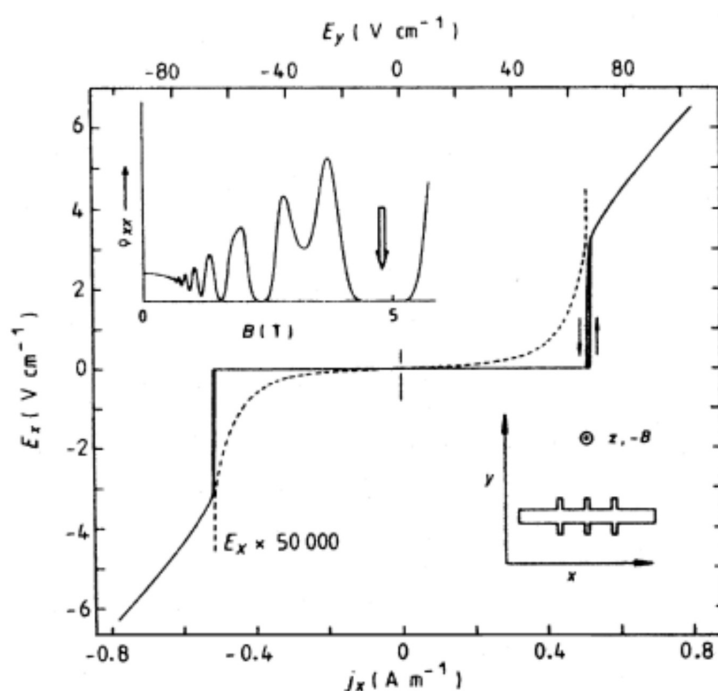


**Fig. 2.7:** Breakdown of quantum Hall effect characterized by a sudden increase of the longitudinal resistance at a sufficiently large longitudinal current. The dashed line is magnified by  $5e5$ . From [11].

the electric field along the transversal direction, or Hall field, becomes so large that the Landau levels are bended. This enables scattering processes where electrons are scattered from the highest occupied into the lowest unoccupied Landau level. The breakdown currents observed in such samples are usually very large and the breakdown curves often rather sharp, which is associated with an avalanche-type multiplication of excited carriers after injection into a constriction [15].

The hot electron model mainly describes the hysteresis effect when up- and back-sweeping the current [16]. The current dependence of the electron temperature which has a S-shape is shown to be responsible for the hysteretic effect. This S-shape originates from the balancing between energy gain of electrons due to electric field and energy loss (such as due to Quills-mechanism or phonon emission) [16]. Such competing effects will lead to instability in the electron temperature and finally to the hysteresis in the breakdown currents.

## 2.2 Fractional Quantum Hall Effect

In the previous section, only integer filling factors have been discussed. As a matter of fact, the quantum Hall effect has also been observed at fractional filling factors [17]. Nevertheless, the latter effect is of very different origin compared with its integer counterpart.

The main difference between the fractional and the integer quantum Hall effects lies in the role of electron-electron interaction. In the IQHE, each Landau level is fully filled, so that no vacant states are available. The electrons therefore cannot reduce their Coulomb energy by adjusting their spatial distribution, so that the ground state wave functions are given by the Slater-determinant wave functions. In the FQHE, vacant states are available within the unfilled Landau level, so that the electrons interact with each other strongly to reduce the Coulomb energy while maintaining their kinetic energy. Here, the Coulomb energy is the only relevant energy scale since the cyclotron energy is frozen. Theoretically, neither an exact analytical solution nor a perturbative one is conceivable: the former one due to the large number of particles in the many body system while the latter one due to the Coulomb-energy being the only relevant energy scale, since the kinetic energy is frozen at sufficiently high magnetic fields and low temperatures. One thus has to approach the wave function in a different way.

*Laughlin et al.* postulated a wave function, which gives the exact ground state wave function for the odd denominator fractional quantum Hall states at filling factor  $\frac{1}{q}$  ( $q$  is an odd integer)

$$\Psi_{1/(q)} = \prod_{j < k} (z_j - z_k)^q \exp \left[ -\frac{eB}{4\hbar} \sum_l |z_l|^2 \right]. \quad (2.23)$$

The product term indicates the Coulomb energy between two electrons as the relevant energy scale: the probability density goes to zero whenever two electrons approach each other. The Coulomb energy can be minimized by avoiding such case.

*Jain et al.* came up with an idea of mapping the electron-electron interaction into even number of magnetic flux quanta carried by each electron, thus making the strongly interacting electrons into weakly interacting quasi-particles, the so-called *composite fermions* [18]. If  $2p$  is the number of magnetic flux quanta (vortices) bound to composite fermion (also called the vorticity or the vortex charge of the composite fermion),  $n$  is the density of the 2DES, one can then write the effective magnetic field experienced by the composite fermions as

$$B^* = B - 2pn\phi_0, \quad (2.24)$$

where  $\phi_0 = h/e$  is the elementary quantum of a magnetic flux. Electrons at filling factor  $\nu$  are thus converted into composite fermions at an effective filling factor of  $\nu^*$  given by

$$\nu = \frac{\nu^*}{2p\nu^* \pm 1}. \quad (2.25)$$

This means that fractional quantum Hall states for electrons can be understood as integer quantum Hall states for composite fermions. This is best reflected by comparing the SdH traces of IQHE and FQHE, as shown in Fig. 2.8.

Under suppression of the spin, the unnormalized microscopic many body wave function for fractional states is written as

$$\Psi_\nu = \Phi_{\nu^*} \prod_{j < k} (z_j - z_k)^{2p}, \quad (2.26)$$

where  $\Phi_{\nu^*}$  denotes the Slater-determinant wave function of non-interacting electrons at the corresponding filling factor  $\nu^*$ . The product term contains the entire concept of composite fermions: each factor means that an electron executes a closed path around a second electron, thereby generating a phase of  $2p \times 2\pi$ . Since a closed loop around a unit vortex generates a phase of  $2\pi$ , this means that each electron sees  $2p$  vortices on another electron. In fact, the reduction of Coulomb energy can also be understood by attaching vortices to electrons: the wave function 2.26 keeps the electrons apart more effectively than by merely satisfying the Pauli principle<sup>1</sup>. In other words, the Coulomb energy is effectively used to create the vortices, so that only a small amount of it is left for the resulting composite particles.

The fractional filling factor of  $\frac{1}{2}$  doesn't exhibit any quantum Hall state, which can be explained by the composite fermion picture: this fraction in the view of electrons is playing the role of  $B = 0$  for composite fermions. This means that at this filling factor, one has a Fermi sea of composite fermions, which is similar to the electron Fermi sea, except that the former is spin polarized.

Eq. 2.26 yields fairly accurate yet non-exact results for the ground state wave function.

Both the Laughlin's wave function and the composite fermion picture are, however, only able to explain the odd denominator fractional states. Exotic fractional states with even denominator, such as  $\nu = \frac{5}{2}$ , have also been observed [20], whose origin is still under discussion.

---

<sup>1</sup>The probability that two electrons will approach each other within a distance of  $r$  is proportional to  $r^{2(2p+1)}$  in the current case, while in the other case it is proportional to  $r^2$ .

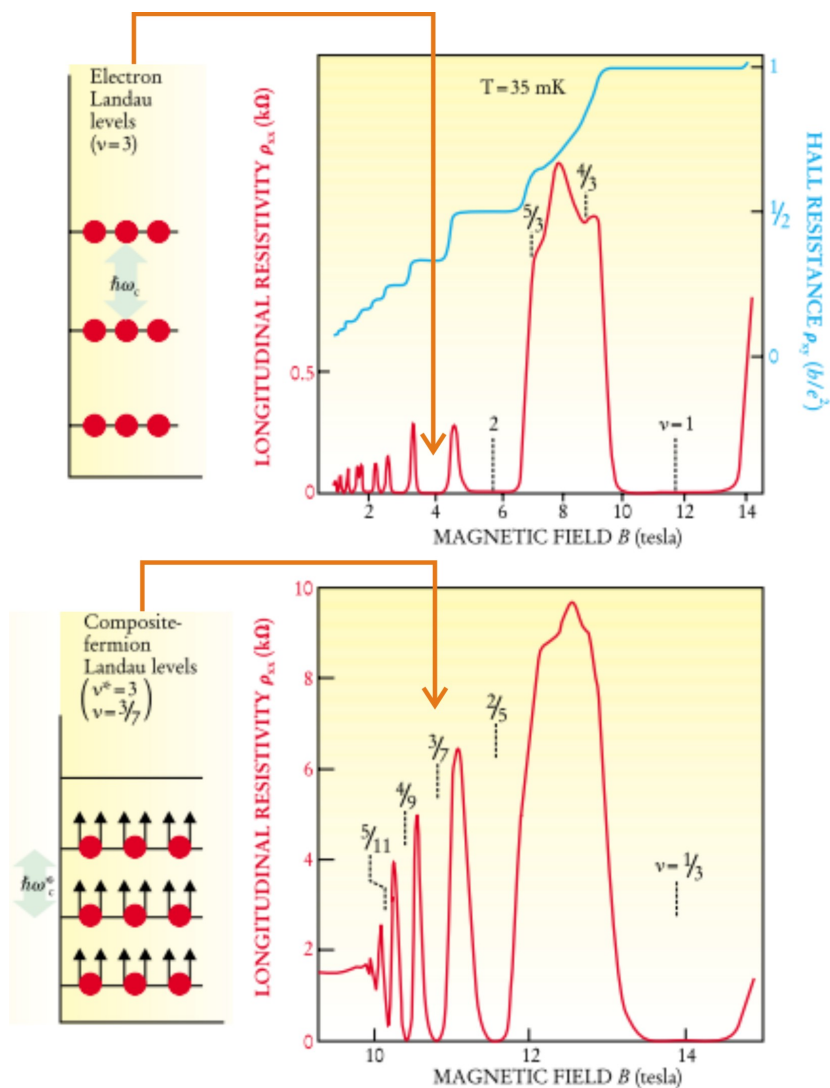


**Fig. 2.8:** Comparing IQHE (top panel) and FQHE (bottom panel). The two red curves, showing the respective Shubnikov-de Haas oscillations, are remarkably similar which is consistent with the composite fermion picture of the fractional filling factors. Modified from [19]

# Chapter 3

## Bilayer Quantum Hall State at $\nu_T = 1$

The study of correlated electron systems in low dimensions continues to be important for condensed matter physics nowadays. This has been driven by the emergence of both high  $T_c$  superconductors and the fractional quantum Hall effect in the last decades: while strongly correlated 2DES on a lattice are important for the former system in which weak coupling between the superconducting planes is believed to be crucial for the correlation, the latter provides a frame to study the correlation in continuum 2DES. Recently, other systems such as graphene, topological insulators and 2D systems embedded in oxide-based interfaces have also attracted strong interest in terms of correlated charge systems.

Early work has anticipated that in presence of strong magnetic fields, interlayer correlations in multilayer systems can lead to fractional quantum Hall states [21]. With the advances of crystal growth techniques such as molecular beam epitaxy (MBE), high quality heterostructures have become available which allows studying such interlayer correlations. One of the most prominent states in this category is the  $\nu_T = 1$  bilayer quantum Hall state, which is both experimentally and theoretically well established as being a correlated state governed by intra- and interlayer Coulomb interactions.

In this chapter, electron bilayer systems will first be introduced, followed by a discussion about the  $\nu_T = 1$  quantum Hall state being a correlated state. The theoretical models describing the ground state and finally its low energy excitations in the pseudospin picture will be presented. This is followed by an introduction to three types of transport experiments as well as theoretical models explaining the critical tunneling current.

### 3.1 Electron Bilayer Systems

A bilayer system can be formed either by confining electrons into two separate layers, or by confining them into two different edges of a wide quantum well. In both cases, the layer separation can be as small as 100 Å and much smaller than the average distance between electrons

within each layer. In this chapter and throughout this work, it will be focused on the first case, which is schematically shown in Fig. 3.1. When the two layers, being symmetrically doped with electrons resulting in the same densities  $n_T = n_B$ <sup>1</sup>, are spaced by a sufficiently large distance, their wave functions do not overlap resulting in a system of two individual quantum wells. On the other hand, if the two layers are brought into close proximity, their wave functions can overlap, which allows the electrons to tunnel back and forth between the layers. If the wave functions  $|\uparrow\rangle$  and  $|\downarrow\rangle$  denote the eigenfunctions for the upper and lower layers, respectively, the superposition of the wave functions can thus be written as

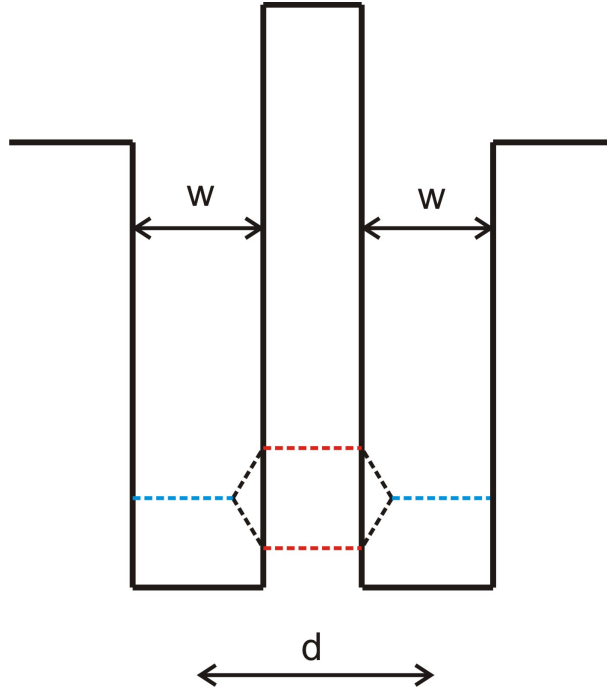


**Fig. 3.1:** Schematic profile of the conduction band edge in a double quantum well system. The dashed lines indicate the energy splitting between the symmetric and antisymmetric state in the limit of strong interlayer coupling.

$$\Psi = u|\uparrow\rangle + v|\downarrow\rangle, |u|^2 + |v|^2 = 1. \quad (3.1)$$

Similar to any other two level system, which undergoes hybridization and form new energy levels, this interlayer interaction can also lead to a gap between two hybridized energy levels: the symmetric state with lower energy and the antisymmetric state with higher energy. In the ground state, the electrons will reside in the lower energy symmetric state with  $u = v = \frac{1}{\sqrt{2}}$ .

<sup>1</sup>From now on, if not specified, all discussions are based on the symmetrically doped case.



The entire system will behave like a monolayer system with an extra degree of freedom, which manifests itself as an extra splitting. The new energy gap is called the  $\Delta_{SAS}$  gap. Intrinsically, it depends on both the layer spacing and the height of the energetic barrier between the quantum wells and can vary between zero and many hundreds of Kelvins, depending on the sample. This splitting can thus be much larger or smaller than the Coulomb interaction between the layers,  $E_C \propto e^2/d$ .

The state described above is called the strong tunneling bilayer system, which is referring to the size of the energy gap  $\Delta_{SAS}$ . The larger this energy gap, the more efficient electrons will reside in the lower lying state, thus the more strongly the two layers are coupled. Under application of a perpendicular magnetic field  $B$ , extra quantum Hall states are visible due to this energy gap. The activation energy of these extra quantum Hall states are in the same energy scale as  $\Delta_{SAS}$ . Since this energy gap does not involve electron-electron interaction, it is also referred to as the single electron bare tunneling amplitude or tunnel coupling strength. In the following, a different case is going to be introduced, in which interlayer tunneling does not require such a strong coupling between the layers, resulting in an energy gap which has a highly collective nature.

### 3.2 Correlated $\nu_T = 1$ State in Weakly Coupled Bilayers

Two energy scales are essential at  $B > 0$ : the Coulomb energy between electrons within each quantum well,  $E_{intra} \propto l_B^{-1}$ , where  $l_B$  is the magnetic length which is equal to the cyclotron radius of the lowest Landau level, and the Coulomb energy between the layers,  $E_{inter} \propto d^{-1}$ . The ratio between these two energies is thus proportional to the  $d/l_B$ , which indicates the relative strength of these two interactions. When the two layers are separated so that  $\Delta_{SAS} \ll E_C$ , one would expect no interlayer coupling in the single electron picture. In the special case of  $\nu_{upper} = \nu_{lower} = \frac{1}{2}$  and  $d/l_B > 2$ , one effectively has two non-interacting Fermi seas. Each Fermi sea exhibits no quantum Hall effect. This is demonstrated by the blue trace of Fig. 3.2 a), where a longitudinal current is applied only through the upper layer while the longitudinal resistance is measured for this layer. However, as can be seen from Fig. 3.2 b), when the effective layer spacing  $d/l_B$  is set to a value that is smaller than 2, spontaneous interlayer coherence leads to the observation of a bilayer quantum Hall state at a total filling factor of one, or  $\nu_T = 1$ . Such a quantum Hall effect is clearly visible in the red trace of Fig. 3.2 a), where a longitudinal current is applied through both layers simultaneously while the longitudinal resistance is measured for both layers.

There are several arguments why this  $\nu_T = 1$  bilayer quantum Hall state is due to correlation. First is that this state survives at arbitrarily weak single particle tunneling amplitude, i.g.  $\Delta_{SAS} \rightarrow 0$  [24]. A second argument is that if the excitation gap  $\Delta$  of the  $\nu_T = 1$  state would be

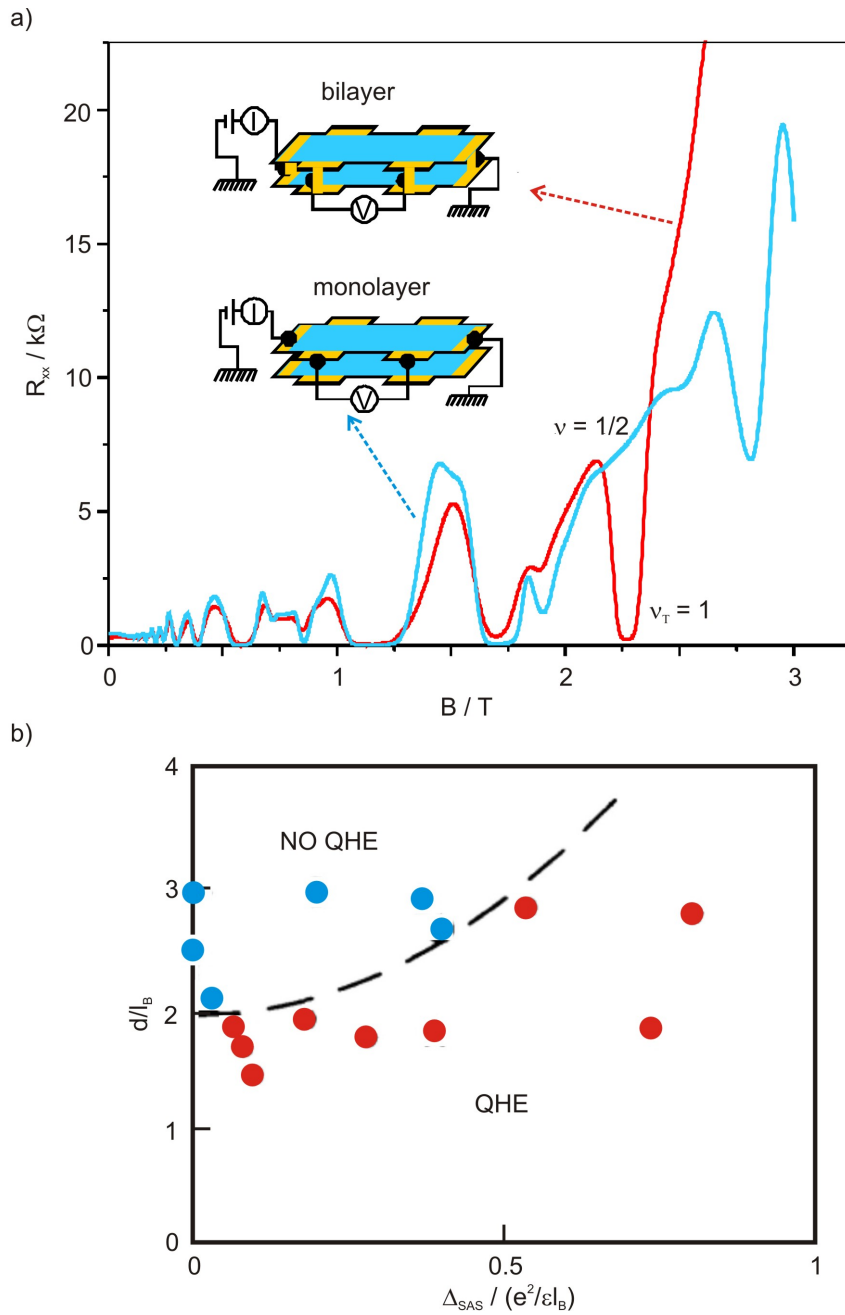


**Fig. 3.2:** Correlated  $\nu_T = 1$  state in bilayers. (a): Longitudinal resistance of a monolayer (blue trace) and bilayer (red trace) systems. Quantum Hall effect of  $\nu_T = 1$  can be observed in the bilayer systems. Ohmic contacts in the monolayer case are connecting only one layer, while they connect both layers in the bilayer case. (b): Phase diagram of the  $\nu_T = 1$  quantum Hall effect with parameters  $d/l_B$  and  $\Delta_{SAS}$ . The data points at the lower left corner of the panel are evident that QHE is also observable in the weak tunneling regime. (a) from [22]. (b) modified from [23].

from single particle origin, the activation energy of the  $\nu_T = 1$  state would also be on the scale of  $\Delta$ . This is not the case as dissipation already levels off as the temperature is corresponding to  $0.1\Delta$ . This has been observed in both double layer and wide quantum wells and is consistent with a thermally induced collapse of a collective order. The third argument for a correlated state is that the excitation gap has been observed to drop significantly at small parallel magnetic fields, which is explained by a phase shift contributed by a horizontal magnetic flux in presence of vertical loop current paths. Since the number of flux quanta needed to wind the phase by a certain value is fix, the size of magnetic field at which such a drop of energy gap occurs is inversely proportional to the size of the vertical loop. Small  $B_{\parallel}$  would thus correspond to a large coherent length in the system.

Since its discovery, this  $\nu_T = 1$  quantum Hall state has attracted significant attention both in experiments and theory. In the following, different theoretical models developed in order to describe the ground state of the  $\nu_T = 1$  effect will be introduced, which are mathematically identical but reflecting different physical aspects of the same system.

### 3.2.1 $\nu_T = 1$ Ground State

#### (111) State

As shown in 2.2, *Laughlin* have developed a wave function to describe the fractional quantum Hall states. Using Eq. 2.23 and taking the electron spin into account, *Halperin et al.* have applied the generalized Laughlin wave function to describe the coincidence states between two Landau levels. Similarly, one can also adapt this approach to formulate the ground state wave function of  $\nu_T = 1$ . Under  $q = 1$ , this yields the following wave function

$$\Psi_{111} = \prod_{i<j} (z_i - z_j) \prod_{i<j} (w_i - w_j) \prod_{i<j} (z_i - w_j) e^{-\frac{1}{4t^2 B} \sum_i |z_i|^2} e^{-\frac{1}{4t^2 B} \sum_i |w_i|^2}. \quad (3.2)$$

Similar to the Laughlin wave function, this so-called Halperin-111 wave function also minimizes the Coulomb interaction energy by spatially redistributing the electrons. The only difference is that in the case of bilayer, one has not only to minimize  $E_{intra}$  but also  $E_{inter}$ . From Eq. 3.2 one finds that the probability amplitude  $|\Psi|^2$  vanishes not only whenever two electrons approach each other within each quantum well, but also when they try to be located directly above each other. From the Halperin-111 wave function, one knows that the energy scale relevant in describing the  $\nu_T = 1$  quantum Hall state is the Coulomb interaction between the electrons.

#### Excitonic BCS-Superfluidity

The Halperin-111 wave function can also be rewritten in a different form [25] [26] [24]

$$\Psi = \prod_k \left[ \frac{1}{\sqrt{2}} \left( 1 + e^{i\varphi} c_{k,\downarrow}^\dagger c_{k,\uparrow} \right) \right] |\psi_\uparrow\rangle, |\psi_\uparrow\rangle \equiv \prod_k c_{k,\uparrow}^\dagger |0\rangle. \quad (3.3)$$

This is realized under particle-hole transformation. The form of Eq. 3.3 strongly resembles the ground state wave function postulated by Bardeen, Cooper and Schrieffer for superconductors [27]. The only difference is that in the BCS wave function describing the superconductivity, electrons are bound to electrons forming bosons which undergo condensation at low temperatures, whilst in the current case of bilayers, electrons are bound to holes forming excitons undergoing a condensation<sup>1</sup>. Thus, the half filled Landau levels can be thought of being half filled by electrons coupled to the holes from the adjacent layer. This is shown in Fig. 3.3. Similar to the phonon-coupled electrons in Cooper pairs, electrons and holes in the excitonic condensate also have opposite wave vectors, resulting in all excitons possessing the  $\mathbf{k} = 0$  state, which does not violate Pauli principle since excitons are bosons.

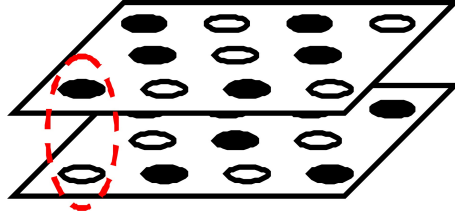


**Fig. 3.3:** Illustration of bilayer excitons. Each layer exhibiting filling factor of  $1/2$  is half-filled with electrons (solid circles) and holes (empty circles). The interlayer coherence at  $\nu_T = 1$  can be shown as given by formation of bound electron-hole pairs or bilayer excitons. Note that the ordering of charge carriers is not strictly given at this quantum Hall state.

The  $\nu_T = 1$  quantum Hall state can thus be viewed as a BCS-condensate of excitons. The existence of Bose-Einstein-condensate of excitons has been predicted back in the 1960s [31]. For a long time, its experimental realization using optical pumping technique has yielded no conclusive result, mostly due to the short lifetime of excitons with electron residing in the conduction band and hole in the valence band [32]. Recently, *High et al.* reported coherence length of indirect excitons of the order of  $30 \mu\text{m}$  thus much larger than in a classical gas, indicating a condensate [33]. On the contrary, bilayer excitons are electron and hole pairs, from which both constituents reside in the conduction band. Such indirect excitons have a lifetime that is infinite.

<sup>1</sup>Besides considering the  $\nu_T = 1$  state as an excitonic condensate, there also exist an alternative model which uses the term *composite bosons* [28] [29] [30]. Such composite bosons are formed by electrons coupling to a single magnetic flux quantum.

## Pseudospin Ferromagnet

In the case of monolayer  $\nu = 1$  state, the wave function is written as a product of the Laughlin wave function and a spin wave function

$$\Psi = \prod_{i < j} (z_i - z_j) e^{\frac{1}{4l_B^2} \sum_i |z_i|^2} | \uparrow \uparrow \uparrow \dots \uparrow \rangle. \quad (3.4)$$

In its ground state, the monolayer filling factor  $\nu = 1$  shows spontaneous magnetization which exists even at vanishing Zeeman energy  $E_Z \rightarrow 0$ . All the spins align themselves in the direction of the external magnetic field and form a quantum Hall ferromagnet (QHF). The exchange interaction in traditional ferromagnetic materials such as Fe exceeds orders of magnitudes of the dipole-dipole interaction energy, which tends to align the spins in opposite directions. Similarly, the Coulomb exchange energy is the relevant energy scale for QHF.

For the case of  $\nu_T = 1$  bilayer state, one can map the Halperin-(111) wave function into

$$\Psi = \prod_{i < j} (z_i - z_j) e^{\frac{1}{4l_B^2} \sum_i |z_i|^2} | \rightarrow \rightarrow \rightarrow \dots \rightarrow \rangle, | \rightarrow \rangle \equiv u | \uparrow \rangle + e^{i\varphi} v | \downarrow \rangle. \quad (3.5)$$

Apparently, the only difference between Eq. 3.4 and Eq. 3.5 lies in the orientation of the spin, or pseudospin for the latter case. The pseudospin denotes the *which layer* degree of freedom of an electron: an up-pseudospin means an electron residing in the upper and a down-pseudospin in the lower layer. The coefficients  $u$  and  $v$  satisfy the normalization condition  $|u|^2 + |v|^2 = 1$ . In this picture, one can assign a pseudospin vector  $\mathbf{S}(\mathbf{r})$  to each spatial position in the bilayer system. Each pseudospin has an out of plane component  $S_z$  given by the polar angle  $\theta$ . The expectation value of this  $S_z$  is proportional to the difference between probability of an electron residing in the upper and the lower layer,  $\langle S_z \rangle \propto |u|^2 - |v|^2$ , thus it represents the density imbalance between the layers and the charge conjugate to the phase  $\varphi$ , the latter defining the projection of  $\mathbf{S}$  to the xy plane. Fig. 3.4 illustrates such a generic pseudospin which has an out of plane component.

It might not be obvious why the projection angle of the pseudospin vector to the xy plane is exactly the phase angle in Eq. 3.5: the Pauli spin matrix can be calculated here for the pseudospin which yields  $\langle \sigma_x \rangle = \cos \varphi$  and  $\langle \sigma_y \rangle = \sin \varphi$ . The physical meaning of this pseudospin picture is similar to that of the monolayer QHF: if one assumes that the real spins are frozen at  $\nu_T = 1$ , Eq. 3.5 describes the electron wave function completely. Due to Pauli principle, electrons will minimize their exchange energy by aligning their pseudospins. In ground state, in which the two layers are density balanced,  $\mathbf{S}$  lies in the xy plane and points in the same direction throughout the entire bilayer system. Hence, one has a pseudospin quantum Hall ferromagnet due to this spontaneous pseudospin magnetization. In transition from the excited state to the ground state, the system thus undergoes a spontaneous symmetry breaking: in the disordered phase, the in-plane component of the pseudospin is averaged out throughout the bilayer; in the

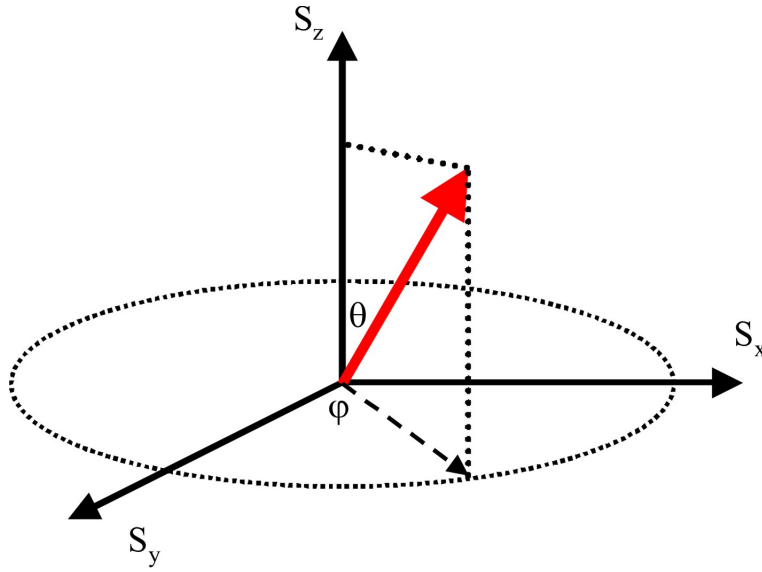


**Fig. 3.4:** Illustration of a pseudospin (red arrow) with an out of plane component  $S_z$  given by the polar angle  $\theta$ . The azimuthal angle  $\varphi$  gives the direction of the pseudospin in the  $xy$  plane.

ordered phase, the pseudospin chooses any value of  $0 < \varphi < 2\pi$ , which breaks the rotational symmetry. This spontaneous symmetry breaking is the reason for the formation of the  $\nu_T = 1$  quantum Hall state.

As pointed out earlier, both the pseudospin ferromagnet and the BCS excitonic condensate pictures can be deduced from the Halperin-(111) wave function. They are thus naturally related. This becomes clear in terms of the phase angle  $\varphi$ , which appears in both wave functions Eq. 3.3 and Eq. 3.5. In the BCS condensate of Cooper-pairs forming conventional superconductors, this phase angle describes the superposition coefficients for having and not having a Cooper pair in a given location in space; in the excitonic condensate forming the  $\nu_T = 1$  state, the phase angle describes the superposition coefficients for having and not having an exciton in a given location in space. Both phase angles are constant in space in the ground state. In other words, one has to pay an energy penalty for varying the phase angle spatially: in case of BCS superconductor,  $\nabla\varphi(\mathbf{r})$  results in a charge current, which tries to equalize the phase by charge transfer (Josephson effect). Analogously, such a phase gradient in the  $\nu_T = 1$  excitonic condensate leads to a neutral flow of excitons, thereby constituting a pseudospin current

$$J = \frac{2\rho_s}{\hbar} \nabla\varphi, \quad (3.6)$$

where  $\rho_s$  denotes the pseudospin stiffness due to loss in exchange energy while tilting the pseu-

dospin.

The pseudospin wave function might remind one of Eq. 3.1 in the strongly coupled limit. The only difference is that one has no braiding of two states in the weakly coupled limit since the wave functions of the two layers do not overlap in the absence of tunneling. It is the symmetry breaking that leads to the (fractional) quantum Hall effect, rather than a hybridization of wave functions. This difference also leads to the different low energy excitations which will be elaborated in the following section.

### 3.2.2 Low Energy Excitations

At the monolayer  $\nu = 1$  state, the lowest excited states are given by spin textures called *skyrmions*. Since the Landau level is fully filled, one has a uniform charge density and the Pauli principle prohibits any excitation in which spin flip is not involved [34]. Similarly, in a bilayer system which contains disorders (i.e. due to inhomogeneities of the doping), topological defects called *merons* can also exist as pseudospin textures at the  $\nu_T = 1$  state [24]. As demonstrated by Fig. 3.5, the local pseudospin tilts by  $\pm 2\pi$  at infinity, while in the core region the pseudospin points either up or down in relative to the  $xy$  plane. At sufficiently low temperatures, merons are bound vortice-antivortice pairs which can be characterized by vorticity ( $\pm 1$ ) and charge ( $\pm \frac{1}{2}$ ). Thus they are also called bound meron-antimeron pairs, which are charge-neutral and have zero vorticity. The inner energy of bound meron-antimeron pairs is lower than that of free merons/antimerons, whose energy scales with  $E \propto |\nabla\varphi|^2$  by giving rise to a pseudospin gradient, thus disturbing the order parameter  $\varphi(\mathbf{r})$ . They are favored by the ground state since lowering the inner energy is more effective for minimizing the total free energy at low temperatures than increasing the entropy. At high temperatures, on the other hand, it is more effective to increase the entropy, thus the merons are unpaired. The transition from the state in which merons are paired to the one with free merons is a generic phase transition called *Kosterlitz-Thouless* (KT) transition.

The KT transition describes a quantum mechanical phase transition in two-dimensional systems from a high-temperature disordered phase with the exponential decay in correlation to a low-temperature quasi-ordered phase. It is a phase transition of infinite order and has a finite transition temperature  $T_{KT}$ . For bilayer systems, this transition temperature is anticipated at the order of the pseudospin stiffness  $\rho_s \sim 0.5$  K. So far, experimental proof is still missing. Once observed, it would be the first quantum Hall state to exhibit a phase transition at non-zero temperature.

According to the Goldstone theorem, a spontaneous breaking of a continuous symmetry will lead to gapless collective modes called *Goldstone bosons*, which are massless and linearly dispersed. In the case of ferromagnetism, such Goldstone-bosons exist in the form of spin oscillations or *magnons*. Analogously, pseudospin waves can also exist in the  $\nu_T = 1$  pseudospin

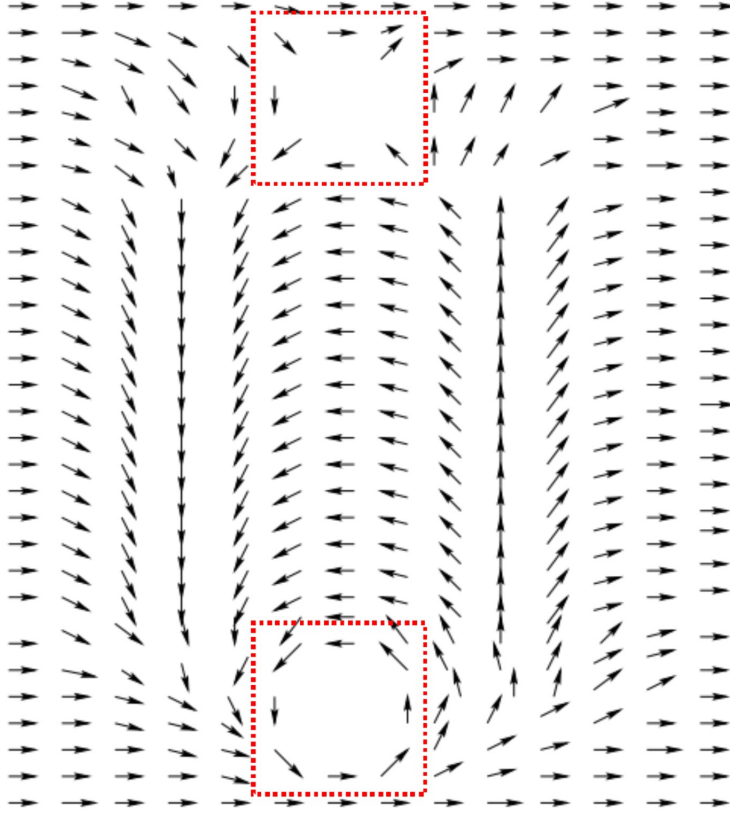


**Fig. 3.5:** A meron-antimeron pair in the ground state of  $\nu_T = 1$ . The arrows illustrate the pseudospins, which point in a certain direction except in the region confined by the meron-antimeron pair (enclosed in red dashed lines). Taken from [24].

quantum Hall ferromagnet. At zero interlayer tunneling, the Goldstone mode is believed to have a zero pseudospin wave vector at zero energy. A finite but small tunneling leads to a finite energy gap thus the formation of quantum Hall effect. An in-plane magnetic field component  $\mathbf{B}_{\parallel}$  can couple to the wave vector  $\mathbf{q}$  according to

$$\mathbf{q} = e\mathbf{B}_{\parallel}d/\hbar \quad (3.7)$$

and induce a resonance at an interlayer bias which corresponds to the energy of the Goldstone bosons

$$eV^* = \underbrace{\hbar\sqrt{\frac{\rho_s}{\Gamma}}}_{:=u} \frac{e}{\hbar} q. \quad (3.8)$$



Such linear dispersion has been observed by Spielman et al. [35]. Fig. 3.6 shows their result, from which a pseudospin velocity of  $u = 14$  km/s has been deduced [36].

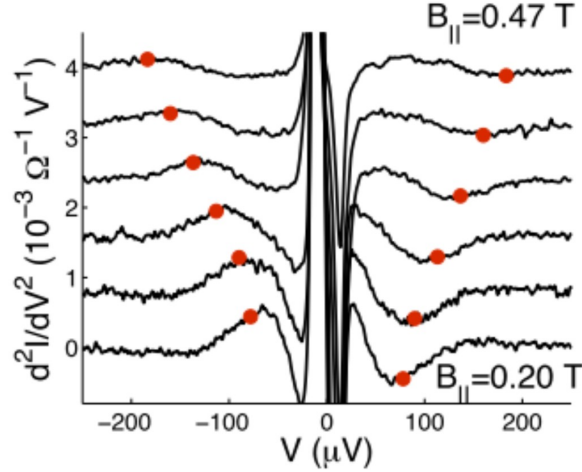


**Fig. 3.6:** Resonance peaks (red dots) in interlayer tunneling under parallel magnetic field. The resonance voltage evolves nearly linearly as a function of magnetic field [35]. Based on this result, Hyart et al. have deduced a pseudospin wave velocity of 14 km/s [36].

### 3.3 Transport at the $\nu_T = 1$ State

Transport is a powerful tool to extract deep-lying properties of low dimensional charge systems. In the case of  $\nu_T = 1$  state, the double quantum wells geometry of the bilayers enables studying transport in three different configurations: longitudinal transport, interlayer tunneling and excitonic counterflow. Fig. 3.7 illustrates all three configurations. In the following, all three configurations will be described.

#### Longitudinal Transport

In the longitudinal (or in-plane<sup>1</sup>) transport, current is applied to one or both layers through the sample plane. The current here is carried by quasi-particle excitations. These are, in analogy to quasi-particles in BCS-superconductors outside the superconducting gap, individual charge carriers which are not bound to form excitons. This quasi-particle current is associated with

<sup>1</sup>In the rest of this work, if not further specified, in-plane is equivalent to longitudinal.

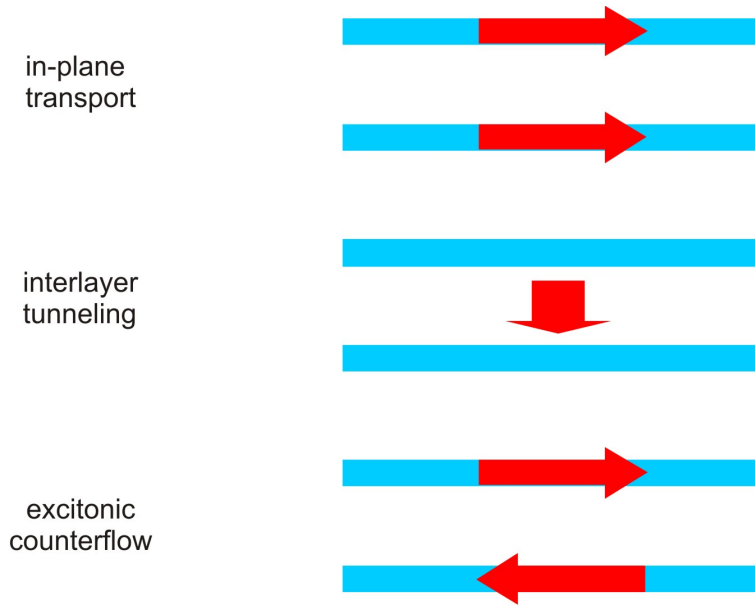


**Fig. 3.7:** Three different transport configurations for bilayers at  $\nu_T = 1$ . In in-plane transport (upper), an external current is applied through one or both layers; in interlayer tunneling (middle), current is applied between the layers; in excitonic counterflow (lower), current flows through both layers in opposite directions.

the quantum Hall effect observed at  $\nu_T = 1$ , leading to the vanishingly small longitudinal resistance shown in Fig. 3.2 a). There also exists an alternative form of in-plane transport which demonstrates the coherence between the layers. Fig. 3.8 shows the Coulomb drag effect [37] [38]: longitudinal current is applied to one layer while the longitudinal and Hall resistances are measured in both layers separately. The upper (drive) layer exhibits quantum Hall effect at several filling factors. The lower (drag) layer only exhibits quantum Hall effect at the total filling factor of one, at which both layers show a minimum in the longitudinal resistance accompanied by a Hall resistance corresponding to filling factor of one.

### Interlayer Tunneling and Josephson Effect

One of the most important quantum phenomena in low dimensional charge systems is the tunneling of particles through an energetic barrier, which is classically not permeable. In superconductivity, a junction consisting of two superconductors separated by a thin insulating barrier or weak link, known as the Josephson junction, exhibits a supercurrent that flows between the superconductors not due to any bias voltage difference but due to the phase difference between the two superconductors [39]. This phenomenon is described by the DC Josephson equation

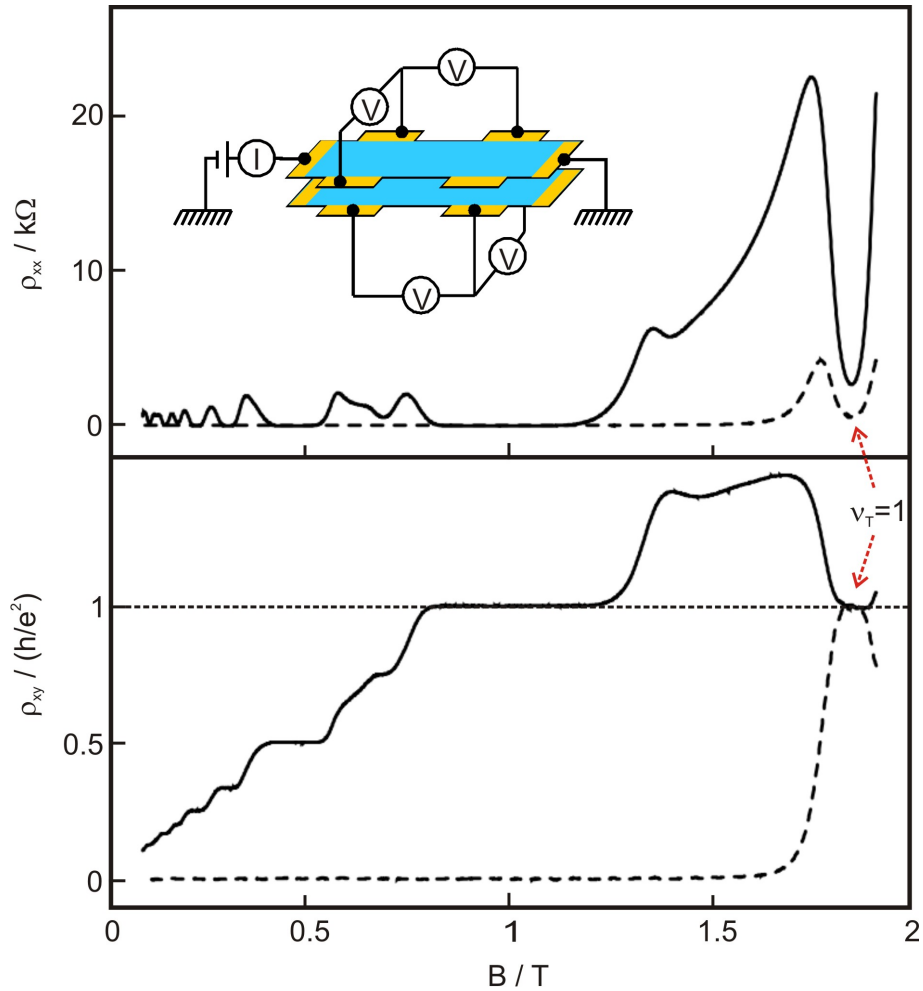


**Fig. 3.8:** Coulomb drag measurement in bilayers, with each ohmic contact connecting only one layer. External current is applied to flow through the upper layer. The longitudinal (upper panel) and Hall (lower panel) resistances are measured for the upper (solid curves) and lower (dashed curves) layer. At  $\nu_T = 1$ , the Hall resistance of both layers shows quantized value corresponding to filling factor one and the longitudinal resistance of both layers shows a minimum. Modified from [38].

$$I = I_c \sin \phi. \quad (3.9)$$

Here, the supercurrent is carried by Cooper pairs—two electrons bound to each other due to attractive interactions mediated by electron-phonon interactions [27]<sup>1</sup>. Josephson's second prediction, that a fix voltage difference across the junction results in a phase difference that is linear in time and the supercurrent is an AC current, is summarized as

$$\frac{d\phi}{dt} = 2eV(t)/\hbar. \quad (3.10)$$

Shortly after the confirmation of the DC Josephson effect, the AC supercurrent was observed under microwave irradiation [41]: steps are formed at dc bias voltages which correspond to an integer number of flux quanta in the barrier.

A similar tunneling configuration can be realized in bilayers at  $\nu_T = 1$ , when probing the current tunneling between the two quantum wells. An enhanced tunnel conductance as shown in Fig. 3.9 is observable about zero bias voltage up to a critical current [42] [43]. Due to this astonishing resemblance to the well established Josephson effect in conventional superconductors—charge carriers tunnel between two charge systems coupled by a barrier, the latter tunneling is referred to as a *Josephson-like* interlayer tunneling<sup>1</sup>.

However, there exist some differences between the superconductor Josephson junctions and the  $\nu_T = 1$  bilayers: phase coherence already exists in each of the two superconductors before they are brought into contact, whilst the interlayer phase coherence is not established until the two quantum wells are brought into a weak tunneling system at  $\nu_T = 1$ . The consequence is that in the former case, one speaks about the phase difference between the two BCS-condensates, whilst in the latter one the phase of the excitonic condensate (or the phase angle in the pseudo-spin space) is the phase difference in the tunneling at the same time.

Furthermore, the  $\nu_T = 1$  vertical tunneling current is not a supercurrent carried by the coupled electron-hole pairs, as Cooper pairs for superconductors, but a pure electron current. Strictly speaking, the true bilayer Josephson junction can be realized in a horizontal tunneling geometry depicted in Fig. 3.10 [45].

In terms of experimental observations, a significant difference is that in the  $\nu_T = 1$  bilayer tunneling, the tunneling peak as well as width are finite. Numerous theoretical works have discussed the origin of dissipation in the  $\nu_T = 1$  interlayer tunneling. While some models argue that the anticipated DC Josephson effect is destroyed by disorder in form of vortex fields (merons) [46], others claim that what one observes in the bilayers is a variant form of the true

<sup>1</sup>The idea that such pairs of charged particles can tunnel through a barrier which is non-superconducting faced immense challenge at the beginning, even by some most prominent solid state physicists of that time including J. Bardeen (see [40] and references therein).

<sup>1</sup>For simplicity, this effect will be referred as Josephson effect in the following.

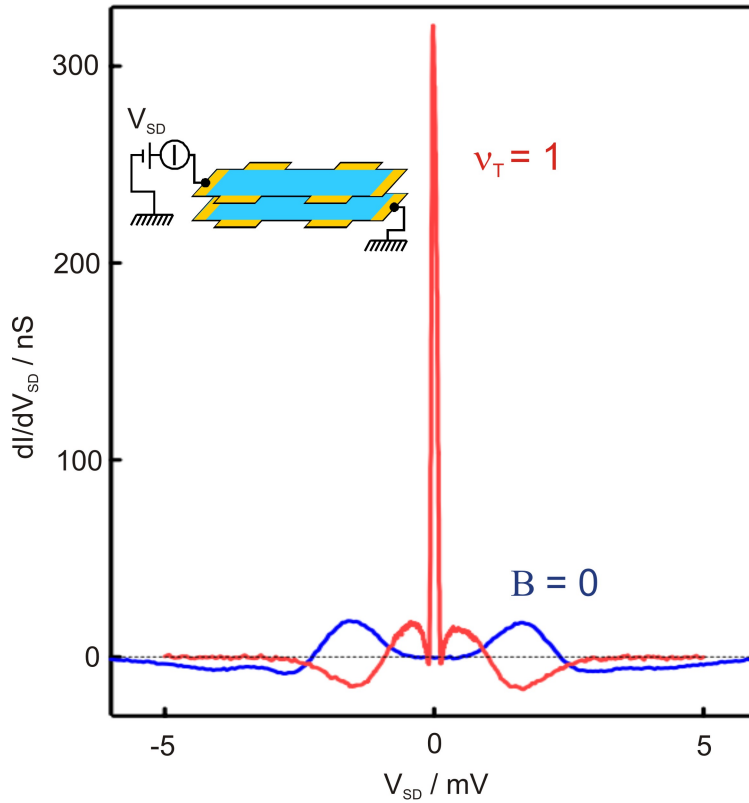


**Fig. 3.9:** Interlayer tunnel conductance at  $\nu_T = 1$  compared to zero magnetic field. Here, the two-terminal conductance is enhanced by a factor of 20 about  $V=0$ . Nevertheless, its height and width remain finite. Modified from [44].

DC Josephson effect with flux flow [47]. Some models point out that the non-occurrence of the DC Josephson effect is due to disorder in form of spatial inhomogeneities [48]. Moreover, as long as tunneling is not perfectly vertical, the before-mentioned quasi-particle current flowing in the plane can also be the source of dissipation by coupling to the merons. At present, no conclusive model has been found which can explain the dissipation.

### Excitonic Counterflow

The supercurrent observed in conventional Josephson junctions is carried by paired electrons. This current is driven by the gradient of phase between the two superconductors, as Eq. 3.10 describes. A similar type of flow has been anticipated by theoretical models also for the  $\nu_T = 1$  bilayers. The difference is that in the latter case, the superflow is carried by electron-hole pairs, instead of electron-electron pairs. This results in a charge-neutral flow of excitons. The first experimental demonstration of such a counterflow is shown in Fig. 3.11 [49] [50]. A longitudi-

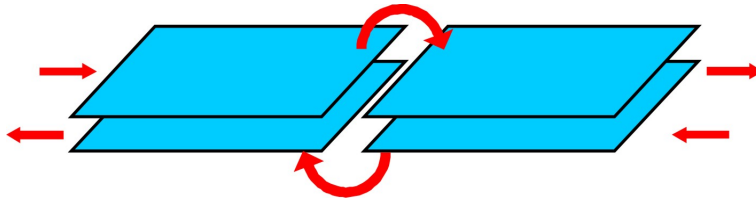


**Fig. 3.10:** Horizontal tunneling geometry proposed by Park et al. Two individual bilayer condensates are linked by a tunnel barrier in serial. In the case when the Josephson tunneling between the layers is suppressed, one has a pure counterflow current between the two bilayer systems. This would demonstrate a true bilayer equivalent of conventional Josephson junctions in BCS-superconductors. Modified from [45].

nal current is applied to one layer, before it is redirected to the other layer via a loop resistor. Hence, the current flows in opposite directions through both layers. The resulting magneto-transport traces exhibit both vanishing longitudinal and Hall resistances in either layer. Thus, the resistivity tensor of the 2DES is zero. This is viewed as an evidence of the theoretical picture of excitonic superfluidity in semiconductor systems.

### 3.4 Critical Josephson Current at $\nu_T = 1$

Besides the observation of a strongly enhanced interlayer tunneling conductance at  $\nu_T = 1$ , a critical interlayer current has been also found in both the tunneling [43] [52] and counterflow configurations [51]. Several models have been proposed to explain the occurrence of such a critical current and its parameter space. All of these models use the pseudospin picture and differ mainly in terms of whether the sample is a clean excitonic superfluid or a disordered one as well as whether the pseudospin vortex field is static or dynamic. Most of the models assume the bilayer to be in the realistic regime of  $\xi \ll \lambda_J$ . Here,  $\xi$  denotes the system's coherence length and describes the length scale over which the interlayer phase coherence is maintained.  $\lambda_J \propto (\rho_s/\Delta_{SAS})$  is the Josephson length, the length scale which the excitonic tunneling current can penetrate into the condensate after being injected from the contacts<sup>1</sup>.

MacDonald et al. have proposed a theory which assumes a clean system [54]. In this theory, the interlayer current enters and leaves the condensate at the hot spot corners and there exists a small region close to the hot spots, in which tunneling is negligible but the pseudospins are

<sup>1</sup>There is also a further theory from Fil et al. which assumes  $\lambda_J \leq \xi$  and assigns the dissipation to Josephson vortices, i.e. vortices that are perpendicular to the 2DES plane [53]. However, the critical current predicted from this theory is much larger than the experimentally observed one.

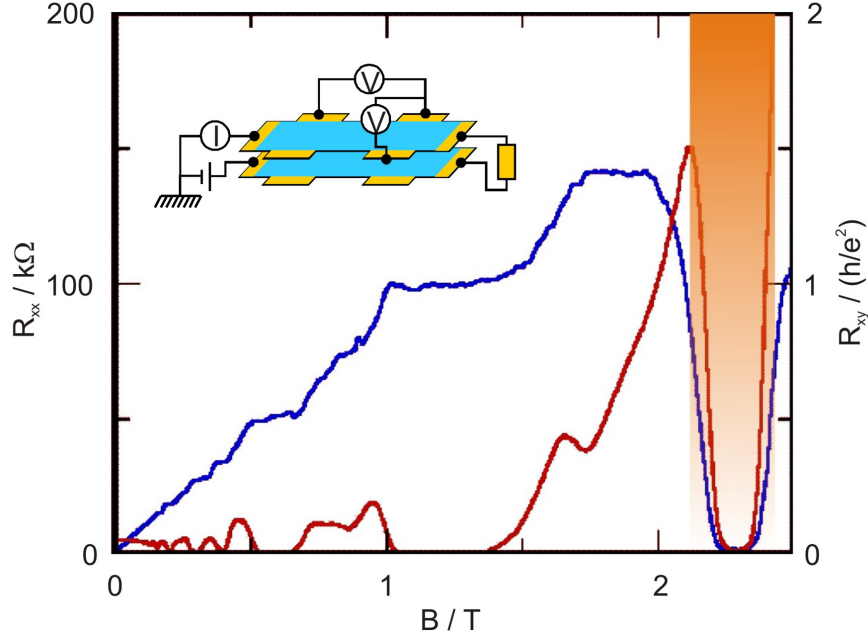


**Fig. 3.11:** Magneto-transport in which current is injected into the lower layer and redirected to the upper layer via a loop resistor, resulting in a counterflowing current. At the  $\nu_T = 1$  state, both the longitudinal (red curve) and the Hall (blue curve) resistances are almost zero, indicating the existence of an excitonic condensate. Modified from [51].

twisted as counterflow takes place. This model makes a more detailed assumption of the total counterflow current as consisting of a quasi-particle component and an exciton component. Within this small (yellow) region shown in Fig. 3.12, the quasi-particle component is converted into the exciton component by the pseudospin transfer torque. In the center of the sample, there exists an interplay between the exciton counterflow and the interlayer tunneling current, where the latter acts as a sink for the former current. The critical current is characterized by the maximal tunneling current when the order parameter  $\phi$  remains static. Depending on the size of the Josephson length  $\lambda_J$  which depends directly on the bare tunneling amplitude  $\Delta_{SAS}$ , the critical current is found in this model to scale differently with parameters such as area and  $\Delta_{SAS}$ : small  $\Delta_{SAS}$  or large  $\lambda_J$  tends to equilibrate the phase angle  $\phi$  over large area of the sample

and coherent tunneling can even be present over the entire sample area, which is qualitatively consistent with the experimentally observed areal dependence of the critical current [52]. To the contrary, large  $\Delta_{SAS}$  or small  $\lambda_J$  will lead to small tunneling region which can be restricted to the hot spot corners. In this case the critical current does not depend on the sample area anymore. Nevertheless, in all regimes from this model, the predicted critical currents are orders of magnitude smaller than the experimentally observed ones. This is explained by taking disorder into account.

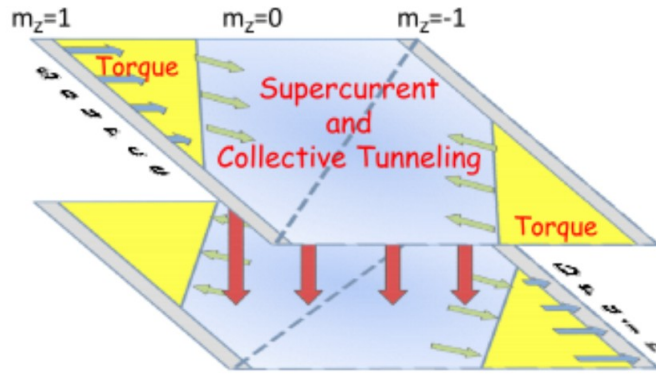


**Fig. 3.12:** The spin-transfer torque model proposed by MacDonald et al. to explain the critical interlayer current in a clean  $\nu_T = 1$  system. At the hot spot corners (yellow region), the injected quasi-particle counterflow current is converted into an exciton counterflow, leading to local twisting of pseudospins. In the center region of the system, tunneling acts as a sink for the supercurrent. Critical current is reached when the order parameter, in this case the pseudospin orientation  $\phi$ , becomes dynamic. From [54].

Eastham et al. have proposed a disorder theory which involves static vortex fields [55]. This means that the disorder-induced vortices (or merons) are pinned. In this model, the occurrence of criticality is accounted for by depinning process, which is due to the charge current injected at the contacts on the edge of the sample. This charge current is normally carried by quasi-particles, which can only flow through the edge channels<sup>1</sup>. However, the model predicts an areal dependence of the critical current. This intriguing result is explained by a self-organizing mechanism: in the bilayer groundstate, the excitonic quasi-superfluid consists of coherent (and ferromagnetic) domains of size  $L_d \sim \frac{\lambda_d^2}{\xi}$  for a two-dimensional system, separated by incoherent regions where the disorder is present. Injecting tunneling current from one end to the opposite

<sup>1</sup>Theoreticians often use edge channel as a generalizing term for the current carrying strips at the  $\nu_T = 1$  state. In reality, these channels should be provided by the incompressible strips described in Sec. 2.1.2.



end of a sample (typically a Hall bar) means injecting a counterflow current which enforces a twisting of the pseudospin compared to equilibrium, thereby giving rise to a finite tunneling current locally. Since the energy cost to twist the pseudospins inside the ferromagnetic domains is too high, the system favors a uniform rotation of pseudospin at the boundary to increase the tunneling current. This process introduces counterflow current further towards the bulk and continues until the tunneling current has saturated at the boundary. The critical current is reached when the tunneling current saturates over all the sample area. Therefore, this model predicts a critical current to scale with the number of coherent domains as

$$I_c \sim \frac{e\rho_s}{\hbar} \frac{A}{L_d^2}. \quad (3.11)$$

Recently, Hyart et al. have proposed a theory including dynamic vortex fields [36]. To the contrary of static vortex fields introduced in the previous model, the dynamics is caused by hopping of thermally activated merons from one puddle to another, which leads to fluctuations of vortex fields. The interlayer tunneling current can interact with such vortex fields, giving rise to a pseudospin correlation that is no longer infinite in time, but decays within a correlation time besides a correlation length. Within their model, the correlation (or coherence) length is estimated to be  $\sim 150$  nm for typical wafers used in the measurements, in good agreement with other theories [46]. It predicts the interlayer coherent tunneling to exist all over the sample plane, which is enabled by counterflow currents between the coherent islands leading to equilibration of the superfluid phase all over the sample. Thus, the critical current should naturally depend on the area of the sample. In addition, it also predicts a quadratic dependence of the critical current on the single-particle tunneling amplitude  $\Delta_{SAS}$ , as seen in

$$I_c \sim \frac{e}{\hbar} \frac{\xi^2 L^2}{\rho_s} \frac{\Delta_{SAS}^2}{l_B^4}. \quad (3.12)$$

The exact mechanism of interaction between the current and the vortex fields is not well known. Nonetheless, this model predicts an intrinsic tunneling resistance due to such interaction, which seems to be consistent with existing measurements which all show a conductance with finite width and peak height. Another feature of this theory is that the  $\nu_T = 1$  state remains unaffected when the injected interlayer current exceeds the critical current, which is consistent to the experimental observation [51]. This is also consistent to the theoretical limit of  $\Delta_{SAS}$  going to zero: in that limit, no Josephson-like tunneling can be experimentally observed, while the spontaneously broken symmetry persists.



# Chapter 4

## Quantum Hall Breakdown in Interlayer Tunneling

The Josephson-like interlayer tunneling in quantum Hall bilayers at the  $\nu_T = 1$  state has been introduced in Sec. 3.3. To our knowledge, this coherent tunneling phenomenon has been studied excessively in samples with relatively large barrier thickness, ranging from 10 nm to 12 nm. This has the consequence that the interlayer tunneling strength in those samples was relatively weak, i.e. about  $10 \mu\text{K} \sim 100 \mu\text{K}$  [42] [43]. Furthermore, the correlation between the Josephson tunneling and the longitudinal (in-plane) transport has not been discussed so far. In this chapter, we extend the samples to include barrier thickness decreased to 8 nm, with dramatically increased coherent tunneling at  $\nu_T = 1$ . Experimental results including three Hall bar samples will be compared. These samples share the same geometry as shown in Fig. 4.1, but differ in their barrier thickness. The data will be discussed, followed by conclusions at the end.

### 4.1 Measurement Results

In this section, interlayer and longitudinal transport measurements which involve three Hall bar bilayer samples with different barrier thicknesses will be shown. In all measurements, the electron densities of the layers have been balanced and a corresponding magnetic field has been applied so that the  $\nu_T = 1$  state is well established at a sample temperature of  $\leq 15 \text{ mK}$ <sup>1</sup>. The measurements were performed using standard DC sources and preamplifiers.

---

<sup>1</sup>In the following of this work, if not further specified, all the temperatures are referring to the mixing chamber temperature read from a *Cernox* temperature sensor close to the sample position.

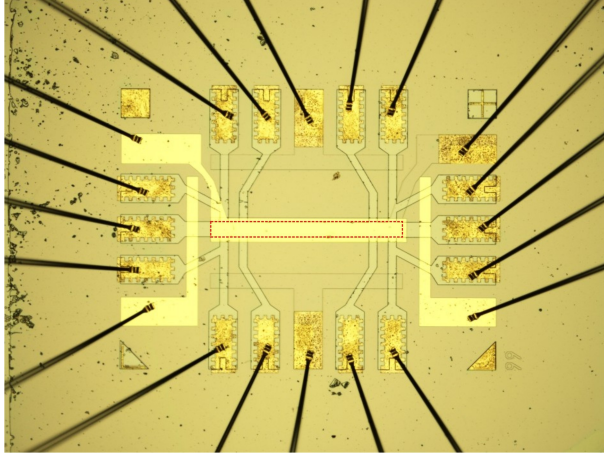


**Fig. 4.1:** Sample structure of all Hall bar samples used in this work. The length of the active region (marked by red dashed line), i.e. the region covered by the global front and back gates defining the area of  $\nu_T = 1$ , is  $880 \mu\text{m}$  and its width  $80 \mu\text{m}$ . Details to sample fabrication see Sec. B.1.

### Interlayer Tunneling with varied Barrier Thickness

Fig. 4.2 summarizes the interlayer tunneling in three Hall bar samples, which have the same mesa geometry (as shown in Fig. 4.1) and only differ in the barrier thickness. The three samples are labeled HB-12 from wafer #82018, HB-10 from wafer #81653 and HB-8 from wafer #81981. The barrier thickness in these three wafers is 8 nm, 10 nm and 12 nm, respectively, which are indicated by the numbers in their labels. The details about sample fabrication and low temperature measurement techniques are summarized in App. B. As shown in (a), the interlayer current is injected from one end of the first layer and taken out from the opposite end of the second layer. Here, the current is measured by dividing the voltage drop across a resistor of  $1 \text{ M}\Omega$  (not shown). The DC voltage source itself is connected to an RC-filter with an inner resistance of  $1 \text{ M}\Omega$  (not shown). The circuit resistance is thus  $2 \text{ M}\Omega$ .

The four terminal tunneling I-V characteristics are shown in (c) with the same voltage scale but different current scales. Both the up and down sweeps are shown in all three samples. Sample HB-12 and HB-8 exhibit similar results to those reported earlier. At  $d/l_B \sim 1.45$ , the critical current of sample HB-12 is about  $2.3 \text{ pA}$  in each direction, while at a similar  $d/l_B$  value sample HB-10 has a critical current of  $1.5 \text{ nA}$  in each direction, hence three orders of magnitude larger. The zero bias interlayer resistance of sample HB-12 is about  $10 \text{ M}\Omega$ , which is also three orders of magnitude larger than that of sample HB-10 ( $\sim 10 \text{ k}\Omega$ ). Furthermore, sample HB-10 exhibits jumps after reaching its critical current. Sample HB-8 shows a critical current of  $25 \text{ nA}$  in each direction at  $d/l_B \sim 1.68$ . After reaching the critical current, the current does not decrease as is

the case in the other two samples. Instead, it continues to increase and flattens at even higher interlayer voltages. No jumps is seen here beyond the critical current. Its interlayer resistance at zero bias is about  $1 \text{ k}\Omega$ .

## Longitudinal Transport vs. Interlayer Tunneling

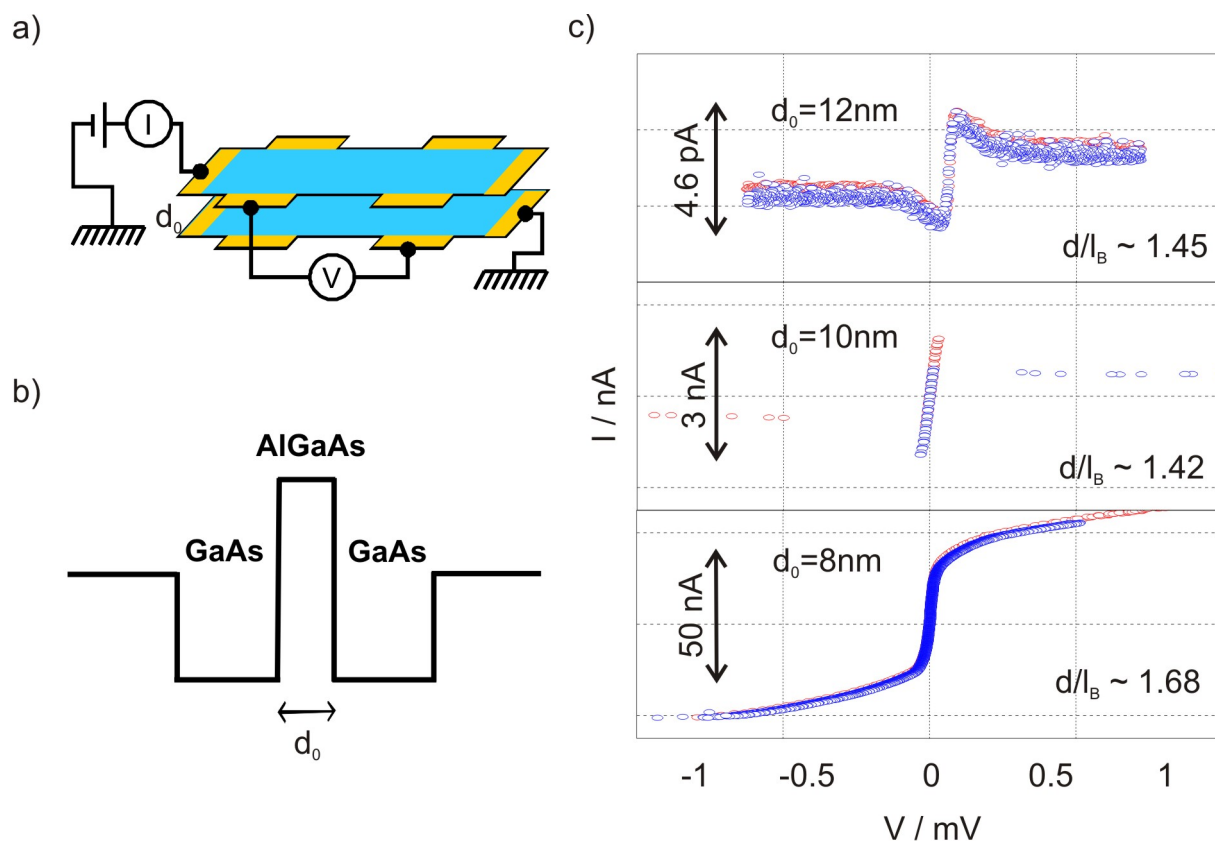
The barrier thickness in bilayers has a strong effect on the interlayer resistance and the size of the critical current at  $\nu_T = 1$ . Hence, the effect of (longitudinal) transport in the plane will be different since the ratio between the sheet resistance of each layer and the tunneling resistance will vary. Here, we show in-plane transport and interlayer tunneling measurements on two samples: HB-10 and HB-8.

Fig. 4.3 shows tunneling and longitudinal transport in sample HB-10. At  $\nu_T = 1$ , the  $d/l_B$  ratio is set to 1.66. In (a), the inset shows that the interlayer tunneling current is driven across the sample plane. The tunneling I-V curve includes both up and down sweeps and exhibits a critical current of  $0.5 \text{ nA}$  and an interlayer resistance of  $50 \text{ k}\Omega$ . Figures (b) and (c) show the in-plane transport in the upper and lower layer, respectively. One observes a critical behavior in both curves: below a current of  $10 \text{ nA}$  in both directions, the longitudinal voltage remains relatively small, whilst above this value the voltage increases dramatically. The slope of each I-V curve within the critical regime gives the longitudinal resistance of each layer. Being qualitatively the same, both layers show difference in their longitudinal resistances: the upper layer has a resistance of  $10 \text{ k}\Omega$ , while that of the lower layer is about a factor of 3 larger.

Fig. 4.4 summarizes the interlayer tunneling and in-plane transport in sample HB-10 at four different  $d/l_B$  values, from 1.42 to 1.66. In each panel, the black curve shows the interlayer tunneling, while the red and blue curves show the transport in the upper and lower layer, respectively. As the main graphs show, the critical tunneling current increases with decreasing  $d/l_B$ , consistent with reported measurements [43]. Moreover, in all cases, the critical tunneling current is significantly smaller than the critical current in the plane, as shown by the insets. Besides the slope of the tunneling I-V curve, the slope of the I-V curves of in-plane transport also increases with decreasing  $d/l_B$  ratio. At  $d/l_B = 1.42$ , the transport in the upper layer shows some abrupt changes close to the critical current.

Now we turn to sample HB-8 with smaller barrier thickness. In Fig. 4.5, interlayer tunneling and in-plane I-V characteristics are presented for  $\nu_T = 1$  at  $d/l_B = 1.68$ . In contrast to sample HB-10, where the tunneling I-V characteristic is largely different from that of the in-plane transport, all the four panels show similar I-V curves in this case. Most surprisingly, the critical current observable in all circuit configurations is the same at  $\sim 25 \text{ nA}$ .

From the slopes of the I-V curves, one can determine the resistance in each configuration. The interlayer tunneling resistance is about  $1 \text{ k}\Omega$  and close to the sheet resistance of the upper layer, which is slightly smaller than that of the lower layer. Both sheet resistances are smaller



**Fig. 4.2:** Interlayer tunneling in three Hall bar devices which share the same geometry but differ in barrier thickness. In (a), the tunneling circuit configuration is shown where tunneling current is passed to flow across the sample plane. The inner resistance of the circuit is  $2 \text{ M}\Omega$  (not shown). In (b), the schematic diagram of the conduction band of the bilayer is shown. In (c), the I-V characteristics of samples HB-12 (upper), HB-10 (middle) and HB-8 (lower). The barrier width, indicated by the label numbers, is varied from 12 nm to 10 nm and 8 nm, respectively. All three curves are shown using the same voltage scale but different current scales.

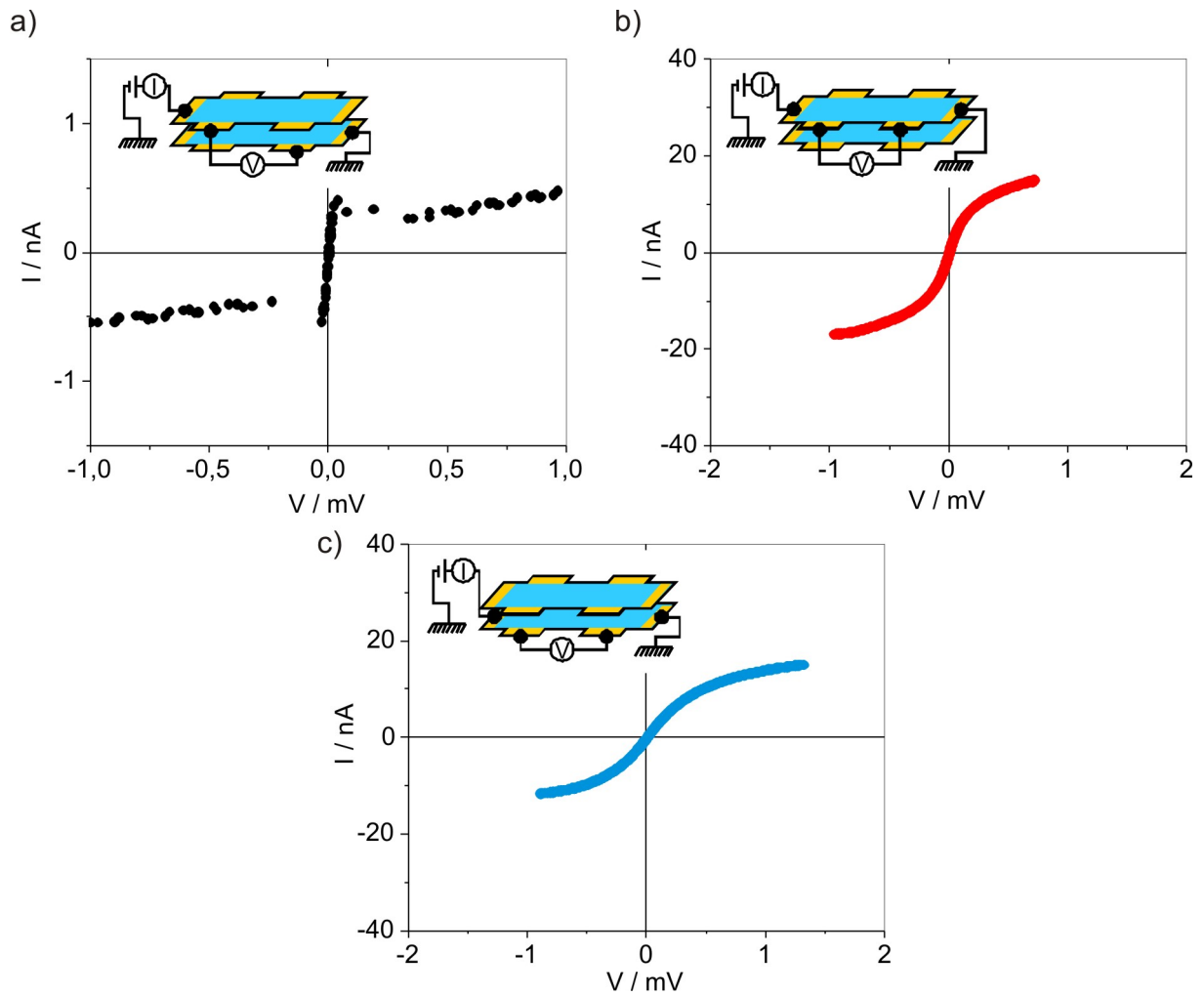


**Fig. 4.3:** Interlayer tunneling compared with longitudinal transport through the upper and lower layer in sample HB-10. The effective layer spacing  $d/l_B$  is set to 1.66 at  $\nu_T = 1$ . The insets show the circuit configuration corresponding to each curve.

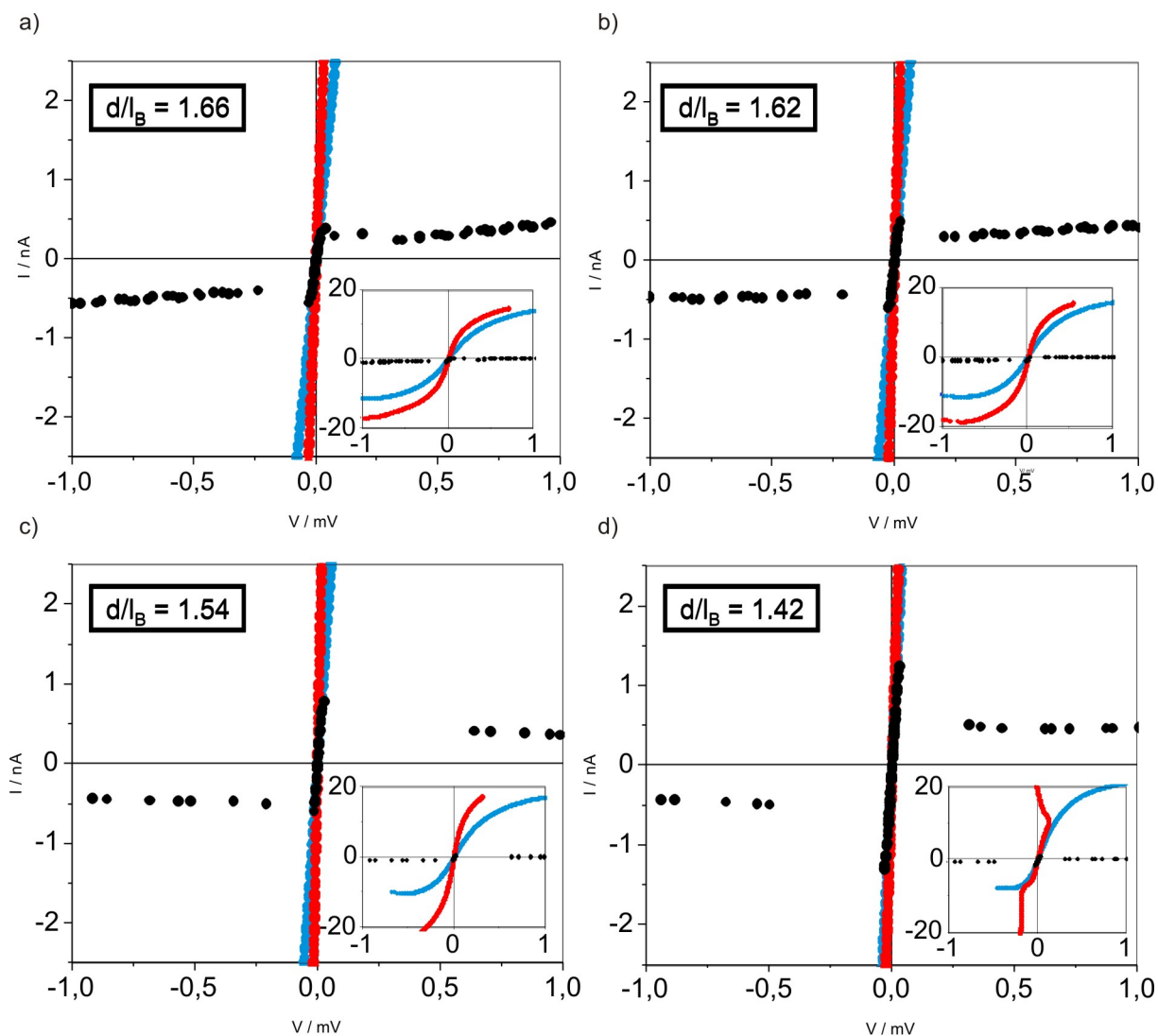


**Fig. 4.4:** Interlayer tunneling (black) compared with longitudinal transport through the upper (red) and lower (blue) layer in sample HB-10. The effective layer spacing  $d/l_B$  is varied between 1.42 and 1.66. Insets: full traces of in-plane transport through both layers separately. In all cases, the critical tunneling current is much smaller than the critical current in in-plane transport.



compared to the case when the two layers are unseparated, shown in (d).

A summary of the same measurements at different  $d/l_B$  values is also shown for sample HB-8 in Fig. 4.6. The behavior seen at  $d/l_B = 1.68$  is qualitatively reproducible at other  $d/l_B$  values: in all panels, the critical current in tunneling is comparable to the critical current in the plane. The size of the tunneling (black) critical current is the highest at  $d/l_B = 1.68$ , where the interlayer resistance is the lowest. This seems to indicate that the  $\nu_T = 1$  state is best established at this  $d/l_B$  ratio. The upper layer has a lower resistance than the lower layer. The difference between the two layers becomes clearer at lower  $d/l_B$  ratios, where the lower layer exhibits an almost ohmic behavior. The tunneling resistance is between the two sheet resistances except at  $d/l_B = 1.8$ , where it is slightly smaller than the upper layer sheet resistance.

If one compares the two samples, HB-10 and HB-8, at similar  $d/l_B$  ratios  $\sim 1.7$ , they show significantly different behaviors in interlayer tunneling, since the critical currents in the tunneling contact configuration applied differ by a factor of 100. Nevertheless, the behaviors in transport along the sample plane remain qualitatively similar in both samples. It is remarkable that the change in barrier width and consequently in the tunnel coupling between the layers seems to have only a minor effect on the longitudinal transport, while it has a strong effect on the Josephson-like tunneling.

In order to study the role of longitudinal transport in tunneling, we have measured the interlayer tunneling with an alternative contact configuration. In Fig. 4.7, the black curves in (a) and (b) show the interlayer tunneling using the same contact configuration applied, which is also depicted in the lower circuit in each panel. The red curves have been obtained when the upper circuit is used for both samples. In this case, the interlayer current is injected into a contact that is situated directly above the contact, from which this current is taken out again. The interlayer voltage is measured with two contacts that are also directly above each other. In sample HB-10, the two contact configurations result in difference in both the critical current and the interlayer resistance. The critical current is increased from 1.3 nA to 1.6 nA and the tunneling resistance decreased from 16 k $\Omega$  to 4 k $\Omega$  from the lower to the upper configuration. In sample HB-8, the differences are even much larger. While the change in tunneling resistance is similar to that in sample HB-10, the critical current is increased to exceed the order of 1  $\mu$ A, i.e. by a factor of 50. In addition, the interlayer tunneling using the upper configuration also shows negative differential resistance when approaching its critical current.

## 4.2 Data Analysis and Discussion

The results presented in the previous section will be analyzed and discussed here. First, we focus on the effect of barrier thickness on the interlayer tunneling. Then, we look at the interplay between the interlayer tunneling and in-plane transport in two samples, HB-10 and HB-8 and

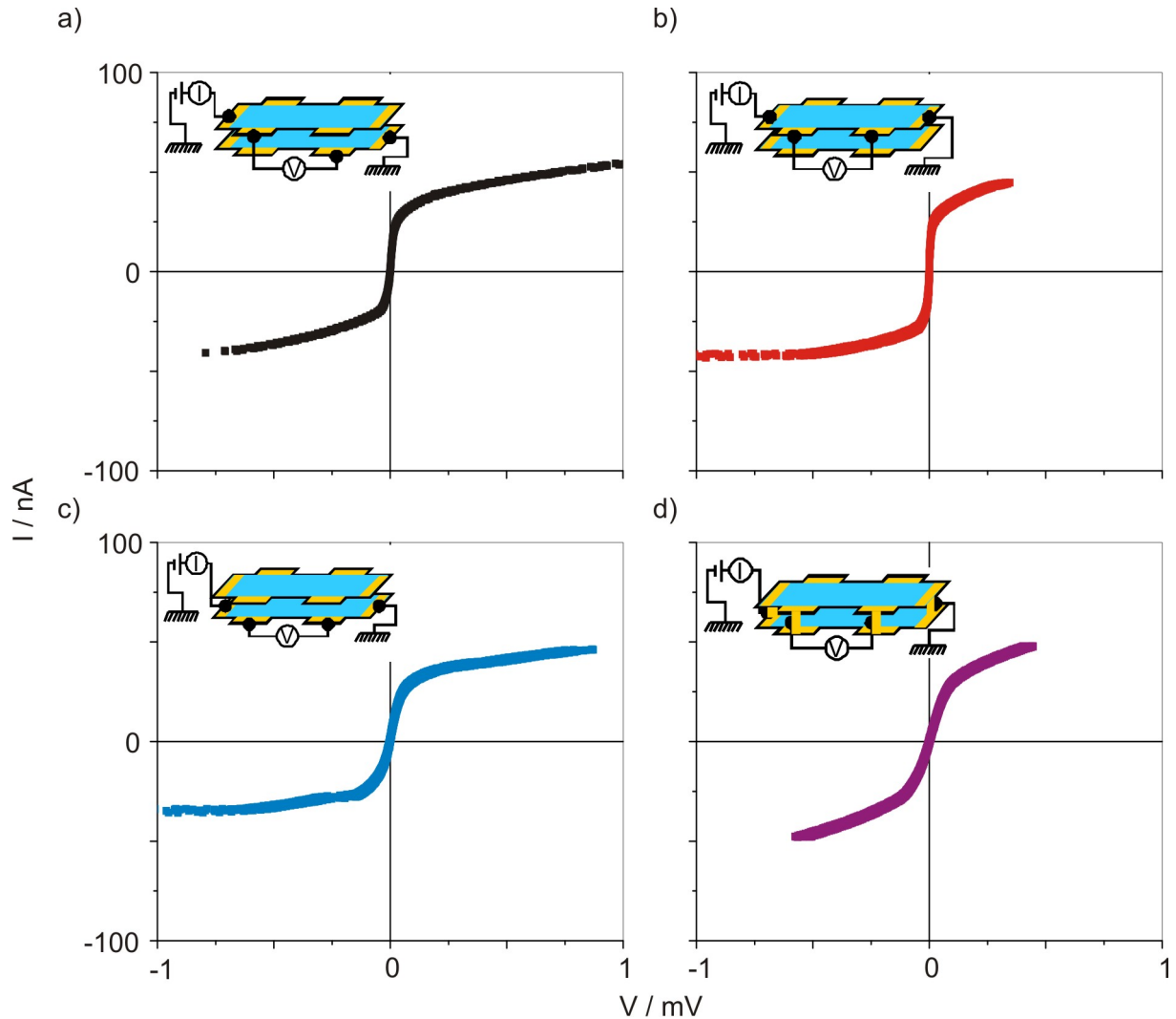


**Fig. 4.5:** Interlayer tunneling compared with longitudinal transport through the upper and lower layer as well as through both layers simultaneously in sample HB-8. The effective layer spacing  $d/l_B$  is set to 1.68 at  $\nu_T = 1$ . The insets show the circuit configuration corresponding to each curve. Note that the contacts in the inset in (d) are connecting both layers.

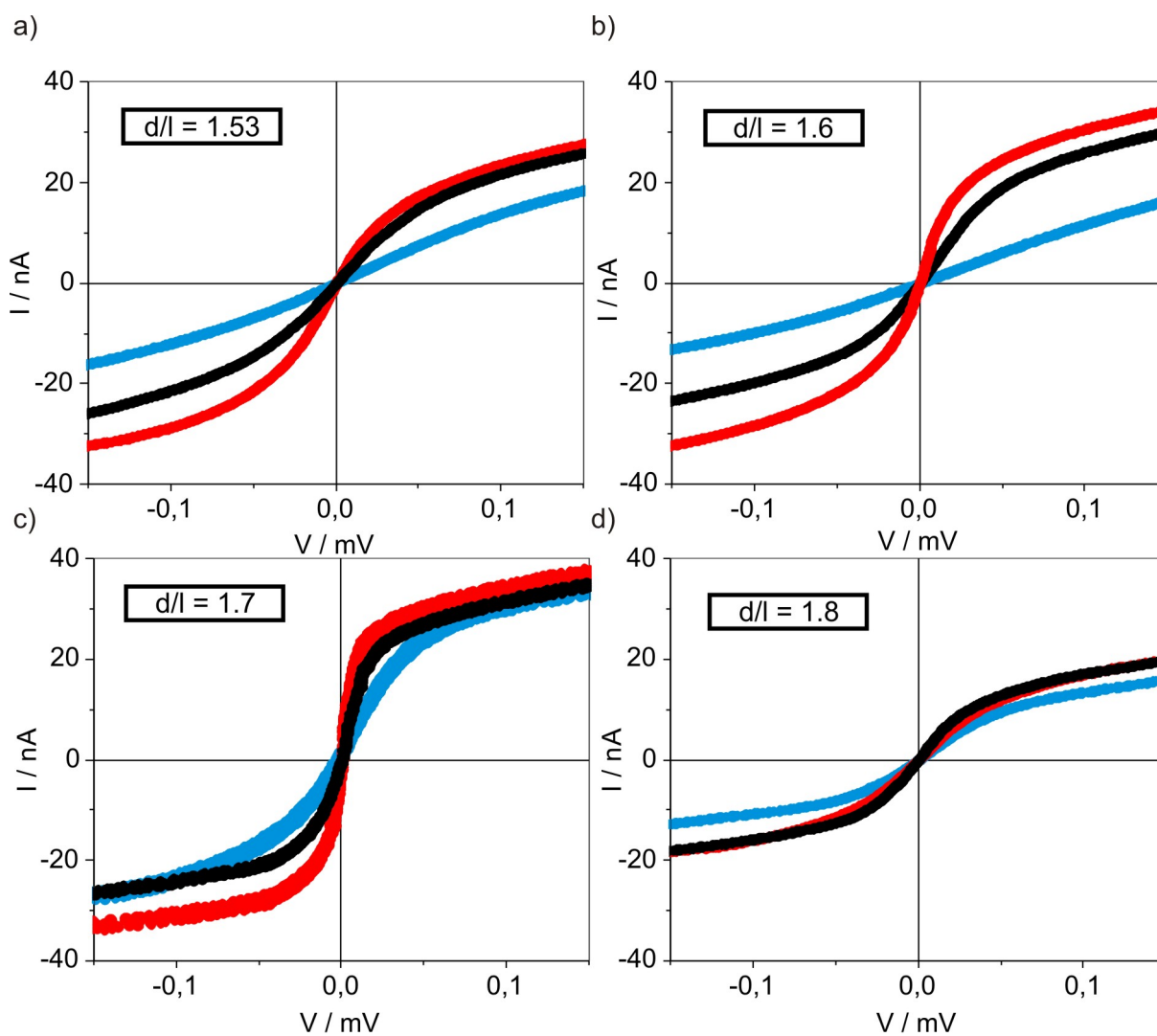


**Fig. 4.6:** Interlayer tunneling (black) compared with longitudinal transport through the upper (red) and lower (blue) layer in sample HB-8. The effective layer spacing  $d/l_B$  is varied between 1.53 and 1.68. In all cases, the critical tunneling current is comparable to the critical current in in-plane transport.

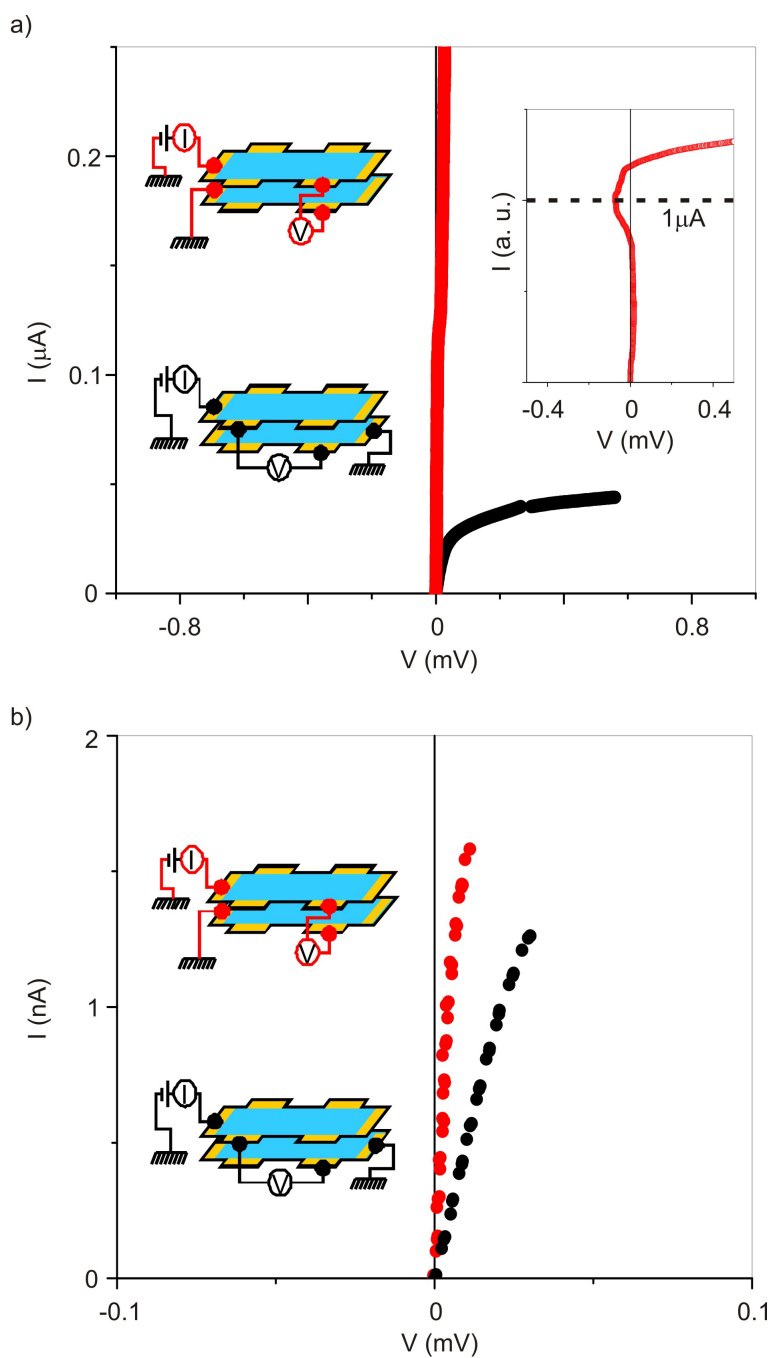


**Fig. 4.7:** Interlayer tunneling characteristics with two different contact configurations in Hall bar device HB-8 (panel (a)) and HB-10 (panel (b)). The black/red curves have been obtained when using the lower/upper contact configuration. In (a), a significant difference in critical current can be observed between the two contact configurations, whilst there is only a minor difference in (b). Inset of (a): a gigantic critical current exceeding  $1\mu\text{A}$  is observed in sample HB-8 for the upper configuration.

discuss a possible picture of the breakdown of  $\nu_T = 1$  QHE.

### Role of Barrier Thickness

At first glance, the three Hall bar samples shown in Fig. 4.2 do not vary largely in their barrier thickness, which is only 20%~25%. Nevertheless, the symmetric-antisymmetric energy gap,  $\Delta_{SAS}$ , changes by a significantly larger factor with such small changes in barrier thickness. The  $\Delta_{SAS}$  gap is a measure for the strength of tunnel coupling (or tunneling probability) in bilayer systems. As explained in Sec. 3.3, its value can be determined from the tunneling I-V characteristic at  $B=0$  T. This has been done for both wafers #81653 (10 nm barrier) and #81981 (8 nm barrier), yielding values of  $\sim 150$   $\mu\text{K}$  and  $\sim 1$  mK, respectively<sup>1</sup>. For wafer #82018, the experimental value of  $\Delta_{SAS}$  is still missing. However, based on the above mentioned analysis [36], the gap is estimated to be 1~10  $\mu\text{K}$  for a similar system.

Among the theoretical models concerning the relation between tunneling critical current  $I_c$  and the  $\Delta_{SAS}$  gap, the one provided by Hyart et al. [36] claims that  $I_c$  scales quadratically in  $\Delta_{SAS}$  and linearly in the area of the  $\nu_T = 1$  system, i.e.  $I_c \propto A \cdot \Delta_{SAS}^2$ . The authors point out that their model is best applicable to samples with small  $\Delta_{SAS} \leq 10$   $\mu\text{K}$ . This has to do with the large tunneling resistance associated with a small  $\Delta_{SAS}$ . When the tunneling resistance is the dominant resistance in the entire circuit, tunneling can be viewed as homogeneous in the sample. Nevertheless, the model also works well for samples with  $\Delta_{SAS} \sim 100$   $\mu\text{K}$ . This might explain the scaling of the observed critical currents  $I_c$  in sample HB-12 and HB-10 with the estimated  $\Delta_{SAS}$ :  $I_c$  increases by a factor of 1000 while  $\Delta_{SAS}$  increases by a factor of between 10 and 100.

Furthermore, comparing the tunneling I-V characteristics of sample HB-10 and HB-8 at  $d/l_B \sim 1.7$  (Fig. 4.3 a) and Fig. 4.5 a)), one also finds that the quadratic dependence on  $\Delta_{SAS}$  seems to hold. Here,  $I_c$  increases by a factor of 50 while  $\Delta_{SAS}$  increases by a factor of  $\sim 10$ . Nevertheless, it is not known whether this can be taken as evidence that the above mentioned model extends its applicability to samples with such a large tunneling probability.

The occurrence of jumps beyond reaching the critical current can be explained by bistability. Fig. 4.8 shows the tunneling current as a function of both the two-terminal and the four-terminal voltage, taken from sample HB-10 at  $d/l_B = 1.42$ . When the 2-terminal interlayer voltage continues to increase after  $I = I_c$ , it tries to increase the interlayer current. However,  $I$  is strongly suppressed after its critical value, since the bilayer system is now highly ohmic. One thus has to do with two competing effects. This bistability becomes strong, when the tunneling resistance is much smaller than the circuit resistance. Fig. 4.8 demonstrates such a case: the tunneling current is shown as a function of both the two-terminal and the four-terminal voltage, taken from

<sup>1</sup>The value for wafer #81653 is obtained from earlier work [56], while the one for wafer #81981 is obtained using a separate sample within this work.

sample HB-10 at  $d/l_B = 1.42$ . The slope of curve in (a) corresponds to a circuit resistance of  $\sim 2.5 \text{ M}\Omega$ , which is much larger than the tunneling resistance of  $\sim 10 \text{ k}\Omega$  observable from the slope in (b). For sample HB-8, the tunnel resistance is much larger than the circuit resistance, which results in a smooth transition after the current has reached its critical value.

Sample HB-8 has an even much smaller tunneling resistance than sample HB-10. Nonetheless, its tunneling I-V characteristic does not show any jump or hysteresis between different sweeps. The reason will become clear in the following.

## Interplay between Tunneling and In-Plane Transport

Based on the tunneling contact configuration shown in the inset of Fig. 4.3 a), it is intuitive to assume that the transport in the longitudinal direction also plays a role in the tunneling. However, the critical tunneling current in sample HB-10 is an order of magnitude smaller than in the in-plane transport. This shows that there exists no intrinsic coupling between the tunneling critical current and the longitudinal critical current.

The slope of the I-V characteristic in Fig. 4.3 b) and c) gives the differential conductance of the upper and lower layer, respectively. At  $I \sim 10 \text{ nA}$ , the differential conductance drastically decreases, which marks an onset of critical behavior. Such a phenomenon is essentially understood as the breakdown of quantum Hall effect. While there exist some pictures in analogy to the breakdown of QHE breakdown in single quantum wells, the actual mechanism, which leads to the  $\nu_T = 1$  breakdown, is currently not yet well understood.

The contact configurations in these two measurements are similar to the one used in studying the Coulomb drag effect at  $\nu_T = 1$ , which has been introduced in Sec. 3.3. The Coulomb drag has been studied in detail theoretically [54]. One can thus apply a picture concerning the composition of currents in each layer to the in-plane measurements in this chapter. Fig. 4.9 shows a cartoon of this picture. Let us first clarify the terminology: the layer, in which the current is applied, is denoted the *drive* layer, while the adjacent layer is the *drag* layer. The total current  $I_{total}$  applied to the drive layer can first flow as a quasi-particle current, which is layer symmetric.

According to the model of MacDonald et al. [54] introduced in Sec. 3.3, this layer symmetric current can undergo a conversion into a layer anti-symmetric current, which is a counterflow current carried by bilayer excitons. Under the assumption, that the current composition does not change on the onset of dissipation, one can apply this model for a clean system also for the current case. The current conservation in the drive and drag layers lead to

$$I_{drive} = I_{S,drive} + I_{AS} = I_{drive}^{QP} + I^{EX} = I_{total} \quad (4.1)$$

$$I_{drag} = I_{S,drag} - I_{AS} = I_{drag}^{QP} - I^{EX} = 0. \quad (4.2)$$

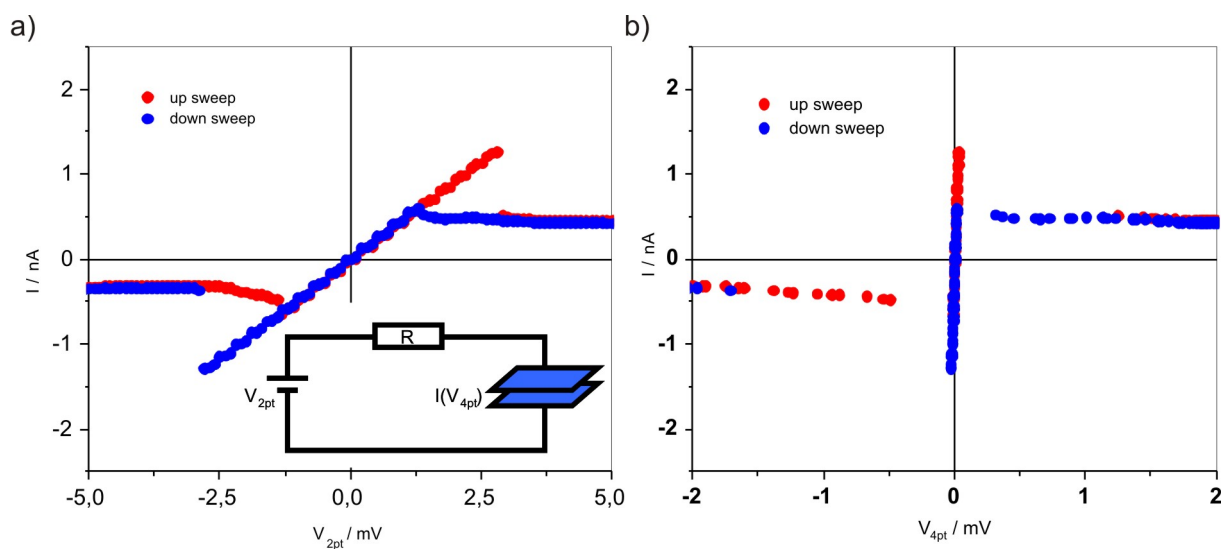


**Fig. 4.8:** Interlayer current as a function of the two-terminal voltage in (a) and four-terminal voltage in (b), measured in sample HB-10 at  $d/l_B = 1.42$ . Bistability leads to the jumps after the critical tunneling current as well as hysteresis between up and down sweeps. Inset: the effective circuitry with  $R$  being the circuit resistance.

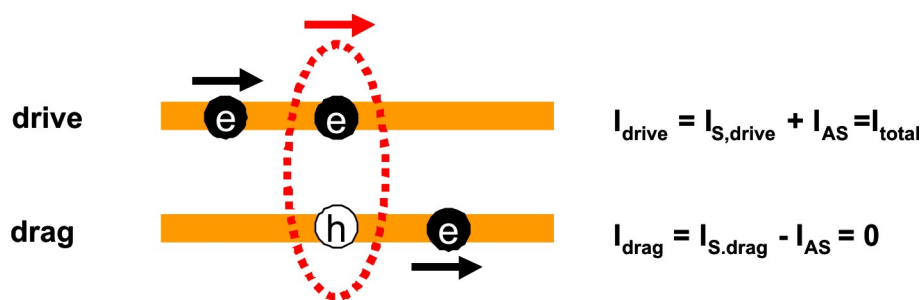


**Fig. 4.9:** Illustrative explanation of the Coulomb-drag effect: current is only applied in one of the bilayers, while the Hall potential can be detected in both layers. The total current in both layers can be thought of consisting of two components: a layer symmetric quasi-particle current and a layer antisymmetric exciton current.

Here,  $I_{S,drive} = I_{drive}^{QP}$  is the layer symmetric quasi-particle current in the drive layer and  $I_{S,drag} = I_{drag}^{QP}$  the same current in the drag layer.  $I_{AS} = I^{EX}$  is the layer anti-symmetric exciton current. Summing up both equations, one yields

$$I_{drive} + I_{drag} = I_{drive}^{QP} + I_{drag}^{QP} = I_{total}. \quad (4.3)$$

Within this picture, the total current applied in either case is the sum of the quasi-particle current flowing in both layers combined. If one takes into account that exciton current flows as a nearly dissipationless current, one would not expect the exciton current to lead to a breakdown which usually involves dissipative transport. In this sense, the equal critical current measured in both layers at the breakdown possibly reflects that indeed the layer symmetric quasi-particle current leads to breakdown of the  $\nu_T=1$  QHE.

The in-plane transport measurements performed in sample HB-8 essentially confirms the qualitative picture above. The critical currents in both the upper and lower layers, shown in Fig. 4.5 b) and c), are about 25 nA. Furthermore, in (d), where the two layers are not separated, one observes also the same in-plane critical current as in the two other measurements. Due to the charge neutrality of bilayer excitons, one can only detect the quasi-particle current in this configuration. Hence, the same critical current here as in single layer measurements means that the same amount of quasi-particle current is required to reach breakdown of the  $\nu_T = 1$  QHE, which remains the same in all three measurements. The slope in (d) is larger than in (b) and (c). This might be due to the fact that in the single layer transport one is only measuring the conductance of one layer, in which both quasi-particle and exciton currents flow. In (d), the conductance is given only by quasi-particle currents.

The interlayer tunneling in sample HB-8 exhibits the same critical current as in the in-plane measurements. There can be three explanations: i. due to coupling of the in-plane transport to the interlayer tunneling; ii. due to coupling of the interlayer tunneling to the in-plane transport; iii. due to coincidence. If there exists an intrinsic coupling of the in-plane transport to the interlayer tunneling, it would be difficult to explain the observations in sample HB-10, since there the critical longitudinal current is an order of magnitude larger than the critical tunneling current. Using the same argument, there can also be no intrinsic coupling of the critical current in tunneling to that in in-plane transport. If it would be a coincidence, it would also be difficult to explain that at different  $d/l_B$  ratios similar observations can be made. Based on the tunneling contact configuration, in which the tunneling current is forced to flow in the sample plane, it is more likely that the tunneling critical current observed in sample HB-8 is an effect of the breakdown.

The results shown in Fig. 4.7 seems to confirm the above assumption. For sample HB-8, the two tunneling contact configurations result in a significant difference in critical current. If the tunneling in the lower configuration would be independent on the in-plane transport, but



consequence of some intrinsic property, one would not expect such a large difference when switching to the upper one. In other words, we can conclude that the critical tunneling current observed in Fig. 4.5 and Fig. 4.6 is a consequence that the Josephson-like tunneling is limited by the breakdown happening in the plane. This is possible because the breakdown current, which is similar in both samples HB-10 and HB-8, is smaller than the intrinsic critical Josephson current in sample HB-8, but larger in sample HB-10.

This also means that the difference between the two configurations is essentially that the lower one involves transport in the plane while the upper one seems not to. Fig. 4.10 illustrates this in terms of the Andreev reflection (AR) mechanism. The situation in (a) corresponds to the upper configuration: the interlayer current is injected via the AR process directly, after which the electron-hole pairs can propagate as an excitonic counterflow inside the sample. To the contrary, the AR process in (b) takes place, accompanied by a transport current in the plane (indicated by the blue arrows). The Josephson current is thus forced to flow as a quasi-particle current along the sample plane. Based on the knowledge that the  $\nu_T = 1$  breakdown is most likely an effect of the quasi-particle current in the plane, the same quasi-particle current should also lead to breakdown in the tunneling here. This is consistent to the observation that a much larger exciton current in sample HB-8 in the second configuration does not lead to any breakdown.

It is also notable that the interlayer resistance in both samples remains finite even when tunneling essentially does not involve quasi-particle transport in the plane. This result indicates that such a resistance is intrinsic for the tunneling. The source of dissipation leading to a finite tunneling resistance is still an open question. Nonetheless, theoretical models taking into account dissipative processes like those introduced in Sec. 3.3 seem to agree that merons interacting with the tunneling current play the central role. In the static vortex field picture, the merons always remain pinned to the peak or valleys of the disorder potentials, depending on the sign of charge they carry. It is therefore difficult to explain dissipation even before reaching the critical current in this picture. In the picture where the vortex field is assumed to be dynamic, on the other hand, the merons can interact with the tunneling current. More precisely, both the exciton and the quasi-particle current can mobilize the merons and give rise to an increase of current. This mechanism might be the origin of the observed intrinsic interlayer resistance.

The critical current exceeding the order of  $1 \mu\text{A}$  in the upper configuration in Fig. 4.7 a) is intriguing. If one assumes that the estimated  $\Delta_{SAS}$  is independent on the contact configuration, this critical tunneling current is larger than expected from the quadratic  $\Delta_{SAS}$  dependence by a factor of  $\sim 20$ . The quadratic correlation comes out from a theory which treats tunneling perturbatively. Taking into account that the tunneling resistance is not dominant over the system's in-plane resistance anymore, the interlayer voltage distribution in the plane might become inhomogeneous and start to play an important role in describing the tunneling current. This feature is not considered in the perturbative model [36] and it is not expected that it will be suitable

for samples with such strong tunnel coupling as HB-8. On the other hand, the model provided by Eastham et al. [55] might explain the size of the critical current. Under application of the Josephson length  $\lambda_J = \sqrt{4\pi l_B^2 \rho_s / \Delta_{SAS}}$  [36], Eq. 3.11 can be rewritten as

$$I_c \sim \frac{e\rho_s}{\hbar} \frac{A}{L_d^2} = \frac{e \cdot A \cdot \xi^2 \cdot \Delta_{SAS}^2}{16\pi^2 \cdot \hbar \cdot l_B^4 \cdot \rho_s}. \quad (4.4)$$

If one uses  $\Delta_{SAS} \sim 1$  mK and assumes the parameters determined by Hyart et al. [36], namely a coherence length  $\xi \sim 150$  nm and a pseudospin stiffness  $\rho_s \sim 0.4$  K<sup>1</sup>, one obtains a critical current of  $I_c \simeq 10$   $\mu$ A, which is in the same order of magnitude as observed. Since this model does not provide an exact prediction but rather a proportionality, it is difficult to judge its applicability. Nevertheless, this reasonable matching indicates that the pseudospin vortex field (or merons) should be static. This is likely to be the case in the absence of a sufficiently large quasi-particle current. The critical tunneling current of  $\sim 25$  nA observed in the other configuration, however, agrees very well with the quadratic  $\Delta_{SAS}$  dependence. This might mean that the merons are mobile in this case, which arises probably due to interaction with the quasi-particle current.

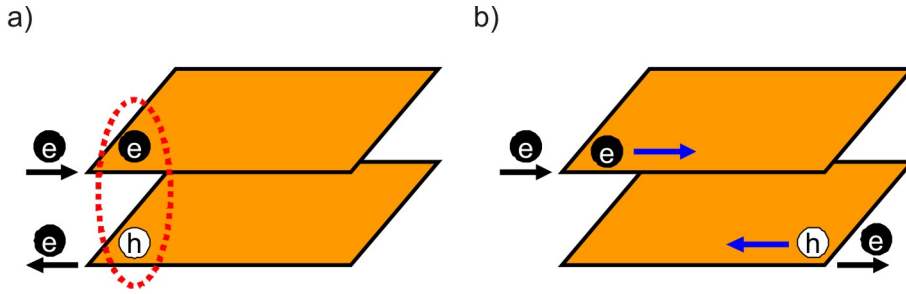


**Fig. 4.10:** Schematic demonstration of the Andreev reflection mechanism in the two contact configurations depicted in the insets of Fig. 4.7. (a): When the source and drain contacts are situated directly above each other, the charge carriers can form excitons upon injection into the exciton condensate. (b): When the source and drain contacts have a horizontal distance, the charge carriers injected into the condensate form excitons while flowing as a quasi-particle current.

Nevertheless, it should be pointed out that the microscopic details of the interlayer current in the new configuration are not well-known. In particular, the origin of the negative differential resistance appearing close to the critical current is not identified. Such an observation is not made in sample HB-10 with thicker barrier. It is possible that in that case the interlayer resistance is

<sup>1</sup>The choice of these parameters is based on the excellent matching between the model and multiple independent experimental data.

the dominating one whilst in sample HB-8 both interlayer and in-plane resistances are comparable. In the latter situation, the current distribution might be complex and depends on the ratio between both resistances locally. Comparable observations have been made in superconducting junctions [57].

Finally, our results of in-plane transport show that the breakdown currents in different samples have similar size, although the tunnel coupling as well as the critical tunneling current largely differ between them. The detailed mechanism, which leads to dissipation and eventually breakdown of the  $\nu_T = 1$  QHE is not yet understood. Nevertheless, under the light of the interaction between merons and quasi-particle current, the similar breakdown current can be interpreted as a consequence of similarity in the disorder potential induced by doping inhomogeneities. The distribution of disorders might be similar in the two wafers, from which sample HB-10 and HB-8 are extracted. Theoretically, this disorder potential will give rise to a separation of the bilayer system into domains, in which the phase coherence is present. The size of such coherent domains as well as the distance between them should consequently be comparable in both samples. Hence, if the nature of the interaction itself between the merons and the quasi-particle current does not change with the lateral structure of the bilayers, one should indeed expect two comparable breakdown currents.

Similar to the case of single layers, the quasi-particle current is theoretically believed to flow along the incompressible stripes in the bilayers at  $\nu_T = 1$ . Such incompressible strips have, nonetheless, not yet been verified. If the bilayer breakdown really arises due to the quasi-particle current, it is likely that a similar mechanism to that underlying the breakdown in single layers applies here. Important differences would include that the relevant energy gap is no longer the Landau gap, since the  $\nu_T = 1$  state is not a single particle but a collective state. The relevant gap will possibly be the thermal activation energy  $\Delta$ , which is about 100 mK in typical samples.

## 4.3 Conclusions

The Josephson-like interlayer tunneling has been studied in bilayer systems with Hall bar geometry. Three samples, which share the same horizontal structure but only differ in their barrier thickness, have been investigated. The barrier thicknesses are 12 nm, 10 nm and 8 nm. Two tunneling contact configurations were used to study the interlayer tunneling. In the first configuration, the tunneling current is driven to flow across the sample plane. The first two samples show interlayer tunneling characteristics that are similar to published literature and qualitatively consistent to the quadratic dependence of the critical current  $I_c$  on the symmetric-antisymmetric energy gap  $\Delta_{SAS}$ . The critical current of the third sample exhibits also a quadratic  $\Delta_{SAS}$  dependence. However, jumps of I-V characteristics beyond reaching the critical current do not occur.

In order to clarify the role of in-plane transport in the tunneling current, interlayer tunneling was compared with in-plane transport in the two samples HB-10 (10 nm barrier) and HB-8 (8 nm barrier). In both samples, the critical in-plane current, which is associated with the breakdown of the  $\nu_T = 1$  QHE, is the same in both layers. Furthermore, the value of this critical in-plane current is similar in both samples. This equal critical in-plane current in both layers can be explained by a picture, which demonstrates that the total amount of quasi-particle current is the same no matter to which layer an external current is applied. The similar size of breakdown current in both samples indicates that both samples may have similar disorder potential such as induced by doping inhomogeneities.

The two samples exhibit large difference when comparing the size of tunneling current in the above mentioned first configuration with the breakdown current. In sample HB-10, the tunneling critical current is an order of magnitude smaller than the breakdown current, whilst in sample HB-8 the tunneling critical current is exactly the same as the breakdown current. This difference originates from the relative size of the maximum tunneling current and the breakdown current in each sample. With the same sample geometry and thus same area, the actual maximal tunneling current is determined by the tunnel coupling  $\Delta_{SAS}$ , which is given by the barrier thickness  $d$ . The actual maximal tunneling current can be approached by choosing the second contact configuration, in which the current contacts are vertically aligned. In such a configuration, the tunneling current is no longer forced to flow in the sample plane. This configuration results in a gigantic critical current in sample HB-8, which exceeds  $1 \mu\text{A}$ . In sample HB-10, the critical currents registered in the two contact configurations do not differ significantly. The actual maximum tunneling current in sample HB-8 is thus considerably larger than the breakdown current, so that in the first configuration the tunneling is limited by the breakdown current and in the second configuration it is not. In sample HB-10, the actual maximum tunneling current is much smaller than the breakdown current, so that in this sample both configurations yield the same tunneling critical current.

The size of the critical tunneling current of sample HB-8 as well as its microscopic details in the second contact configuration are still not clarified. Nevertheless, it is possible that this is caused by a static pseudospin vortex field described by Eastham et al. [55].

Though the quasi-particle current is likely to be the major contributor to the breakdown of the  $\nu_T = 1$  QHE, the microscopic understanding of the mechanism remains indiscernible. There exists a picture, which involves the hopping of merons between coherent puddles at large currents. Measurements of local potentials such as using a single electron transistor (SET) might be able to shed light on this question.

# Chapter 5

## Josephson Currents in Corbino Bilayers

In the previous chapter, measurements in bilayer Hall bar samples with different tunnel coupling strengths  $\Delta_{SAS}$  have been presented. In this chapter, we will focus on the quasi-Corbino ring geometry. To the contrary of Hall bars, which only have one single edge, Corbino rings have two edges: the outer and inner boundaries of the annulus. For a real Corbino ring, each of these two edges form a single source and drain contact. For the purpose of individually contacting both layers, however, one needs more than one contact. The quasi-Corbino ring used in this work, which is depicted in Fig. 5.1, provides two contacts to the inner and three contacts to the outer edge.

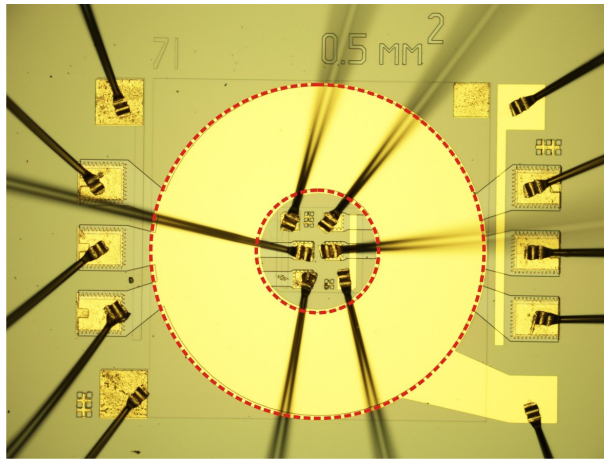


**Fig. 5.1:** Sample structure of quasi-Corbino ring samples used in this work. The radius of the outer and inner edge is 0.43 mm and 0.16 mm, respectively. The active region is the area enclosed by the red dashed circles.

According to the Corbino effect discussed in Sec. 2.1.1, the longitudinal (or radial) conductance in a Corbino disk vanishes at QHE. This also holds for the  $\nu_T = 1$  state, which means that

charged quasi-particles are not able to move from one edge of the Corbino ring to the opposite edge. On the other hand, the charge-neutral electron-hole pairs give rise to an excitonic counterflow in the bulk. Hence, by having two edges, one should be able to separate the excitonic counterflow from the quasi-particle current.

It has been shown, both in theory and experiments, that both the interlayer tunneling conductance and the critical tunneling current scale linearly with the sample area [55] [36] [52] [58]. In this chapter, this issue will be studied for Corbino ring samples, whose outer and inner diameters largely differ. Interedge and interlayer transports will be presented here. Furthermore, our sample geometry enables the application of a second Josephson-like interlayer tunneling current at the inner edge of the sample, simultaneously to the tunneling current at its outer edge. In this way, a possible interplay between these two Josephson currents can be studied.

## 5.1 Interlayer and Interedge Transport

### 5.1.1 Measurement Results

The very first step is to determine the  $\nu_T = 1$  state by magnetotransport. The inset of Fig. 5.2 shows the setup: an AC voltage is applied between the two edges of sample CR-10 from wafer #81653, which has a barrier thickness of 10 nm. While a magnetic field perpendicular to the bilayer plane is swept, the measured current exhibits minima whenever the sample is at a QHE. The  $\nu_T = 1$  state is established at  $B=1.7$  T, yielding a  $d/l_B$  ratio of 1.5 at a sample temperature of  $\sim 12$  mK. In this case, interlayer phase coherence is thus well established.

In Fig. 5.3, two I-V characteristics are shown. In (a), the current is applied from the outer edge to the inner edge of the upper layer while the interedge DC voltage is measured in the same layer. The current is obtained by dividing the voltage drop across a shunt resistor by its resistance of  $1 \text{ M}\Omega$ . The result exhibits a linear regime between  $\pm 2$  mV, giving rise to an interedge resistance of  $1 \text{ M}\Omega$ . Further increasing the interedge voltage leads to dramatic increase of the current between the two edges. Similar behavior can be seen in (b), where the current is not only applied between the two edges, but also between the two layers, with the voltage measured accordingly. Here, a higher resistance of  $2 \text{ M}\Omega$  is obtained from the linear regime.

Fig. 5.4 shows two interlayer tunneling measurements. Here, the two-terminal interlayer voltage is applied and correspondingly the interlayer current as well as the four-terminal interlayer voltage are measured at the outer (a) and inner (b) edge. Both curves have been obtained by combining the up and down sweep directions, in both directions starting from zero. Both configurations result in the typical Josephson-like characteristic as is similar in Hall bar from Sec. 4.1. Interestingly, the critical currents registered from both edges are nearly identical and about  $8.5 \text{ nA}$  in both directions. Furthermore, the interlayer resistance of about  $1 \text{ k}\Omega$  is also sha-

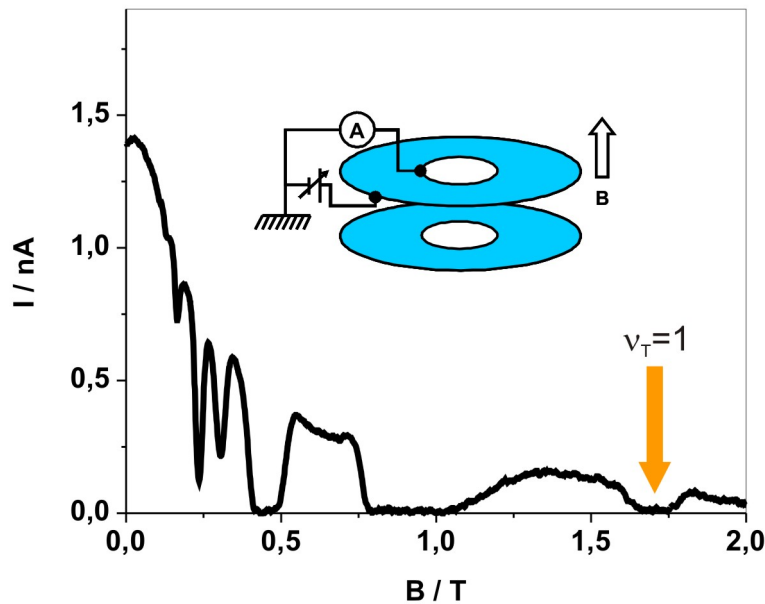


**Fig. 5.2:** Magneto-transport measurement of Corbino ring device CR-10 from wafer #81653. AC current is applied between the outer and inner edge of the annulus as a function of perpendicular magnetic field. At quantum Hall states, the Corbino effect leads to zero interedge conductance seen as minima in the transport trace.  $\nu_T = 1$  state is found at a magnetic field of 1.7 T at balanced layer densities, giving a  $d/l_B$  ratio of 1.5.

red by both edges. While these two features are not surprising on their own, they are intriguing despite a significant length difference of close to a factor of three.

With a sufficient number of ohmic contacts to both layers as well as to both edges of the Corbino ring, our sample geometry provides the additional possibility of measuring the four-terminal interlayer voltage at both edges simultaneously while the interlayer current is applied to one edge. Fig. 5.5 demonstrates such a measurement. Here, the interlayer current is applied at the inner edge and the voltage is measured at both edges simultaneously. In (a), the Josephson regime of the I-V characteristic, which is already presented in Fig. 5.4 b), is shown in more details. The interlayer tunneling is almost linear in this regime with a resistance of 1 k $\Omega$ . Additional structures to the linear background are also visible. The two voltages measured simultaneously are plotted against each other in (b). They are nearly identical in the entire Josephson tunneling regime. This result is surprising, since the bulk system between the two edges is highly insulating. This and other experimental features will be discussed in the next section.

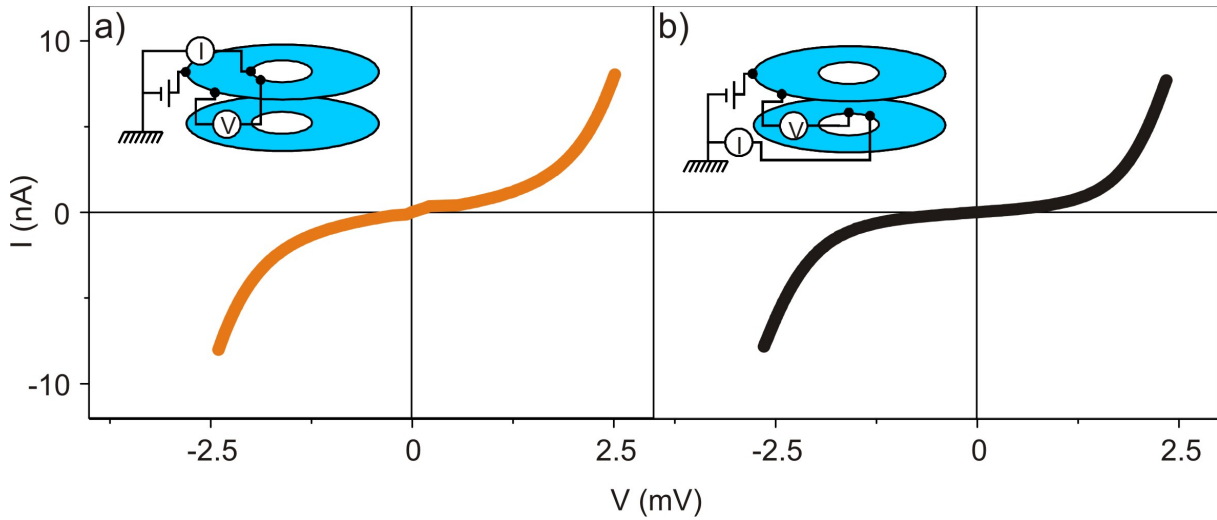


**Fig. 5.3:** Interedge transport in Corbino ring device CR-10. Left panel: Intralayer current is applied between the edges in the upper layer. Right panel: Interlayer current is applied between the edges. In both measurements, the conductance within a voltage of  $\pm 1.5$  mV is small, while it dramatically increases beyond this voltage regime.

The measurements discussed above have partially been carried out in sample CR-8 from wafer #81981 with a barrier thickness of 8 nm. The results, shown in Fig. 5.6, show qualitative similarities to those from sample CR-10. Quantitatively, the interedge measurements shown in (a) and (b) exhibit a higher voltage value marking the onset of the increase of current between the two edges compared to the previous sample.

Moreover, the interedge resistance in sample CR-8 is an order of magnitude larger than in sample CR-10, as indicated by the smaller slope of the I-V curves here. In (c) and (d), one also observes nearly identical critical currents measured at both the outer and inner edge of the sample. The critical current exhibits a slight asymmetry in respect to the direction: the positive critical current is  $\sim 75$  nA while the negative one is  $\sim 50$  nA. Beyond the critical behavior, both I-V characteristics show a smooth transition into the regime where the bilayer is highly ohmic.

### 5.1.2 Data Analysis and Discussion

The results presented in the previous section will be discussed here. First of all, we emphasize that the interedge resistance in Fig. 5.3 a) is consistent with the minimum in current in magneto-transport from Fig. 5.2. This means that the two edges are effectively separated for charge transport. As the voltage between the edges increases to exceed  $\sim 2$  mV, a sizable current starts



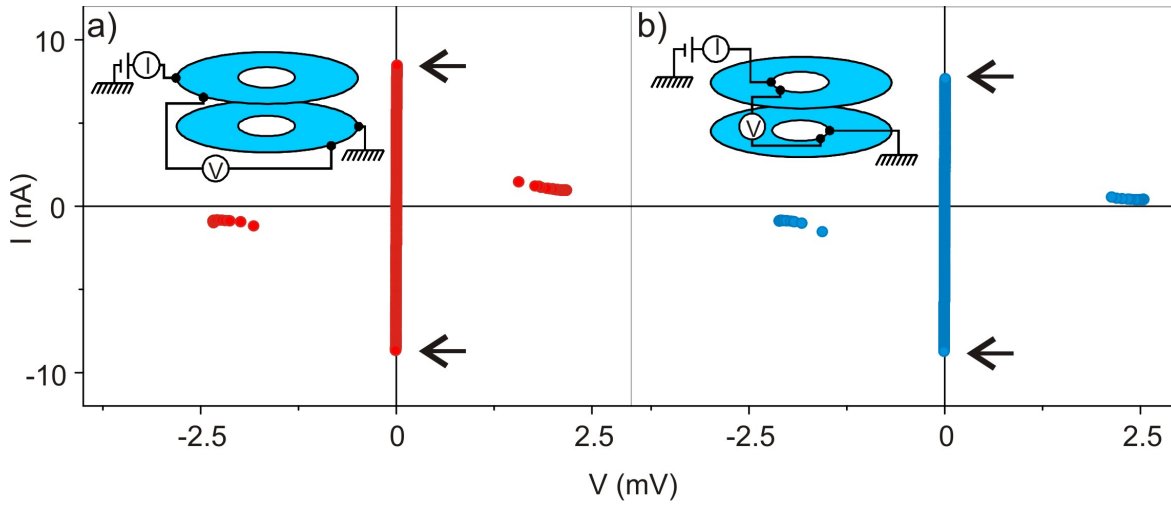


**Fig. 5.4:** Interlayer tunneling in Corbino ring device CR-10. Interlayer current is applied at the outer (left panel) and inner (right panel) edge, respectively. Both curves have been created by combining the up and down sweeps starting from zero interlayer bias voltage. The Josephson-like behavior is observable in both measurements, which show almost the same critical currents. Note that the ratio between the outer and inner diameter is 2.7.

to flow. This marks the onset of the  $\nu_T = 1$  QHE breakdown, which is characterized by the drastic increase of the interedge conductance  $\sigma_{xx}$ .

From Sec. 4.2 it is known that the breakdown of the bilayer QHE is most likely induced by a sufficiently large quasi-particle current. In a Hall bar, the quasi-particle current should flow along the incompressible strips. In case of a Corbino ring, there can be two types of quasi-particle current: a circular current flowing perpendicular to the applied electric field across the ring and a radial current flowing between the edges. At small interedge voltage, the radial current is small and the quasi-particle current is mainly the circular current. As the breakdown sets in, it is possible that the Hall angle will no longer remain at  $90^\circ$  and the circular current gradually evolves into a spiral current. This gives rise to a radial component that increases until the system is completely out of the linear regime.

The Hall resistance at  $\nu = 1$  is  $\sim 25 \text{ k}\Omega$ . Hence, the circular current at a breakdown voltage of  $\sim 1.5 \text{ mV}$  should be the order of  $60 \text{ nA}$ . This is approximately a factor of 4 larger than the breakdown current registered in sample HB-10. Taking into account that the width of the Corbino ring is about 3.5 times as large as that of the Hall bar, this ratio of the critical current seems reasonable and indicates that the critical current has a sample width dependence. Such a dependence has been found in single layer systems [11]. Our result thus provides a further

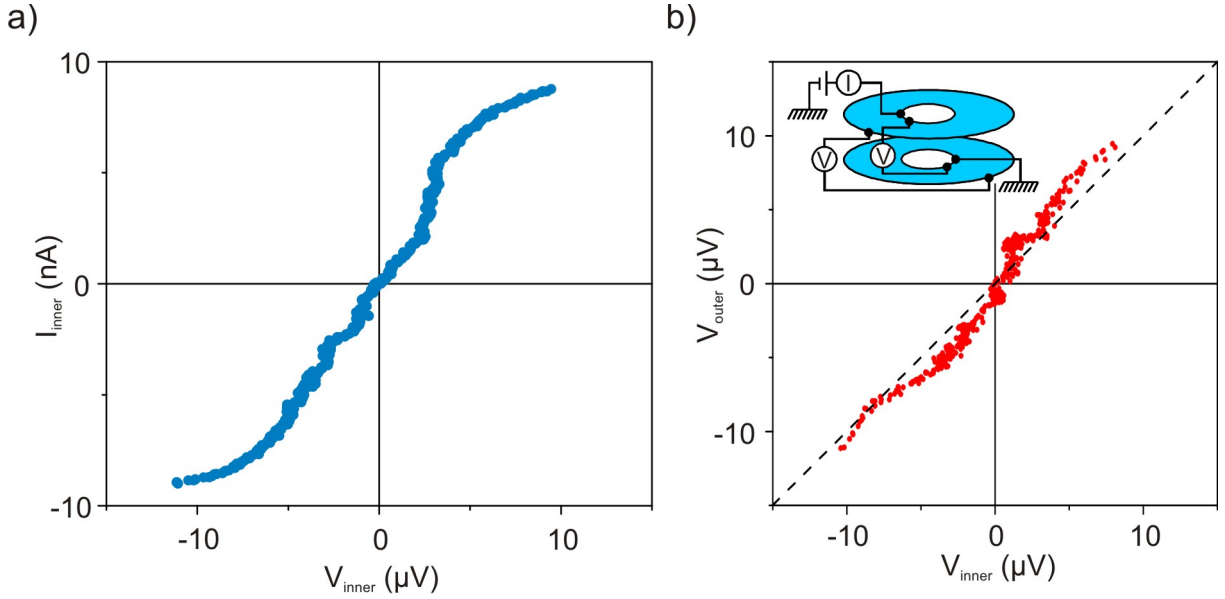


**Fig. 5.5:** (a) Interlayer tunneling at the inner edge of sample CR-10. Time dependent process is believed to lead to the finite interlayer resistance [36]. (b) Voltage measured simultaneously at both edges while tunneling occurs at the inner edge. Both voltages are almost identical, despite the large layer resistances in the plane.

argument besides Sec. 4.2 that the breakdown of  $\nu_T = 1$  QHE might have a similar origin to conventional single layer QHEs.

The interlayer tunneling shown in Fig. 5.3 b) can be viewed as consisting of an interlayer tunneling and interedge transport. Its similarity to (a) shows that in this tunneling configuration the interedge transport is dominant. If the tunneling part is also of coherent nature such as in the case of Josephson-like tunneling, one should be able to apply the same tunneling picture as shown in Fig. 4.10 b) here: the AR-reflected electron-hole pair is spatially separated and needs to travel between the edges to form bilayer exciton. The resistance difference between (a) and (b) is, nevertheless, three orders of magnitude larger than the resistance registered from Fig. 5.4, but similar to the case at zero magnetic field. This strongly indicates that the interlayer tunneling in such a configuration is most likely not coherent.

The Josephson-like tunneling behavior is only realizable when one uses the contacts at the same edge for current injection and removal. The interedge tunneling in Fig. 5.3 b) results in a vanishingly small interlayer current. To the contrary, tunneling at the same edge recovers the enhanced interlayer conductance at  $\nu_T = 1$  state. This seems to mean that tunneling is only possible at the edge of the sample. However, the length of the outer edge is larger than that of the inner edge by a factor of close to three. If tunneling would be an edge phenomena, the

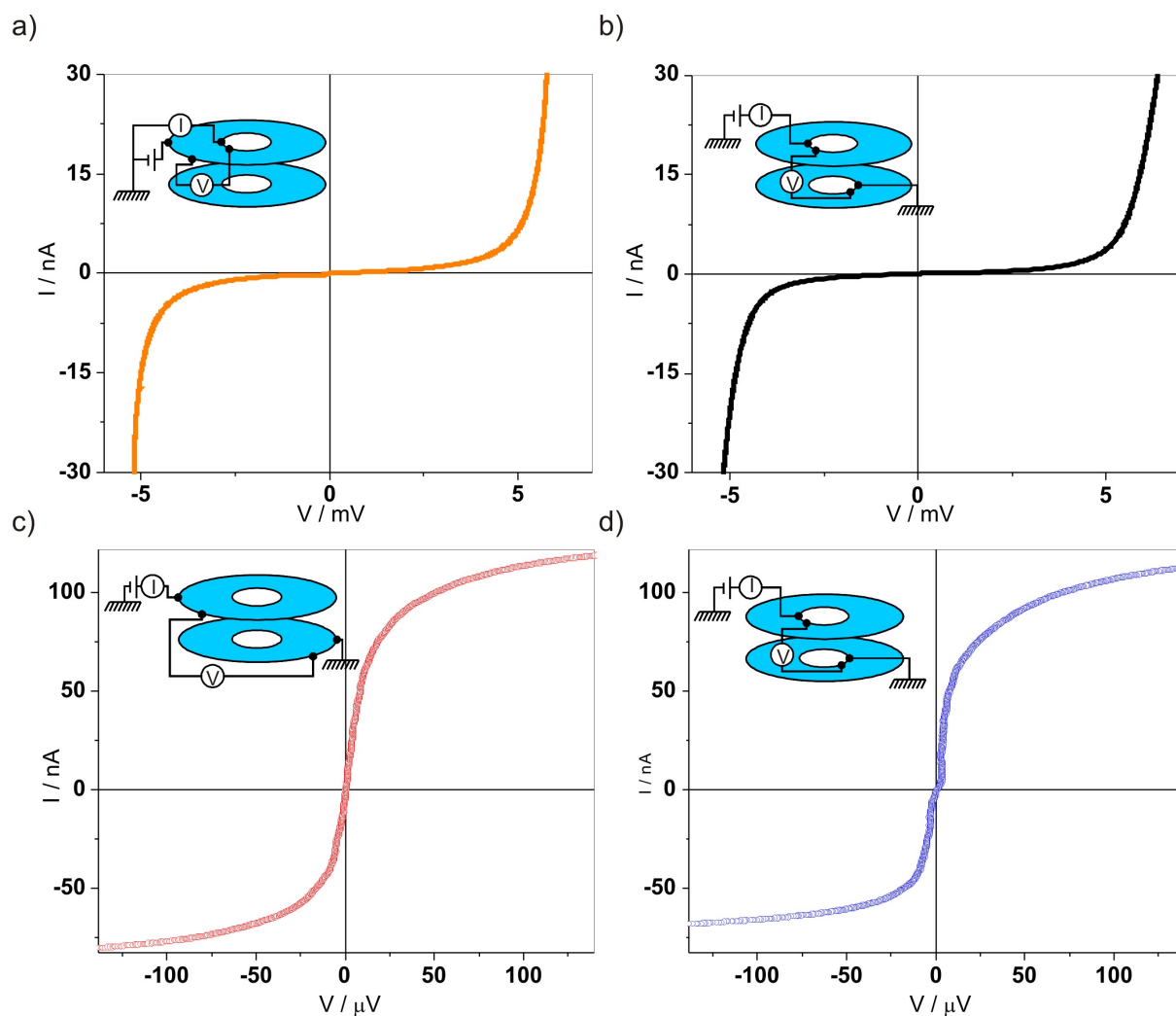


**Fig. 5.6:** Interlayer and Interedge transport in Corbino ring device CR-8 from wafer #81981. Only the up sweep has been included in all measurements. Similar observations to Fig. 5.3 and Fig. 5.4 can be made here, except that the tunneling characteristic in both cases is different.

critical current measured at the outer edge should be about three times the size of the inner critical current. The result that the two critical currents are nearly identical clearly shows that tunneling should not be an edge but indeed a bulk phenomenon.

While this finding is consistent with previously published results [58] [52], the identical critical currents at both the outer and inner edges in a Corbino device tell even more about the Josephson tunneling in the bilayers. After the tunneling current has been injected into the sample, the simple picture of current continuity is that the tunneling current has a decay length in the sample area which is the Josephson length  $\lambda_J$ . Within  $\lambda_J$ , the tunneling current flows as a counterflow current horizontally. In clean systems, this length scale is small and tunneling is nearly confined to the edge. In disordered systems, however,  $\lambda_J$  can be so large that it exceeds the size of the sample. The upper panels of Fig. 5.7 show the current paths for tunneling injection at both edges. In this picture, our result of equal critical currents indicates that tunneling takes place across the entire sample area. The two lower panels illustrate the Andreev reflection process at both edges. At  $\nu_T = 1$  ground state, bilayer excitons are believed to be distributed in the bulk in equilibrium. Injecting tunneling current can thus be seen as injecting AR-generated excess excitons into the excitonic condensate. Such excess excitons differ from the ground state excitons because they can recombine by tunneling. Hence, the maximal injection rate of excess excitons is also limited by the maximal tunneling current. If the tunneling regions for both edges would not overlap, it would be difficult to interpret the equal critical currents. Rather, the two edges share the same bulk and thus the same maximal tunneling current, leading to the same critical currents observed.

The tunneling configuration used in the current Corbino sample involves a transport in the plane, as shown in the inset of Fig. 5.4. In Sec. 4.2, it has been shown that in such case, the tunneling current needs to flow as a quasi-particle current through the sample. This means that in a Corbino ring system, the tunneling current is coupled to a circularly flowing current in the plane. The interlayer resistance of  $1 \text{ k}\Omega$  is thus a combination of this circular transport and an intrinsic tunneling resistance explained in 4.2.

The result that both voltages are equal within the Josephson regime is even more intriguing. The sheet resistance of each layer is of the order of  $1 \text{ M}\Omega$ , while the tunneling resistance at the edges is three orders of magnitude smaller. Hence, one would naively expect that the interlayer voltage measured at the outer edge would be three orders of magnitude smaller than at the inner edge, simply according to Kirchhof's law. Instead, tunneling is happening all over the sample area so that the same current tunnels at the outer as at the inner edge. Since the two resistances measured at these two edges are equal, the interlayer voltages will naturally be equal. This can also be understood with help of the counterflow current  $I^{CF} \propto t\nabla V(\mathbf{r})$ , where the Josephson relation is already taken into account. In the disorder model [36], the excitonic counterflow is present in the whole area and equilibrates the phase all over the sample.

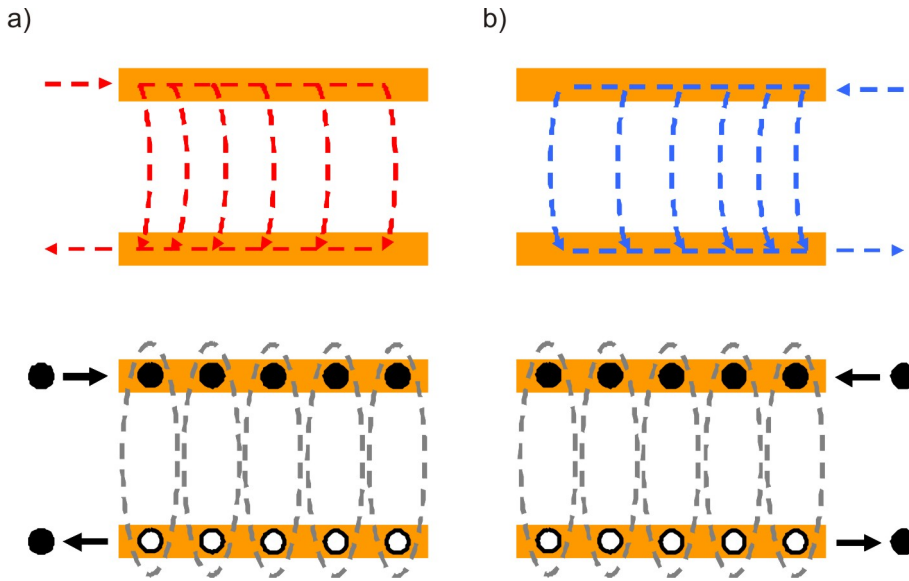


**Fig. 5.7:** Injection of excess excitons as a modified Andreev reflection at one edge of a Corbino bilayer system: an injected electron is bound to a hole from the adjacent layer, which is equal to an electron being removed from this layer. Excitonic counterflow all over the sample plane gives rise to the equal critical currents observed in Fig. 5.4.

Now we turn to discuss the sample CR-8 from wafer #81981 with stronger tunnel coupling (8 nm barrier). The drastic increase of interedge current occurs when the interedge voltage exceeds 4 mV, as is visible in Fig. 5.6 a), which is larger than the 1.6 mV in sample CR-10 from wafer #81653 with intermediate tunnel coupling (10 nm barrier). Interestingly, the critical breakdown currents observed in the Hall bar samples HB-8 (8 nm barrier) and HB-10 (10 nm barrier) are 25 nA and 10 nA, respectively. The ratio between both critical currents is almost exactly the same as between the critical interedge voltages of the two Corbino ring samples. This perfect consistency suggests that the breakdown picture should be equally applicable in the case of interedge transport in Corbino ring samples. Furthermore, the consistently larger critical current/voltage in wafer #81981 points out that smaller interlayer barrier thickness, though not having an effect on the in-plane transport as large as in the Josephson-like tunneling, may lead to a larger energy gap of the  $\nu_T = 1$  state.

The interlayer resistance from the overall resistance in Fig. 5.6 b) is also in the  $M\Omega$  range as in the previous Corbino ring sample, suggesting a similar underlying mechanism here. In Fig. 5.6 c-d), almost equal critical currents may also suggest a similar reason as in sample CR-10. However, taking into account that the actual maximal Josephson-like tunneling current may be orders of magnitude larger than measured in this contact configuration, it is more likely that

the equal critical tunneling currents at both edges are a consequence of the in-plane transport. The interlayer tunneling current can be coupled to a circular current anticipated to exist in Corbino devices at QHE due to the contact configuration. If the same amount of circular current is needed for the breakdown of the  $\nu_T = 1$  QHE, the results in sample CR-8 is natural. The only inconsistency in this regard is that the circular current estimated from the critical interedge voltage of 4 mV is about 160 nA, which is twice as the size of (positive) critical interlayer critical current.

## 5.2 Applying a Second Josephson Tunneling Current

The fact that the excitonic condensate is extended all over the bulk may point at the possibility of interplay between the two edges in a Corbino ring device. In all existing interlayer tunneling measurements in the bilayer  $\nu_T = 1$  quantum Hall state, only one single tunneling current has been applied. By applying a second interlayer current simultaneously might be able to provide evidences of such an interplay, which has to be mediated by bilayer excitons due to the highly insulating properties of the bulk for charged quasi-particles. The setup is shown in Fig. 5.8, where interlayer current is applied at the outer and inner edge while the interlayer voltage is detected only at the outer edge. Using this setup, one is able to register the interlayer tunneling characteristic at the outer edge while applying a constant interlayer current at the inner edge. By varying the second interlayer current, one is able to study how this current influences the interlayer tunneling at the outer edge, despite the insulating property of the bulk for charged quasi-particle currents.

### 5.2.1 Measurement Results

#### Second Tunneling Current $I_{in} < I_c$

Fig. 5.9 shows the result of the above mentioned measurement. Here, the I-V characteristic of interlayer tunneling at the outer edge is shown, while a constant interlayer current between -8 nA and +8 nA is applied at the inner edge. The positive current direction is defined as positive charge flowing from the top to the bottom layer. The I-V characteristics have been artificially shifted along the voltage axis for the sake of clarity. The plotted current is measured on the input side (close to the voltage source) to the upper layer. The voltage is measured at the outer edge using separate contacts.

As no tunneling current is applied at the inner edge, the I-V recovers the one shown in Fig. 5.4 a), i.e. symmetric with respect to the voltage axis. As the inner current is increased in the positive direction, the entire I-V curve at the outer edge shifts downwards by approx. the same amount as the inner current. Such a shifting can be observed up to an inner current of +8 nA,

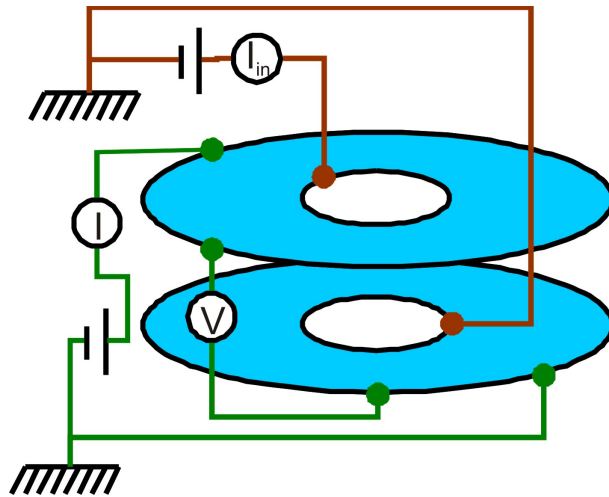


**Fig. 5.8:** Simultaneously applying two interlayer currents at both edges of a Corbino ring bilayer sample. The outer circuit is shown in green while the inner one is shown in brown. While detecting the interlayer current and four-terminal voltage at the outer edge of the sample, a constant second interlayer current  $I_{in}$  can be applied at the inner edge. By varying  $I_{in}$ , this setup enables to study the interplay between both edges in the Josephson regime.

which is below the intrinsic critical Josephson current  $I_c = 8.5$  nA. In the other current direction, the evolution is opposite: with increasing inner current in the negative direction, the entire I-V characteristic at the outer edge shifts upwards by approx. the same amount as the inner current, up to  $I_{in} = -8$  nA. At all the applied inner tunneling currents, the interlayer I-V characteristic measured at the outer edge largely maintains its form. In particular, the current range between the upper and lower bounds of the interlayer current remains almost the same for all  $I_{in}$ , despite a slight change of the slope of the curves within the critical currents.

Fig. 5.10 shows the I-V characteristics measured at the outer edge while the inner tunneling current is varied, this time plotting the output current (close to the ground) from the lower layer. The I-V curves here are also shifted along the voltage axis for the sake of clarity. The result is qualitatively similar to Fig. 5.9, except that the current range between the upper and lower bounds of interlayer current declines in both directions of the inner current with increased  $I_{in}$ . Similar tilting of the I-V curves to Fig. 5.9 can also be observed here.

### At higher $I_{in} > I_c$

The situation in which the size of the inner current  $I_{in}$  is further increased is shown in Fig. 5.11 a). Here, the I-V curves are again shifted along the voltage axis for clarity. With  $I_{in}$  up to 16

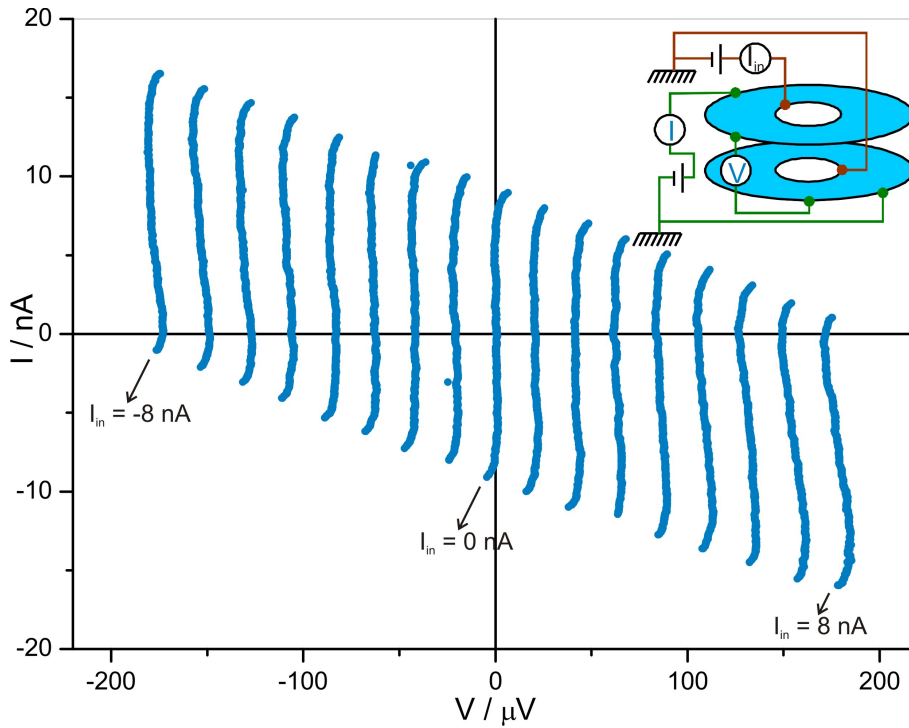


**Fig. 5.9:** Interlayer tunneling I-V characteristics at the outer edge (blue symbols in the inset) of Corbino ring device CR-10 from wafer #81653 (10 nm barrier), while applying a second constant tunneling current  $I_{in}$  at the inner edge (black symbol in the inset).  $I_{in}$  is varied from  $-8$  nA to  $+8$  nA with an increment of  $1$  nA, thus within the intrinsic critical Josephson current  $I_c \simeq 8.5$  nA. The positive current is defined as flowing from the upper to the lower layer. The plotted current refers to the input current to the upper layer. All the I-V characteristics have been artificially offset along the voltage axis for the sake of clarity.

nA in the negative direction, the I-V characteristic at the outer edge maintains its form and the current range between the upper and lower bounds. In order to apply an inner current which is larger than the intrinsic critical current  $I_c$  of the system, it is necessary to first apply a constant interlayer current at the outer edge, before a constant interlayer current at the inner edge can be applied. In this way, the maximal constant inner current can be larger than the intrinsic critical current  $I_c$  by an amount equal to the constant outer current.

At further elevated inner currents, the measurement of outer interlayer tunneling becomes unstable, such that the I-V characteristic at  $I_{in} = 0$  nA is recovered.

In Fig. 5.11 b), the same measurement as shown in Fig. 5.3 b) (black) as well as its modified form (yellow) are plotted. In the modified case, the interlayer tunneling current across the bulk is detected while the interlayer circuit at the outer edge is closed, indicated by a yellow switch



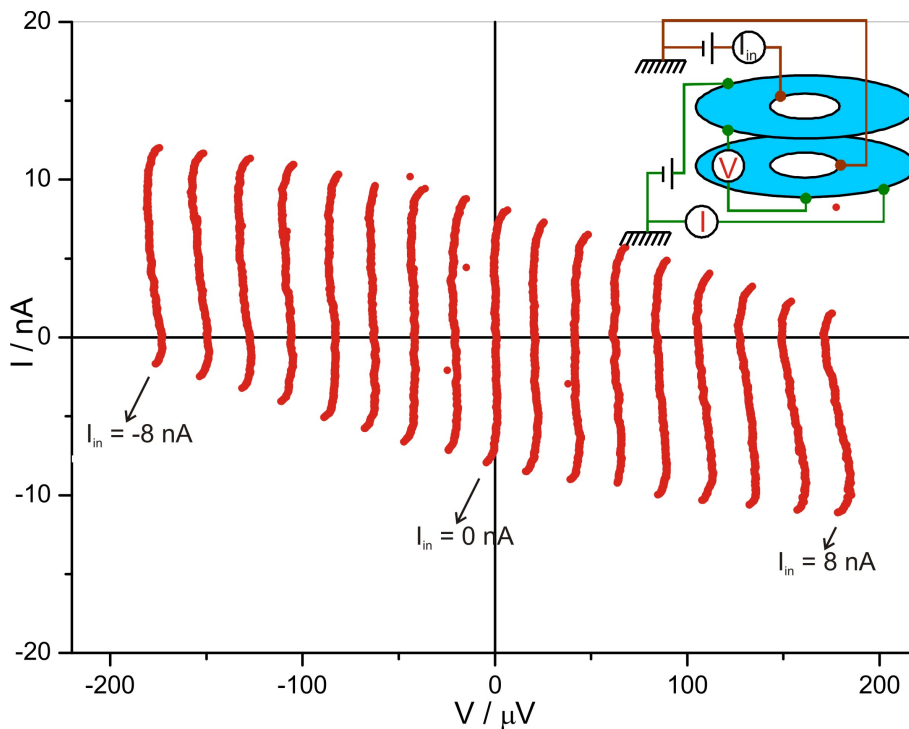


**Fig. 5.10:** Interlayer tunneling I-V characteristics at the outer edge (red symbols in the inset) of Corbino ring device CR-10 from wafer #81653 (10 nm barrier) for  $I_{in}$  at the inner edge (black symbol in the inset).  $I_{in}$  is varied between  $-8$  nA and  $+8$  nA with an increment of  $1$  nA. The plotted current refers to the output current from the lower layer. All the I-V characteristics have been artificially offset along the voltage axis for the sake of clarity.

in the inset. The data shown in yellow is obtained when the interlayer tunneling is measured as shown in (a) at  $I_{in} = 0$  nA. The two I-V characteristics strongly overlap in the measurement range.

### 5.2.2 Data Analysis and Discussion

From Fig. 5.9 one can clearly see a correlation between the I-V characteristics at the outer edge and the applied Josephson current at the inner edge. The fact that the inner current is a Josephson current is justified by its size:  $I_{in} < I_c$ . The vertical shifting of the outer I-V is always almost exactly the same as the size of the inner current. In all measurements with  $I_{in} > 0$ , the current measured at the outer edge already exceeds the negative value of the system's intrinsic critical current, while for  $I_{in} < 0$  the positive value of the intrinsic critical current is surpassed. Remarkably, the Josephson-like characteristic is well preserved for the measurement

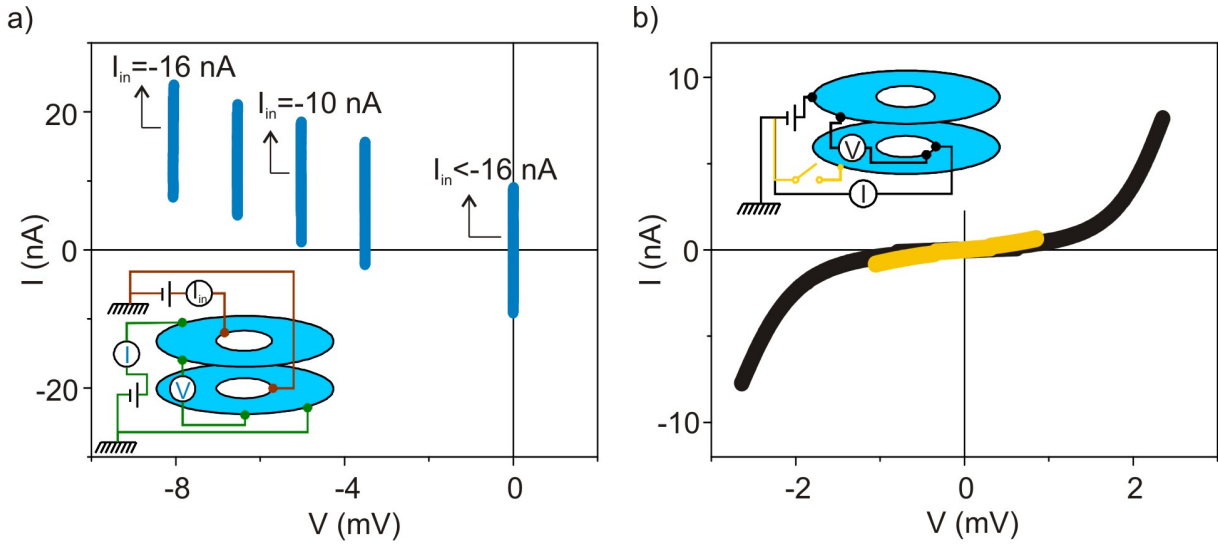


**Fig. 5.11:** Interedge coupling at higher  $I_{in}$ . (a) Interlayer tunneling characteristics at the outer edge at higher  $I_{in}$  exceeding the critical tunneling current of 8.5 nA.  $I_{in}$  is varied between  $-10$  nA and  $-16$  nA. Beyond  $-16$  nA, the interlayer tunneling at the outer edge *jumps* back to the case at  $I_{in} = 0$  nA, indicating that the interedge coupling is lost. (b) Interlayer tunneling between the edges with the circuit switch open (black curve) and closed (yellow curve). In both cases, parasitic potential differences between the edges lead to a charge current flowing between them.

at the outer edge in all traces. In particular, this manifests itself in the difference between upper and lower bounds of the critical currents, which is the same under all applied inner currents  $I_{in}$ . Furthermore, this is also supported by the overall form of the I-V tunneling within the low bias region that remains qualitatively the same in all measurements. This shows clearly that the coherent tunneling continues to take place in the sample in presence of a second Josephson current.

This type of correlation or interplay between the two edges is truly spectacular, provided that the two edges are separated for charge current by a highly insulating bulk. As shown in the previous section, interlayer measurement at either edge results in a low ohmic tunneling device, whilst it is almost impossible to transport charges between the two edges until the breakdown of the  $\nu_T = 1$  state sets in. The current result shows, nonetheless, that an electric current at one edge is able to influence the one at the opposite edge, without going into breakdown.

This phenomenon can be elegantly explained by the picture of excess exciton injection. It is shown in the previous section, that the injected excitons are able to distribute themselves over the entire sample area, leading to equal critical currents measured at both edges. Consequently,

if one injects excess excitons at both edges simultaneously, these excitons should be able to merge together and interact. Such an interaction depends on the relative polarization of the excitons between both edges. In the case of the same sign for both inner and outer currents (i.e. the lower left and upper right branches of Fig. 5.9), the excitons have the same polarities and can only recombine via tunneling. In this case, the intrinsic maximal Josephson current is shared by both edges. Consequently, the size of critical current at the outer edge will be reduced by the same amount of current injected at the inner edge. To the contrary, if the two currents have opposite signs (i.e. the upper left and lower right branches of Fig. 5.9), the excitons from both edges are able to compensate themselves directly, which opens up a second channel for recombination besides tunneling. This leads to an increased critical current at the outer edge.

It is the unique property of polarized excitons that leads to these two different dependencies of the I-V characteristic at the outer edge on  $I_{in}$ . In conventional superconductors, the Cooper-pairs are unpolarized. Therefore, when adding up Cooper-pairs through multiple channels, the critical current of one channel will only be decreased. Bilayer excitons thus possess one more degree of freedom.

We stress again that the two currents applied at both edges are effectively separated electrically. The fact that they still interact with each other can therefore only be attributed to the exchange of excess excitons. Our result thus demonstrates, perhaps for the first time, that two individual electrical currents are coupled by exchanging charge neutral objects.

Not only the input but also the output tunneling current measured at the outer edge shows a correlation to the inner current, as demonstrated in Fig. 5.10. However, the I-V characteristics differ from those at the input side. This deviation is best visible in Fig. 5.12, where the critical currents for both the input and the output interlayer currents at the outer edge are plotted as a function of  $I_{in}$ . For the input critical currents (shown as blue dots), a linear dependence can be found upon the inner current. For the output critical currents (shown as red dots), such a linear dependence is visible when the size of the measured outer edge current is small, as is the case for  $|I_c| < 8$  nA. In these two regions ( $I_{in} > 0$  and  $I_{out} > 0$ , as well as  $I_{in} < 0$  and  $I_{out} < 0$ ), the input and output critical currents almost overlap each other. As the size of the outer edge current further increases, the input critical current is larger than the output one and the deviation between the input and output critical current also increases.

While the deviation of the output current from the input one most likely stems from unavoidable circuit resistances which will be explained in detail further below, this discrepancy might raise the question whether the correlation between the edges involves exciton physics or rather due to some trivial hidden link between the edges. At  $I_{in} = 0$  nA, one observes a deviation of about 1 nA in both current directions when  $I_{out}$  has reached its critical value of 8.5 nA. This means that, when an interlayer current that is smaller than the system's intrinsic critical current is applied at one edge of the Corbino ring, no more than 1 nA out of 8.5 nA is flowing between

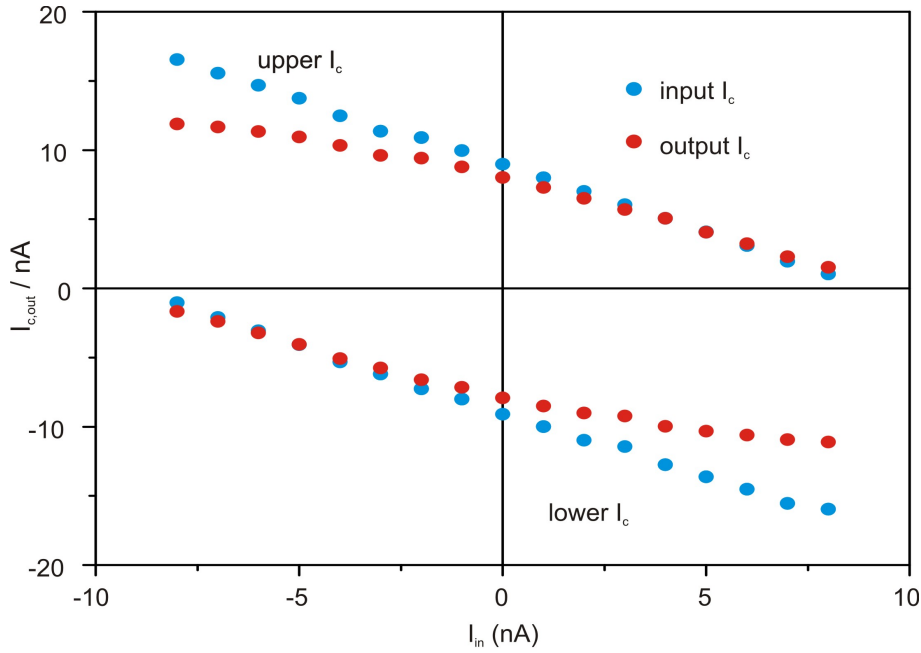


**Fig. 5.12:** Critical interlayer tunneling current  $I_{c,out}$  in Corbino ring device CR-10 from wafer #81653 at the outer edge as a function of the interlayer current  $I_{in}$  simultaneously applied at the inner edge. Both input (blue) and output (red) critical currents are shown here. As the size of outer current is small ( $< 8$  nA), both input and output critical currents overlap. At higher outer currents, the input critical current becomes larger than the output one.

the edges. This interedge current flows because the resistance between both edges is not infinite and a sufficiently large potential difference between them can lead to a measurable charge current. However, this current is carried by charged quasi-particles, not excitons. The critical output current at the outer edge when applying a constant current of 8 nA in either direction is about 12 nA, thus larger by the intrinsic critical current by 4 nA. Clearly, this increase is larger than the interedge charge current of 1 nA. Therefore, it is of solid evidence to state that there is an exchange of currents between two edges which is not to be attributed to interedge charge transport.

Another potential candidate for the coupling would be through the in-plane critical current associated with the breakdown of  $\nu_T = 1$  QHE. The bottle neck in such case would be the

critical breakdown current in the plane instead of the intrinsic critical Josephson current. Nevertheless, taking into account the critical voltage in Fig. 5.3 of 1.6 mV, the breakdown should be expected to happen at a current of the order of 30~50 nA, which is significantly larger than the observed 8.5 nA. Apparently, this possibility to explain the interaction between the two edges can be ruled out.

With the above discussions, we are confident to state that the coupling between two bilayer Josephson currents is indeed enabled by charge neutral interlayer excitons at the  $\nu_T = 1$  state.

Nevertheless, a phase-correlation induced coupling between two Josephson currents as in the case of Superconducting Quantum Interference Devices (SQUIDs) has not been observed in bilayer systems. This may be due to the same reason which destroys the Fraunhofer pattern in tilted magnetic field measurements which yield an envelope function of the anticipated Fraunhofer oscillations [59]: the coherence length of roughly 200 nm in current bilayer systems at  $\nu_T = 1$  state is too small compared to the sample size in the mm range, due to the existence of merons [36]. It is possible that one needs bilayer samples which have the size of the order of the coherence length in order to observe such macroscopic coherence.

An intuitive question can be raised, whether there is a limit for the coupling between two individual bilayer Josephson currents as shown above and if there is, which mechanism is underlying this limit. A possible limit could be posed by the critical velocity of the excitons or equivalently the critical counterflow current between the two edges: such a critical behavior would govern the current exchange since the latter is found to be mediated by the excitons. Theoretical model by Hyart et al. predicts a pseudospin wave velocity in typical bilayer systems such as the current sample to be  $u \sim 14$  km/s. This would correspond to a critical Josephson current of  $\sim 1$  mA if one takes the charge density in the layers as the density of the excitons and their flux as the one of the compensating electric current. Interlayer measurements under elevated  $I_{in}$  shown in Fig. 5.11 a) demonstrate a possible way to identify such a critical counterflow current. This results in a maximal critical inner edge current  $I_{inner,m} = -16$  nA for the negative current direction. This value corresponds to a critical exciton velocity of  $\sim 20$  cm/s, hence significantly smaller than the anticipated value. The disappearance of the exciton-mediated coupling under further increased  $I_{in}$  can therefore hardly be explained by an intrinsic critical velocity of excitons in the condensate. It is more likely that an interedge current resulting from parasitic voltage between the edges is responsible for this observation.

This becomes clearer when taking the result demonstrated by Fig. 5.11 b) into account. When closing the switch, the two terminal interlayer bias voltage at the outer edge is identical to the interlayer voltage between the two edges. Hence, increasing the two terminal voltage at the outer edge will also affect the transport between the edges. The reasonable comparability between both curves indicates that almost the same amount of current flows between the edges, no matter the switch is closed or open. Both measurements show a resistance of  $2$  M $\Omega$ ,

which is the resistance for charge flow between the edges in combination with incoherent tunneling. Such a charge current is given by a parasitic voltage building up between the edges. When the interlayer current at the outer edge is within the system's intrinsic critical current, the charge current is small as shown by the yellow curve. When the outer current becomes larger in presence of an inner current, the two terminal voltage between the edges will also become sufficiently large to enable a large charge current that eventually is as large as the total input current. In such case, the exciton-mediated coupling breaks down and the I-V characteristic at  $I_{in} = 0$  nA is recovered.

Our result thus shows a critical behavior of the counterflow current at  $I_{in} \geq 16$  nA. Nonetheless, it is still not clear, why the parasitic effects will show up at all, since recombination of excess excitons theoretically should be energetically much more favorable since it involves no or little dissipation due to charge neutrality, compared to dissipative processes of charge flow.

Finally, a few remarks will be made to the I-V characteristics seen in Fig. 5.9 and Fig. 5.10. One issue is concerning the vertical shifting of the I-V characteristics. Strictly speaking, the application of  $I_{in}$  does not lead to a vertical shifting of the intrinsic I-V curve without inner current. The reason is that when the two-terminal voltage at the outer edge is zero, there is no current flowing at the outer edge despite the inner current. This is shown in Fig. 5.13, where the current at the outer edge at zero two-terminal interlayer voltage at this edge is plotted as a function of the inner current. If the I-V curves would be indeed shifted vertically as a function of  $I_{in}$ , the data point at  $V_{outer,2pt} = 0$  should also be shifted as the critical currents shown in Fig. 5.12. Since this is not the case, it is most likely that the I-V curves are *cut off* at one end and *extended* at the other end, due to the injected excess excitons from the inner edge.

Hence, the exchange of excitons does not lead to a simple shifting of the Josephson trace. Rather than that, it leads to the change of the critical currents, both the upper and the lower bound. This occurs in form of a counterflow current carried by excitons, which can be estimated by the change of the critical current on the output side at the outer edge<sup>1</sup>. In Fig. 5.14, the data points are obtained by subtracting the output critical currents at  $I_{in} = 0$  from the critical currents measured from Fig. 5.10. Taking into account that the charge current resulting from the inner current is small (less than 1 nA), Fig. 5.14 gives a well estimated amount of counterflow current flowing between the edges. For a fixed  $I_{in}$ , the value of counterflow current exchanged between the two edges also varies, depending on the size of charge current exchanged between the edges<sup>1</sup>. The latter current is associated with the two-terminal interlayer voltage between the two edges, which in our current configuration is equal to the two-terminal interlayer voltage at

<sup>1</sup>The critical current on the input side at the outer edge is not a good reference here. The reason is that this current will include a considerable charge current exchanged between the two edges, when the outer current becomes sufficiently large.

<sup>1</sup>More precisely, it depends on the charge current between the upper layer at the outer edge and the lower layer at the inner edge.

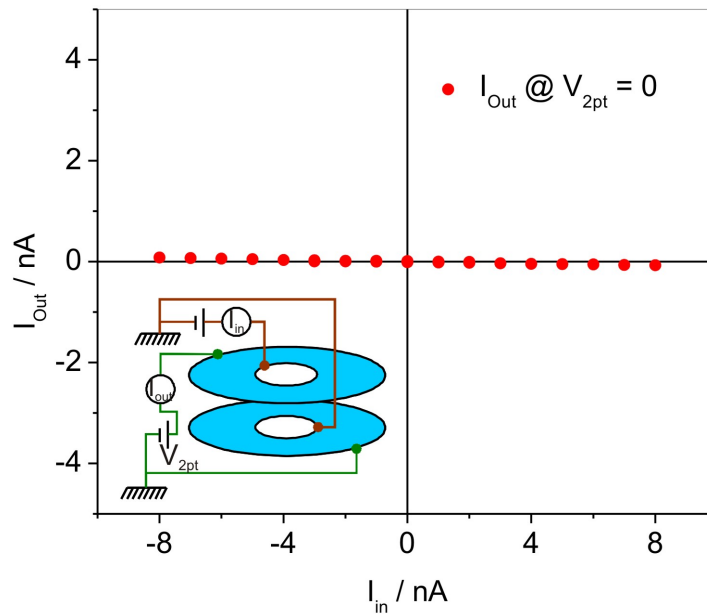


**Fig. 5.13:** Interlayer current  $I_{out}$  measured at the outer edge while the two-terminal voltage  $V_{2pt}$  at this edge is zero, as a function of the inner current  $I_{in}$ . All data points lie almost on the zero current axis.

the outer edge. Hence, the exchange of exciton current is correlated with the size of interlayer current at the outer edge. The actual counterflow current, or, the exciton-mediated change of interlayer current, of the system can thus be any value within the area enclosed by the blue and red points in Fig. 5.14.

As already pointed out earlier, the I-V curves in Fig. 5.9 and Fig. 5.10 exhibit a twisting effect when an inner current is applied. This twisting increases as  $I_{in}$  increases. Furthermore, this twisting is anti-clockwise, no matter if a positive or a negative  $I_{in}$  is applied. A quantity that also increases monotonically with  $I_{in}$  is the difference of the interlayer voltage between the two edges, as shown in Fig. 5.15. Here,  $\Delta V$  denotes the difference between the interlayer voltage at the outer edge and that at the inner edge, i.e.  $\Delta V = V_{outer} - V_{inner}$ . As the size  $I_{in}$  increases, the maximal value of  $\Delta V$  increases, indicating that the gradient of the interlayer voltage across the bulk increases. This corresponds to an increasingly inhomogeneous distribution of the electrical potential in the upper layer, since the lower layer is grounded at both the outer and the inner edge. Such an inhomogeneity might be able to change the distribution of coherent and incoherent puddles in the bilayer system, thereby decreasing the coherent area, so that the coherent tunneling current decreases. The current range between the upper and lower bounds in Fig. 5.9 decreases slightly at high  $I_{in}$ , which supports this picture. Though the details about the

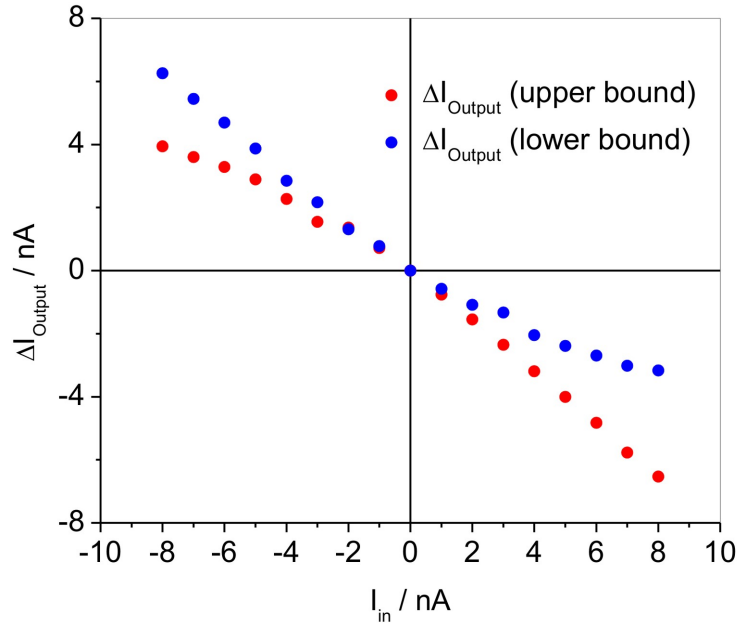


**Fig. 5.14:** Change of critical current  $\Delta I$  on the output side at the outer edge as a function of the inner current  $I_{in}$ . Data points obtained by subtracting the intrinsic critical current (measured at  $I_{in} = 0$  nA) from the upper/lower (blue/red) critical current from Fig. 5.10. For each  $I_{in}$ , the size of exciton counterflow current exchanged between the two edges is estimated to be in the range between values marked by the blue and red dots.

puddle distribution is not known, this mechanism might lead to some kind of instability in the outer circuit and give rise to the observed negative differential resistance.

### 5.3 Conclusions

In this chapter, bilayer systems with Corbino ring geometry have been studied to reveal a number of properties regarding the interlayer tunneling as well as the bulk and edge transport.

For the Corbino sample with 10 nm barrier thickness, transport between the two edges leads to a highly ohmic I-V behavior within a critical voltage of 1.6 mV. Similar behavior is also observed in the tunneling between the edges, except that in the latter case the resistance is higher, indicating the tunneling being an incoherent process. Both measurements show that the two edges are effectively separated by a highly insulating bulk. The Josephson-like interlayer tunneling is, however, fully recovered when tunneling is measured at either the outer or the inner edge of the sample. Moreover, both edges exhibit exactly the same critical currents as well as



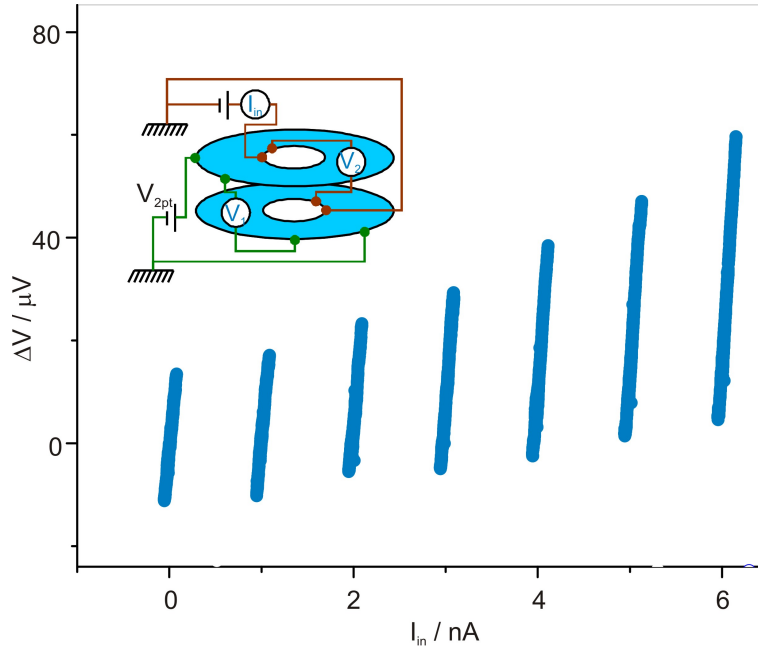


**Fig. 5.15:** The difference of interlayer voltage between the outer and inner edge,  $\Delta V = V_1 - V_2$ . Each curve is obtained from sweeping the two-terminal voltage  $V_{2pt}$  at the outer edge through the Josephson regime for this edge. This measurement has been done under several inner current  $I_{in}$  between 0 nA and 6 nA.

tunneling resistance, despite a length difference of close to factor three. This clearly shows that the Josephson effect in bilayers is not an edge but a bulk phenomenon, consistent with previously reported results [58] [52]. In addition, the equal critical currents also show that the interlayer current tunnels over the entire sample area. This is consistent with the observation that the interlayer voltage measured at both edges are the same while interlayer current is applied to one edge. In the picture of excess excitons, i.e. excitons injected via an Andreev reflection like process, the equal critical currents at both edges can be explained by the two edges sharing the same bulk and thus the maximal Josephson tunneling current, through which the injected excitons recombine. The bulk is prohibited for charge flow, but perfectly open for excitonic flow. Tunneling can thus take place all over the sample area and equalize the interlayer phase. This results in the same interlayer voltage measured at both edges under application of interlayer current at one edge.

The excitons can be injected into the bulk system through both edges simultaneously. Though they are charge neutral, excitons from both edges are able to interact, leading to increase or decrease of the critical current measured at one edge, while a second interlayer current is applied to the opposite edge. When the two currents have the same sign, the injected excess excitons

have the same polarity and can not compensate themselves. Tunneling remains the only possibility of exciton recombination. In this case, the maximal Josephson current is shared by both edges, thus the critical current at one edge is decreased when increasing the interlayer current at the other edge. When the two currents have opposite signs, the injected excess excitons have opposite polarizations and are able to compensate themselves, thereby opening a second channel for exciton recombination. This leads to increased critical tunneling current at one edge when increasing the second current. The two Josephson currents are thus correlated, though the bulk between the two edges are highly insulating.

This result cannot be explained by a trivial electrical effect of parasitic charge current, since an increase of critical current at one edge can be observed that is significantly larger than the maximal charge current between the edges. It cannot be explained by any effect involving in-plane charge transport associated with the breakdown of  $\nu_T = 1$  QHE either, since such a breakdown current would be significantly larger than the observed intrinsic critical Josephson current. Therefore, the exchange of bilayer excitons is the only possible explanation for the observation of coupled Josephson currents at the two edges. Our result thus shows for the first time, that two electrical currents, while being fully separated, can be coupled by charge neutral objects at the  $\nu_T = 1$  bilayer quantum Hall state.

The input and output interlayer currents at one edge deviate when the interlayer current at the other edge becomes sufficiently large. This can be explained by parasitic voltages building up between the edges due to the large but finite resistance between the two edges in respect of charge flow. Measurements at elevated compensating current show that the exciton-mediated coupling between the edges breaks down at a compensating current exceeding 16 nA, marking the onset of critical behavior of the excitonic counterflow. Such a breakdown is most likely a result of the above mentioned parasitic voltage which enables a charge current between the edges that eventually leaves no space for the excitonic exchange. Why such a parasitic effect, which generally involves dissipation, can occur in cost of the exciton exchange is, however, still an open question.

A second open question is the observation that the I-V characteristic of one edge in presence of a second interlayer current at the opposite edge shows anticlockwise twisting, which increases with the size of the second current. Negative differential resistance (NDR) can be seen. While no microscopic explanation is accessible within the current work, it is possible that the increasing difference between the interlayer voltages at both edges with increasing compensating current might lead to a decrease of the coherent tunneling area, since the electrical potential distribution in the upper layer might become highly inhomogeneous due to its increased gradient. This could result in an effective decrease of the tunneling current by increasing the interlayer voltage, thus the NDR.

# Chapter 6

## Corbino-Counterflow at the $\nu_T = 1$ State

One of the most significant features of the  $\nu_T = 1$  bilayer excitonic condensate is that a pseudospin phase gradient in the sample plane gives rise to a charge-neutral counterflowing current, i.e. bound electron and hole pairs flowing in the same horizontal direction. Theoretically, the counterflow is described by Eq. 3.6 and believed to flow in the bulk of the bilayer condensate. Experimentally, the first demonstrations of oppositely flowing currents have used a Hall bar geometry, which has been described in Sec. 3.3. There, current is applied through one layer and a loop resistor before it is directed to the second layer. Vanishing longitudinal and Hall resistance were then taken as signal of a truly dissipationless excitonic counterflowing current.

However, this argument is strictly speaking elusive, since current carried by quasi-particle excitations would theoretically also be able to lead to vanishing longitudinal resistance. Furthermore, it is possible that a charge current  $I$  flowing in one layer will increase the electrochemical potential of the same edge in *both* layers by  $\Delta\mu = \frac{\hbar}{e^2}I$  in the drag measurement [60]. Applying this argument for the counterflow in a Hall bar, the charge current flowing oppositely in both layers will thus increase the electrochemical potential of *both* edges by the same amount, leading to a zero Hall potential. Hence, it is uncertain whether the above mentioned counterflow experiments have detected the bulk properties of excitonic counterflow or merely charged quasi-particle currents. Due to this uncertainty, one needs an alternative which provides securer access to the bulk condensate. As pointed out earlier, the Corbino ring geometry provides two edges, thus direct access to the bulk of the bilayer system. In particular, the bulk quasi-particle current can be neglected at quantum Hall state since the longitudinal conductance vanishes. This enables the extraction of the excitonic counterflow current.

There are two possibilities for this purpose: series and drag counterflow configurations, as shown in Fig. 6.1. It has been argued that the series counterflow configuration does not reach a steady state counterflow since the current might flow through the shunt resistor in a wrong direction, leading to unequal exciton current flowing in and out from the condensate [61]. However, under tilting of the sample, thus introducing a magnetic field component parallel to

the sample plane, Finck et al. have demonstrated the possibility of detecting the counterflow using such a configuration in absence of interlayer tunneling [62].

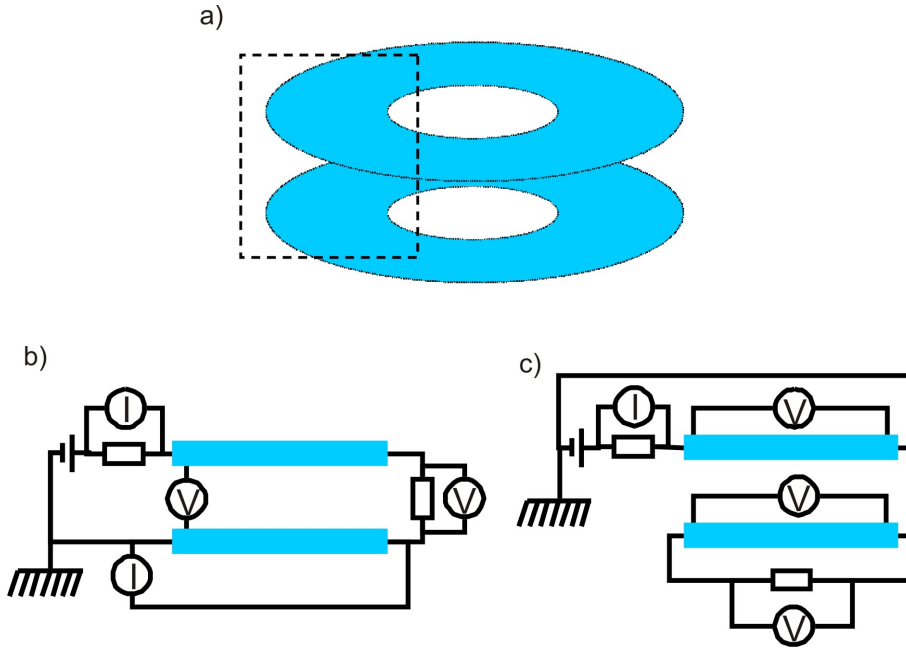


**Fig. 6.1:** Two possible circuit configurations for detection of the counterflow current in a Corbino ring sample (shown in (a), region enclosed by dashed line is shown in (b) and (c)). (b): series counterflow configuration, where current is directed through a shunt resistor connected to one edge of the layers; (c): drag counterflow configuration, where current is directed through a shunt resistor connected across the edges of one layer.

The focus of this chapter lies in measurements in Corbino ring samples performed in both the series and drag counterflow configurations. While the series counterflow has been carried out without tilting the sample in magnetic field, the drag configuration with and without a parallel magnetic field component will be presented.

## 6.1 Series Counterflow

In the series counterflow configuration, the shunt resistor is circuited to connect the upper and lower layers at one edge, while the total current is applied at the opposite edge of the sample. In the following, measurement results in sample CR-10 (10 nm barrier) at  $\nu_T = 1$  will be shown and discussed.

### 6.1.1 Measurement Results

The I-V characteristics measured at the outer edge while the shunt resistor is connected to the inner edge of the sample are summarized in Fig. 6.2, where V refers to the four-terminal interlayer voltage. As the shunt resistance R is reduced from infinity to 1 k $\Omega$ , the Josephson regime of the I-V curve remains the same: both the critical current and the interlayer resistance show no measurable change. To the contrary, the regime beyond the critical currents in both directions changes drastically with the shunt resistance. At high values for R, the interlayer current after reaching the critical currents is strongly suppressed. As R is decreased, a current starts to flow between the layers leading to an increasing slope.

The current flowing through the shunt resistor, denoted as  $I_R$ , is plotted as a function of the total current  $I_{total}$  for the case of R=10 k $\Omega$  in Fig. 6.3. In both current directions,  $I_R$  remains vanishingly small until the total current reaches its critical value. Afterwards, the current flowing through the shunt resistor jumps suddenly to about  $\pm 4$  nA and increases linearly to the total current within the measurement range.

### 6.1.2 Data Analysis and Discussion

There are two features that are special from Fig. 6.2, as the shunt resistance is varied from infinity to 1 k $\Omega$ . First of all, the Josephson interlayer tunneling is clearly visible in all measurements, which is manifested by the zero voltage tunneling associated with almost vanishing resistance and a critical current. Within the Josephson tunneling, the I-V behavior for all shunt resistances is the same. Changing the series shunt resistance thus has no effect on the Josephson effect. Secondly, the I-V behavior beyond reaching the critical currents, i.e. at higher interlayer voltages, changes systematically with the shunt resistance. With infinite or large shunt resistance, as shown in the two upper panels in Fig. 6.2, the slope is small as the interlayer current is strongly suppressed after the critical current is reached. At intermediate shunt resistance, shown in the middle panels, a sizable current begins to flow at higher voltages, which even increases when the shunt resistance is further decreased in the two lower panels.

In order to understand the differences between the Josephson and the high voltage regimes when changing the series shunt resistance, the current flowing through the shunt resistor,  $I_R$ , needs to be analyzed. Fig. 6.3 shows  $I_R$  as a function of the total current applied at the outer edge,  $I_{total}$ , for the case of R=10 k $\Omega$ .  $I_R$  is completely suppressed when the critical Josephson current  $I_c$  is not reached, while it starts to flow after  $I_c$  is exceeded. In Sec. 5.1, it has been pointed out that the interlayer voltage appearing at one edge of a Corbino ring bilayer excitonic system due to application of a 2-terminal interlayer voltage can also be measured on the opposite edge of the sameple. Taking this into account, the current observation is consistent with that from Fig. 6.2. Within the Josephson regime, the interlayer voltage measured at the outer edge is

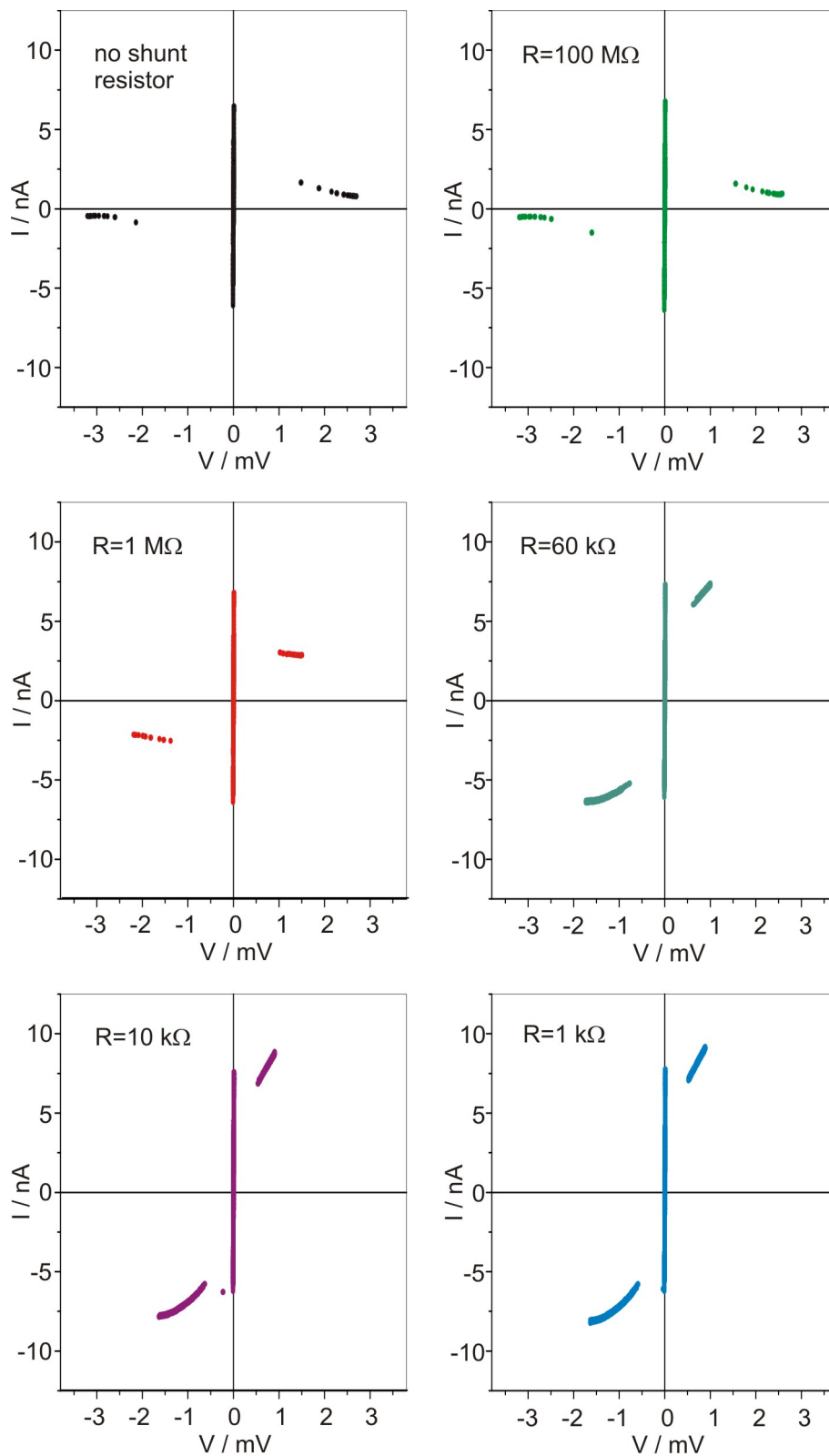


**Fig. 6.2:** Interlayer tunneling at the outer edge of Corbino ring with a shunt resistor connecting the inner edge. The shunt resistance is varied from 1 k $\Omega$  to 100 M $\Omega$ . The case without shunt resistance is also shown (black).

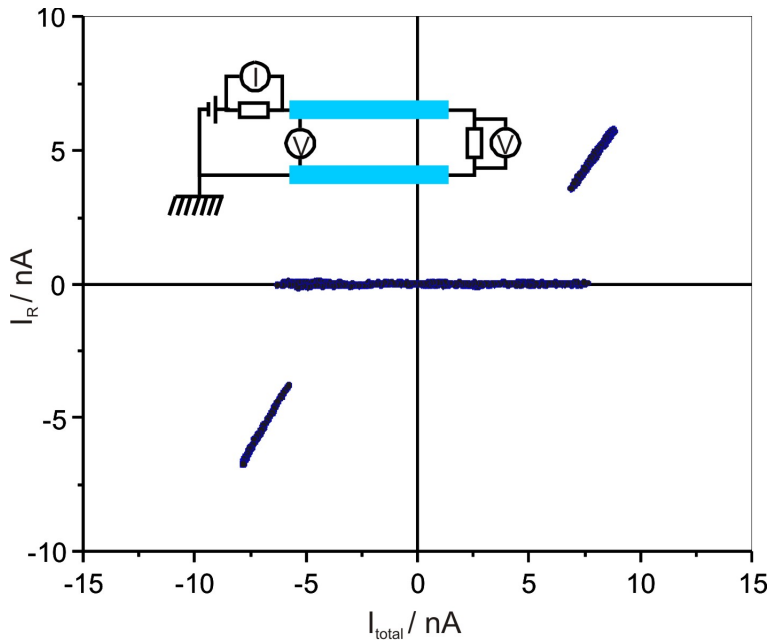


**Fig. 6.3:** The current flowing through the shunt resistor  $R$ , which is connected to the inner edge of the Corbino sample (inset), is plotted as a function of the total current measured at the outer edge for  $R=10\text{ k}\Omega$ . At  $I_{outer} \leq I_c$ , the only a vanishingly small current flows through the loop. Upon the injected current reaching its critical value, the loop current jumps to a finite value and increases monotonically.

vanishingly small. Therefore, the interlayer voltage at the inner edge will also be small, which will lead to vanishingly small current flowing through the shunt resistor. Beyond the Josephson regime, the interlayer voltage suddenly increases, so that a measurable current is able to flow through the shunt resistor. This results in the jump of  $I_R$ .

The finite  $I_R$  is thus responsible for the difference in Fig. 6.2 between different  $R$  values, since the size of  $I_R$  depends on the size of the shunt resistance. This becomes evident in Fig. 6.4, where the difference between the interlayer current at the outer edge and  $I_R$  is shown as a function of the measured interlayer voltage at the outer edge for varied  $R$  values. The resulting I-V characteristics show almost the same behavior in the entire measurement range. Hence, without the influence of  $R$ , the I-V at the outer edge have qualitatively the same behavior, which means that the shunt resistor mainly affects the  $I_R$ .

The occurrence of  $I_R$  needs to be clarified. In particular, it is possible that an excitonic counterflowing current leads to  $I_R$ . In order to proof this possibility, we consider the setup shown in the inset of Fig. 6.5 a), where an additional grounding cable is added to connect the shunt resistor and the grounding point. The shunt resistance is chosen to be  $10\text{ k}\Omega$  here. If

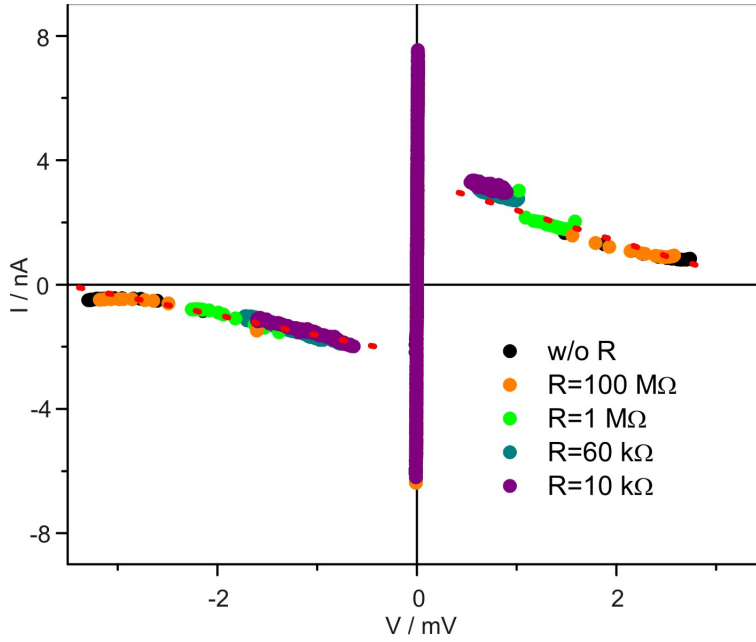


**Fig. 6.4:** Interlayer tunneling characteristics at the outer edge of sample CR-10 while a shunt resistor is circuited to the inner edge. The current results from the total current  $I_{outer}$  minus the current detected at the shunt resistor  $I_R$ . The dash lines indicate the slope of the regime after the critical current has been exceeded, while  $R$  is varied.

the  $I_R$  is indeed associated with the excitonic counterflow, i.e. charge carriers moving in both quantum wells across the loop resistor in opposite directions, it should flow to the grounding point through the lower layer without resulting in a current detectable along the additional grounding line. Otherwise, the current will flow directly through the grounding line, since it has a resistance which is several orders of magnitude smaller than the lower layer.

The left panel in Fig. 6.5 presents two measurements for  $R=10$  k $\Omega$ : the red curve shows  $I_R$ , which flows through the shunt resistor, while the black curve shows  $I_{GND}$ , which is detected along the additional grounding cable. Both currents are plotted as a function of the total current  $I_{total}$ . Before  $I_{total}$  reaches its critical value of 8 nA, both  $I_R$  and  $I_{GND}$  increase monotonically but remain small compared to  $I_{total}$ , while the latter current is slightly larger than the former one. As  $I_{total}$  exceeds the critical Josephson current,  $I_R$  jumps to about 5 nA before it continues to increase. To the contrary,  $I_{GND}$  remains finite and small. This result clearly demonstrates that  $I_R$  does not directly flow to the ground, but through the lower layer. Hence, it is evident that a counterflowing current exists in the bilayer system after the critical Josephson tunneling current has been exceeded.



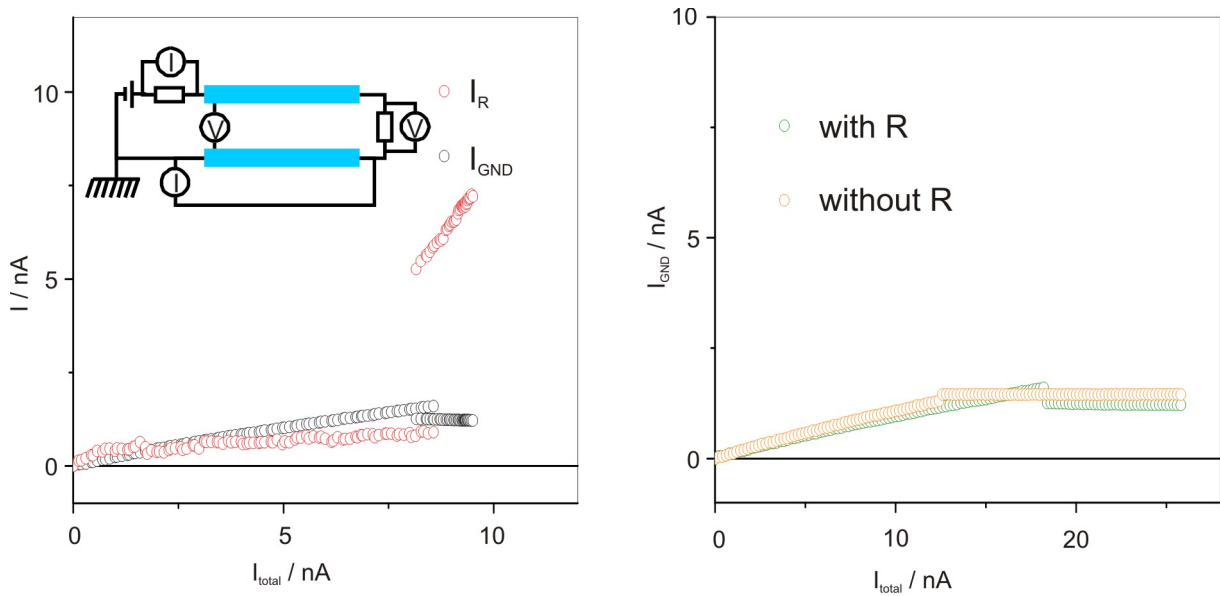


**Fig. 6.5:** Demonstration of  $I_R$  being an excitonic current. Left panel: current flowing through the shunt resistor ( $I_R$ , shown in red) and current flowing from the shunt resistor ( $I_{GND}$ , shown in black) to the ground are plotted as a function of the total current injected at the outer edge, for  $R=10\text{ k}\Omega$ . At  $I_{OUTER} > I_{critical}$ , the loop current is significantly larger than the ground current. Right panel: the ground current  $I_{GND}$  with (orange) and without (green) the shunt resistor.

This phenomenon is intriguing because to the contrary of what is observed in the previous chapter, adding a shunt resistor in the series counterflow configuration does not lead to an increased critical current<sup>1</sup>, but starts to flow beyond the Josephson regime. On one hand, this is somehow self-explaining since in the regime of  $I_{total} \leq I_c$ , the voltage difference between the layers is small on both edges and it can not effectuate a sizable  $I_R$ . On the other hand, this discrepancy should also be rooted in the fact that a shunt resistor does not provide a second source of excess excitons, since such a source would require extra small but finite energy input which is not given here. In the case of a second interlayer current, this energy is provided by the electrical potential difference between the layers at the inner edge, which does not exist in the current case unless the critical current is exceeded. Nonetheless, the fact that under such circumstances the counterflow is still possible and even favored by the current compared to simply flowing through a grounding cable means that one observes a fairly similar effect as Finck et al. [62] in

<sup>1</sup>The lower panels of Fig. 6.2 show a slight increase of critical current compared to the upper panels. Although this is not understood yet, it is most likely not due to any counterflow, since the corresponding  $I_R$  flowing through the shunt resistor is vanishingly small (see Fig. 6.3).

their tilted magnetic field measurement. In fact, suppressing the interlayer tunneling by introducing a parallel magnetic field component seems to not destroy the  $\nu_T = 1$  but effectively only decrease the size of the system's critical current. In this sense, the current measurement may be of exactly the same origin as in the tilted field case: both introducing a parallel magnetic field and exceeding the critical current suppresses the coherent tunneling, while the counterflow can still exist. This is consistent with the prediction of Hyart et al. [36] that the critical current is an intrinsic property of the tunneling but not the  $\nu_T = 1$  state and that exceeding the critical current does not destroy the coherence of the  $\nu_T = 1$  state.

Before the total current has reached its critical value, both  $I_R$  and  $I_{GND}$  exhibit small but finite values. The finite  $I_{GND}$  can be explained by comparing two cases: interlayer tunneling at the outer edge with and without a shunt resistor. The right panel of Fig. 6.5 shows that these two cases yield exactly the same ground current  $I_{GND}$ . In the case without shunt resistor the ground current can only be explained by a parasitic voltage difference between the two contacts where interlayer current is injected and removed, the same as discussed in Sec. 5.2. Hence, the same mechanism must also underly the observed ground current when a shunt resistor is connected to the inner circuit. This result also proofs that  $I_R$  and  $I_{GND}$  are decoupled from each other. Nonetheless, the small but finite size of  $I_R$  in the left panel remains a puzzle. Since  $I_R$  is decoupled from  $I_{GND}$ , the additional grounding cable should pose no influence on  $I_R$ . Further measurements are needed to clarify the details concerning this issue.

## 6.2 Drag Counterflow

In the drag counterflow configuration shown in Fig. 6.1 c), an external current is applied to the upper (drive) layer while a shunt resistor is circuited to the lower (drag) layer of a bilayer system. In the following, measurement results using both samples CR-10 (wafer #81653 with 10 nm barrier) and CR-8 (wafer #81981 with 8 nm barrier) will be shown and discussed. In particular, data of sample CR-8 will be shown in both cases with and without a parallel magnetic field component.

### 6.2.1 Measurement Results

Fig. 6.6 b-d) shows the result obtained with sample CR-8, using the setup shown in (a). The shunt resistance is varied between 1 k $\Omega$  and 3 G $\Omega$ . In (b), the total current measured at the input side of the circuit connected to the drive layer is plotted as a function of the voltage measured across this layer. At high shunt resistance, the I-V characteristic recovers the single layer transport between the edges, shown in Fig. 5.6 a). Between the critical voltages of about  $\pm 4.5$  mV, the slope of the I-V curves is high associated with a large sheet resistance. As the

shunt resistance is decreased to the  $k\Omega$  range, the slope between the critical voltages increases monotonically. This observation is accompanied by an increasing current measured across the drag layer,  $I_{drag}$ , as shown in (c), when the shunt resistance is decreased. Finally, (d) shows the difference between the total current  $I_{total}$  and the drag layer current  $I_{drag}$ :  $\Delta I = I_{total} - I_{drag}$ . The resulting current difference takes a similar form for all shunt resistances. Nevertheless, the critical voltage at which  $\Delta I$  drastically increases shifts downwards as the shunt resistance decreases.

The same measurements are performed also in sample CR-10. As Fig. 6.7 shows, the behavior here is qualitatively very similar to sample CR-8. The slope of the regime within the critical interedge voltages increases with decreasing shunt resistance. Furthermore, the slope of the drag current  $I_{drag}$  as a function of the voltage measured across the drag layer,  $V_{drag}$ , also increases with decreasing shunt resistance. Surprisingly, the difference  $\Delta I$  between  $I_{total}$  and  $I_{drag}$  does not change as a function of  $V_{drive}$  when the shunt resistance is varied, to the contrary of sample CR-8. Instead, all the curves fall together showing the same critical voltages in Fig. 6.7 d).

It has been shown previously, that a parallel magnetic field can lead to suppressed interlayer tunneling currents and that the suppression increases with the tilting angle [35]. Further measurements under strong tilted magnetic fields (up to  $66^\circ$ ) have shown that the Coulomb drag effect, however, remains observable, although the interlayer tunneling is supposed to be completely suppressed at such an angle [63]. In order to study the influence of parallel magnetic field on the drag counterflow, the sample was tilted to an angle of  $75^\circ$ .

Fig. 6.8 a) shows the result of interlayer tunneling at such an angle (red curve), compared to the tunneling I-V without tilting (blue curve). The latter case exhibits a Josephson-like tunneling characteristic that is typical for the wafer #81981 (8 nm barrier thickness), with critical currents in the range of 70 nA. The former case, to the contrary, shows no interlayer tunneling current at all in the entire measurement range. Fig. 6.8 b-c) show measurement of the current flowing through the shunt resistor,  $I_{drag}$  (b) and the difference current  $\Delta I$  (c) between the total current  $I_{total}$  (not shown here) and  $I_{drag}$ , as the shunt resistance is varied between 10  $k\Omega$  and 3  $G\Omega$ . The data for different shunt resistances clearly overlap in the measurement range. Finite values of  $I_{drag}$  can be observed when the shunt resistance becomes sufficiently small and the slope of  $I_{drag}$  as a function of  $V_{drag}$  increases as R decreases. To the contrary,  $\Delta I$  as a function of  $V_{drive}$  takes the same form for all used shunt resistances.

### 6.2.2 Data Analysis and Discussion

In the case without tilting the sample, the behaviors in the drag counterflow of the two samples, CR-8 and CR-10, are qualitatively similar. Both show a change in the total current  $I_{total}$  as a function of the drive voltage  $V_{drive}$ , when the shunt resistance is varied. Here, the slope of

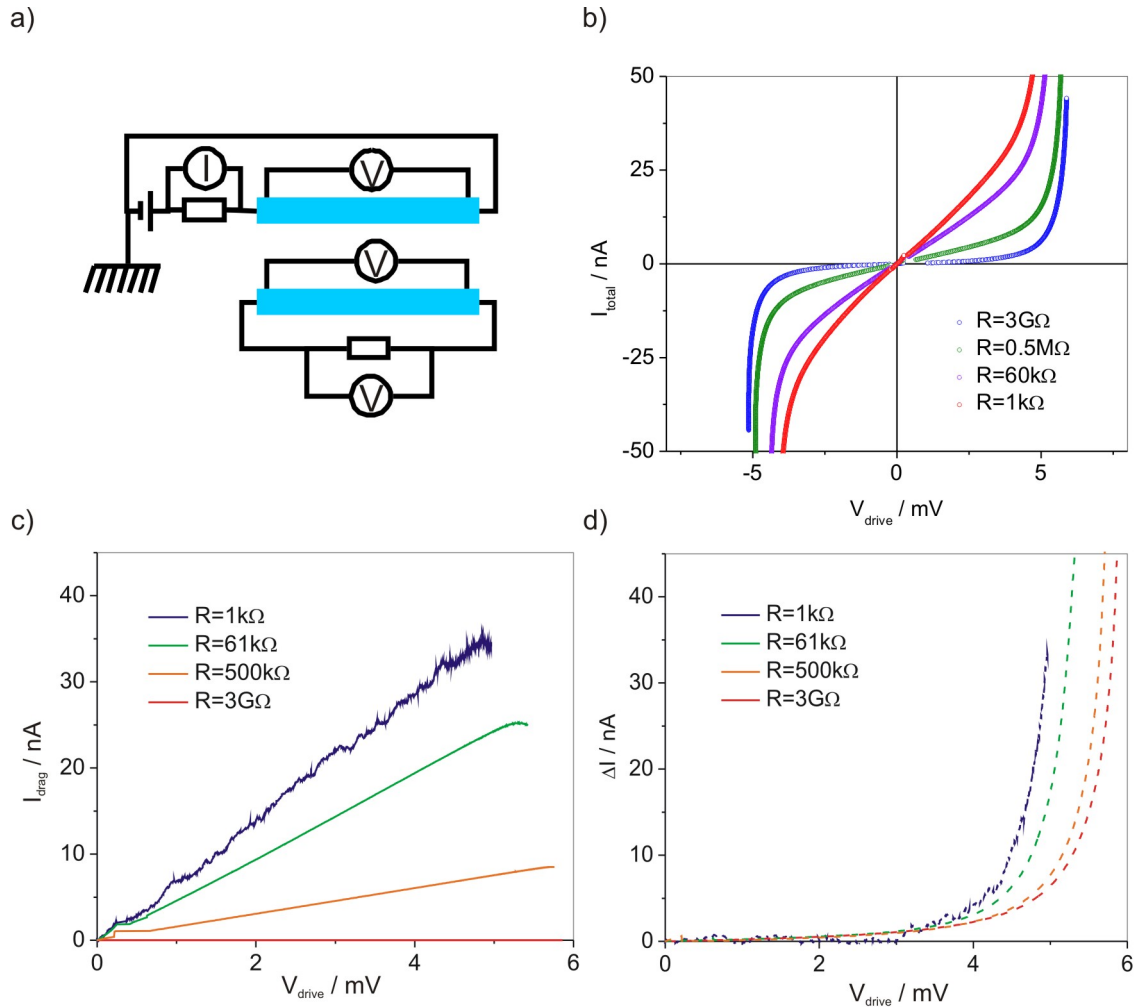


**Fig. 6.6:** Drag counterflow (setup shown in (a)) in sample CR-8. (b) the total current  $I_{total}$  measured at the input side of current as a function of the voltage measured between the edges in the drive layer  $V_{drive}$ . (c) current measured across the shunt resistor connected to the drag layer  $I_{drag}$  as a function of the voltage measured across the drag layer  $V_{drag}$ . (d) The difference between  $I_{total}$  and  $I_{drag}$  as a function of  $V_{drive}$ . All measurements in b-d) are shown for varied shunt resistance.

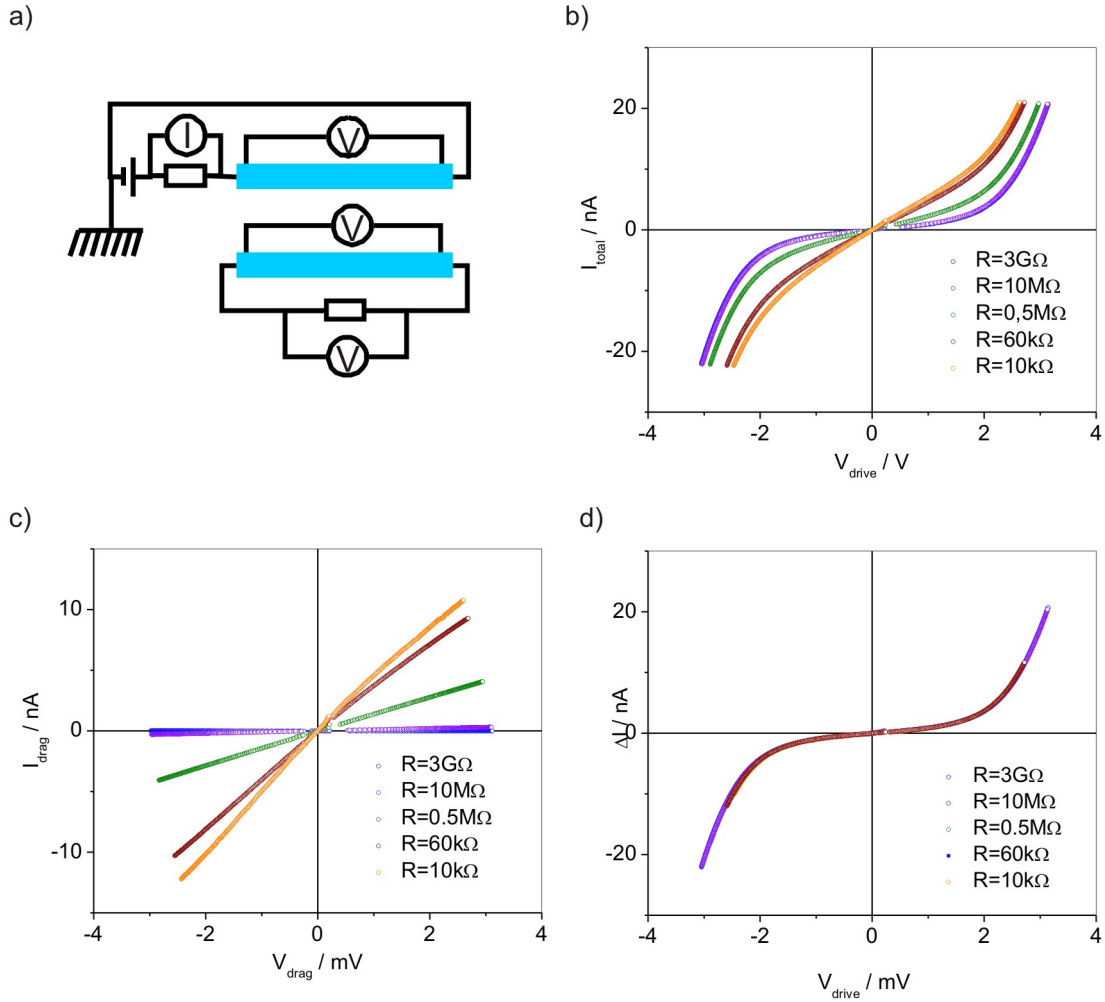


**Fig. 6.7:** Drag counterflow (setup shown in (a)) in sample CR-10. (b) the total current  $I_{total}$  measured at the input side of current as a function of the voltage measured between the edges in the drive layer  $V_{drive}$ . (c) current measured across the shunt resistor connected to the drag layer  $I_{drag}$  as a function of the voltage measured across the drag layer  $V_{drag}$ . (d) The difference between  $I_{total}$  and  $I_{drag}$  as a function of  $V_{drive}$ . All measurements in (b-d) are shown for varied shunt resistance.

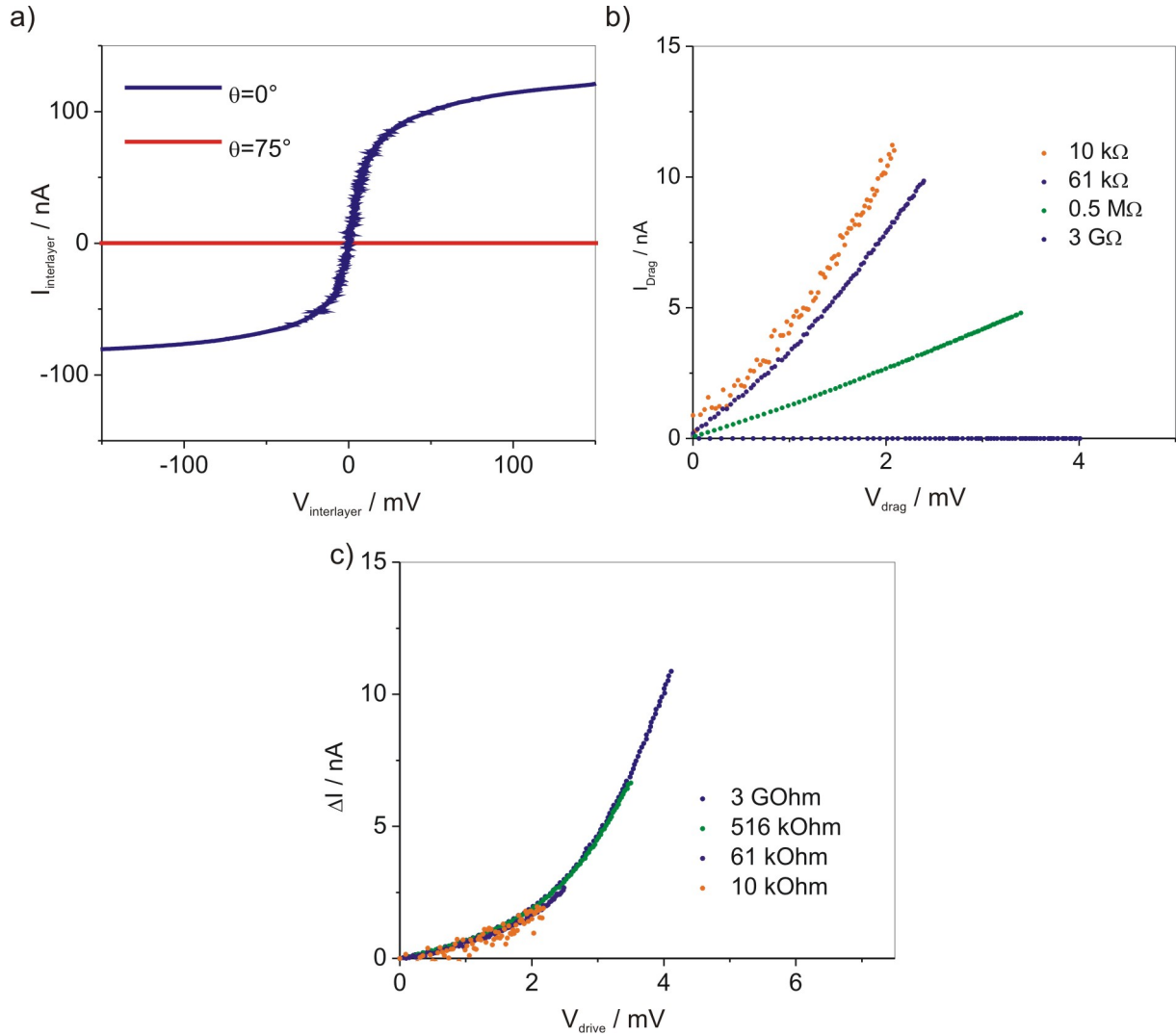


**Fig. 6.8:** Drag counterflow in sample CR-8 under a tilting angle. (a) Interlayer tunneling without tilting (blue) and under a tilting angle of  $75^\circ$ . (b)  $I_{\text{drag}}$  as a function of  $V_{\text{drag}}$  for varied shunt resistances between  $10 \text{ k}\Omega$  and  $3 \text{ G}\Omega$  under the tilt angle. (c) Difference current  $\Delta I$  as a function of  $V_{\text{drive}}$  for varied shunt resistances.

I-V increases with decreasing shunt resistance. The critical behavior at higher  $V_{drive}$  can be understood as associated with the breakdown of the quantum Hall effect at  $\nu_T$ . The drag current  $I_{drag}$  as a function of the drive or drag voltage shows similar slopes for both samples as the shunt resistance is varied. This slope is associated with the total resistance circuited the drag layer except the sheet resistance of the drag layer, if one takes the drag layer as a battery with voltage  $V_{drag}$ . Hence, our result can be interpreted as that the contact resistances are reasonably similar in both samples. Moreover, the slopes concerning the panels (b) and (c) in each sample are also similar. This means that the change in Fig. 6.6 b) as well as Fig. 6.7 b) upon changing the shunt resistance originates from the current measured in Fig. 6.6 c) as well as Fig. 6.7 c), respectively. Hence, varying the shunt resistance to the drag layer changes the drag current  $I_{drag}$ , which indirectly changes the total current  $I_{total}$ .

One can divide the total current  $I_{total}$  into two components,  $I_{drag}$  and the difference current  $\Delta I$ :

$$I_{total} = I_{drag} + \Delta I. \quad (6.1)$$

Without tilting the sample,  $\Delta I$  takes a similar form in sample CR-8 and CR10, except that in the former case the critical voltage shifts to lower values when varying the shunt resistance. Nevertheless, one can state that in all measurements,  $\Delta I$  reflects typical interedge transport in a Corbino ring sample at  $\nu_T = 1$  with a vanishing conductance between the critical voltages. In previous chapters, the increase of current between the edges is attributed to dissipative processes leading to QHE breakdown. In the case of Hall bar samples, it is the quasi-particle current carrying charge that is responsible for the breakdown. It is reasonable to attribute the breakdown in the case of Corbino to the quasi-particle excitations which carry charge from one edge to the other, so that the longitudinal conductance  $\sigma_{xx}$  deviates from zero.

Therefore, it is reasonable to state that the difference current  $\Delta I$  is carried by quasi-particles. The origin of the drag current  $I_{drag}$ , on the other hand, is still not clear at this point. It is possible that it contains the excitonic counterflow which is anticipated also for the drag counterflow configuration, but it might also contain other types of currents. In particular, in the case of strong tunnel coupling such as in sample CR-8, current injected at one edge might tunnel through the barrier. This tunneling current would then be able to leave the same edge and tunnel back through the opposite edge after passing the shunt resistor. Hence, if interlayer tunneling is present in this configuration, the tunneling current can directly contribute to  $I_{drag}$ . Thus, the role of tunneling is crucial in order to clarify the nature of  $I_{drag}$ . A measurement, in which interlayer tunneling is suppressed, will therefore be able to shed some light into this question.

Under a tilt angle of  $75^\circ$ , tunneling is completely suppressed. Nevertheless, the drag current can still be clearly observed which is visible from Fig. 6.8 b). Together with the result without tilting, this shows that a current can flow through the drag layer, independent on the existence of

interlayer tunneling. Taking into account that there is no electrical connection between the two layers in this case, our result provides a direct evidence of the excitonic counterflow: currents flowing oppositely in the layers.  $I_{drag}$  consists at least partially of excitonic current: an electron injected into the drive will be bound to a hole from the drag layer to form an excess exciton. Due to charge conservation, an electron has to leave the drag layer, which contributes to the drag current.

Another feature which can be extracted from the drag counterflow measurements is concerning the role of interlayer tunneling current. Fig. 6.6 d) and Fig. 6.7 d) show fairly similar dependence of the quasi-particle current  $\Delta I$  on the drive voltage  $V_{drive}$ . Nonetheless, in sample CR-10 with weaker tunnel coupling,  $\Delta I$  is a constant function of  $V_{drive}$ , independent on the shunt resistance, whilst in sample CR-8 with stronger tunnel coupling, the critical point of  $\Delta I$  shifts to lower  $V_{drive}$  with decreasing shunt resistance. Most spectacularly, sample CR-8 recovers the same behavior as CR-10 when tunneling is suppressed, visible in Fig. 6.8 c). All these results indicate that interlayer tunneling is influencing the correlation between quasi-particle current and the drive voltage.

This influence can be further visualized by the following diagram: in Fig. 6.9, values of  $V_{drive}$  are plotted versus values of  $I_{drag}$  for sample CR-8 in the case without tilting. The data points have been obtained in the following way: in Fig. 6.6 d), six values of  $\Delta I$  between 5 nA and 30 nA are chosen, which give the corresponding values of  $V_{drive}$  for measurement under each shunt resistance. The values for  $I_{drag}$  associated with the registered  $V_{drive}$  values are extracted from Fig. 6.6 c). For each chosen  $\Delta I$ , all the data points for varied shunt resistances lie on the same line. Intriguingly, all the lines exhibit a slope of close to  $-25 \text{ k}\Omega$ .

The value of the slope reminds one of the quantized Hall resistance at filling factor one. Since the bilayer system is in the  $\nu_T = 1$  state, such a resistance value is likely correlated to the QHE, instead of being incidental. This effect is no longer present, once interlayer tunneling is suppressed or reduced, either by tilting the sample, or by making the barrier thicker. Interlayer tunneling thus plays a central role.

In the following, a model will be provided to explain our results obtained from sample CR-8. The model takes into account three different components which the total current  $I_{total}$  consists of: an excitonic counterflowing current  $I^{EX}$ , a current carried by charged quasi-particles  $I^{QP}$  as well as an interlayer tunneling current  $I^{TU}$ . Fig. 6.10 illustrates these current components as well as their simplified paths within the bilayer Corbino system.

When the total current (blue arrows) is injected from the outer edge of the drive layer, as is the case in the experiments, this total current will be removed from the inner edge to the ground. Within the bilayers, the excitonic counterflow current (brown arrows) can flow from the outer edge to the inner edge in the drive layer, while an opposite current flows in the drag layer that is directed through the shunt resistor. The quasi-particle current (green arrow) flows



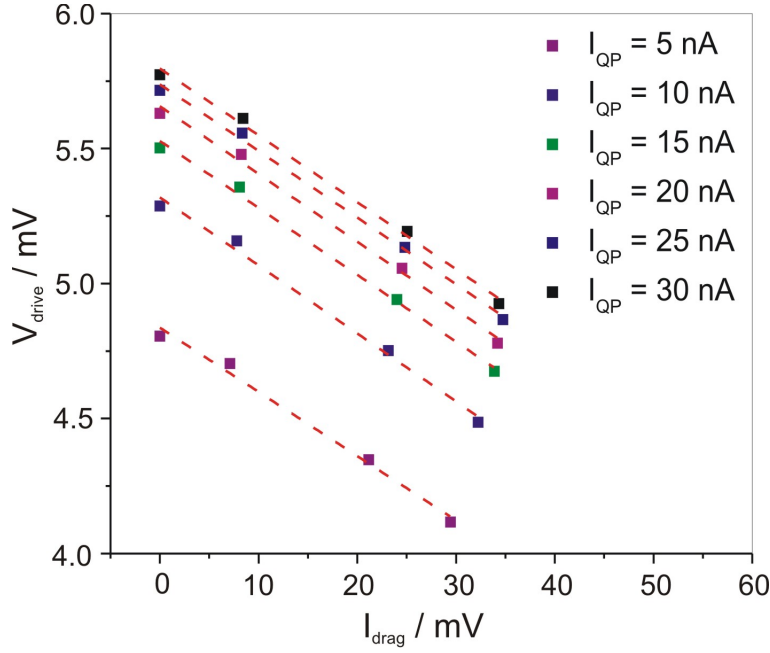


**Fig. 6.9:**  $V_{drive}$  as a function of  $I_{drag}$  for a given  $\Delta I$ . For each value of  $\Delta I$ , the data point is taken for varied shunt resistance. The slope is  $-25 \text{ k}\Omega$  for all traces.

from the outer edge to the inner edge. Finally, the interlayer tunneling current  $I^{TU}$  (red arrows) could flow in the plane, due to the contact configuration in which the source and drain contacts are on opposite ends of the outer edge. This tunneling current will be withdrawn to the ground via a backtunneling process at the inner edge. From the previous chapter, we have learnt that the Josephson effect occurs over all the area where the  $\nu_T = 1$  state is present. Consequently, the tunneling current should be illustrated all over the bulk strictly. Nevertheless, since the bulk is insulating as long as  $\nu_T = 1$  is present, the tunneling current should always flow along the same edge, unless there is a way to circumvent the bulk. This is given when the shunt resistance is sufficiently small, which leads to a second contribution for the measured  $I_{drag}$  besides the excitonic counterflow  $I^{EX}$ . Eq. 6.2 and Eq. 6.3 summarize the two measured currents:

$$I_{total} = I^{EX} + I^{TU} + I^{QP} \quad (6.2)$$

$$I_{drag} = I^{TU} + I^{EX}. \quad (6.3)$$

This leads to the difference  $\Delta I$  between both measured currents:

$$\Delta I = I_{total} - I_{drag} = I^{QP}, \quad (6.4)$$

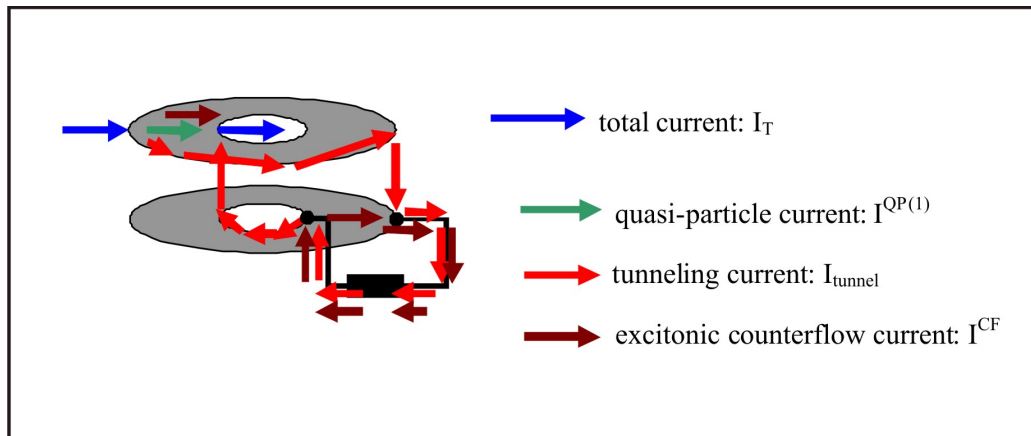


**Fig. 6.10:** Simplified model for the current composition: the total current (blue arrows) applied at the outer edge of the drive layer consists of an excitonic current (brown arrows) flowing oppositely in both layers between the edge, a charge current (green arrow) carried by quasi-particle excitations as well as a tunneling current (red arrows). The tunneling current leaves the drive layer at the outer edge after flowing in the sample plane and flows through the shunt resistor before flowing to the ground via the inner edge.

which states our reasonable assumption that the difference current is carried by the quasi-particle excitations.

There is another current which flows due to the voltage between the edges  $V_{drive}$ . As pointed out in the previous chapter, a circular current flows in a Corbino ring device at QHE, similarly to the longitudinal current in a Hall bar device. This circular current is associated with a voltage drop across the ring, which is the Hall voltage. In the following, this circular current is labeled as the intrinsic circular current  $I_{cir,intrinsic}$  of the system. In addition, the interlayer tunneling current, when it flows in the sample plane, can also give rise to a Hall voltage contribution. This is because when the tunneling current is coupled to an in-plane current, it has to flow as a quasi-particle current along the incompressible strips, as shown in Chap. 4. Due to the contact configuration and the direction of the magnetic field,  $V_{drive}$  only takes Hall voltage originating from the intrinsic part of the circular current. The total voltage between the edges, or the total Hall voltage, will be the sum of both the intrinsic and tunneling current multiplied by the Hall resistance at the total filling factor one. Hence, one has the correlations:

$$V_{drive} = I_{cir,intrinsic} * R_{Hall} \quad (6.5)$$

$$V_{interedge} = V_{drive} + I^{TU} * R_{Hall} \quad (6.6)$$

In the regime far away from the breakdown, i.e. in the low  $V_{interedge}$  regime, the total current  $I_{total}$  consists almost entirely of the drag current  $I_{drag}$ . As  $V_{interedge}$  increases, the circular current can develop a component which flows from one edge to the other. This component is the quasi-particle current  $I^{QP}$ , which increases as the system approaches the QHE breakdown. In the non-ideal breakdown regime characterized by a steep but not perfectly vertical increase of the quasi-particle current,  $I^{QP}$  is monotonic to  $V_{interedge}$ .

Within this model, one can simulate the situation shown in Fig. 6.9 by choosing  $\Delta I = const$ . This means  $I^{QP} = const$ , hence  $V_{interedge}$  has a fix value denoted by  $U$ :

$$V_{drive} = U - I^{TU} * R_{Hall} \quad (6.7)$$

$$\implies I^{TU} = - \left( \frac{1}{R_{Hall}} \right) * V_{drive} + \left( \frac{U}{R_{Hall}} \right) \quad (6.8)$$

The slope seen in each measurement of Fig. 6.9 is effectively the result of differentiating  $I_{drag}$  as a function of  $V_{drive}$  at constant  $\Delta I$ . Using Eq. 6.7, this leads to

$$\left( \frac{\partial I_{drag}}{\partial V_{drive}} \right)_{\Delta I=const} = \left( \frac{\partial (I^{TU} + I^{EX})}{\partial V_{drive}} \right)_{\Delta I=const} = -\frac{1}{R_{Hall}} + \left( \frac{\partial (I^{EX})}{\partial V_{drive}} \right)_{\Delta I=const}. \quad (6.9)$$

The first term of the result in Eq. 6.9 gives the measured value of about 25 k $\Omega$  at  $\nu_T = 1$ . If this model provides the correct picture for our observation in Fig. 6.9, the second term should be zero. This statement means that the excitonic counterflow current is not a function of the interedge voltage caused by the intrinsic circular current. This is consistent with the model of Hyart et al. which suggests that the excitonic counterflow should depend on the difference in interlayer voltage between the two edges, instead of the interlayer voltage or the interedge voltage alone. This model thus clarifies the role of interlayer tunneling in the series counterflow, which does not affect the total voltage between the edges,  $V_{interedge}$ , when tunneling is suppressed by tilting the magnetic field or making the barrier thickness larger. In the frame of this modelling, the similar behaviors in Fig. 6.7 d) and Fig. 6.8 c) can be attributed to the absence of interlayer tunneling current.

Moreover, our measurement also provides for the first time an indirect but quantitative analysis of the anticipated circular current in a Corbino ring device. Such a circular current has never been directly detected so far, whilst in the current analysis taking it into account provides a reasonable explanation of the data.

Two questions still remain open: the slightly smaller slopes in Fig. 6.8 b) as well as the smaller breakdown voltage in Fig. 6.8 c) compared to the case without tilting (Fig. 6.6 c-d)).

The first observation might be explained by the higher contact resistances at a significantly higher total magnetic field of 10.5 T compared to 2.6 T. The second observation might be an indication for a weakening of the  $\nu_T = 1$  state, since its breakdown occurs at a smaller interedge voltage, which corresponds to a smaller critical circular current. It is, nonetheless, not clear what has led to such an attenuation of the excitonic state.

### 6.3 Conclusions

In this chapter, the two circuit configurations for studying the excitonic counterflow, drag counterflow and series counterflow, are presented.

In the series counterflow experiment, in which sample CR-10 is not tilted, one observes the well established bilayer Josephson effect. The Josephson currents do not depend on the shunt resistance circuited to the edge opposite to the one at which interlayer I-V is measured. In particular, the critical current remains the same at all shunt resistances. No current flows through the shunt resistor in this range. When the Josephson critical current is exceeded, the tunneling I-V characteristics exhibit different behaviors depending on the shunt resistance, while the current flowing through the shunt resistor drastically increases. It can be proven that the latter current through the shunt resistor is due to the excitonic counterflow which is expected to exist in the  $\nu_T = 1$  state.

In the drag counterflow, the shunt resistor is circuited to the drag layer, i.e. the layer in which no external current is applied. In both samples CR-8 and CR-10, a drag current flowing through the shunt resistor can be detected, when the shunt resistance is sufficiently small. Furthermore, the difference current, which results from the total current after subtracting the drag current, is most likely carried by quasi-particle excitations. This quasi-particle current increases drastically at a sufficiently large voltage across the drive layer, i.e. the layer in which an external current is applied. Here, there is a difference between both samples: while in the sample CR-10 with weaker tunnel coupling the critical voltage remains the same for all shunt resistances, it shifts to lower voltage in sample CR-8 with stronger tunnel coupling while decreasing the shunt resistance. When the values of drag current and drive voltage at constant values of the quasi-particle current are plotted, the data points one obtains lie on lines with the same slope of  $25 \text{ k}\Omega$ , which is close to the Hall resistance at filling factor one.

Tilting the sample CR-8 under an angle of  $75^\circ$  leads to completely suppressed interlayer tunneling current. Intriguingly, the drag current is still detectable although no tunneling is present, evident of excitonic counterflow. Moreover, the critical voltage of the quasi-particle current do not shift but have the same value for all shunt resistances. This result recovers the same behavior as in the case of sample CR-10 without tilting. Using a model which takes into account the role of interlayer tunneling, one can show that the slope of  $25 \text{ k}\Omega$  is a result of the tunneling giving

---

rise to a Hall voltage contribution, besides the Hall voltage associated with the intrinsic circular current. Our result thus provides the first indirect but quantitative evidence of the circular current anticipated in a Corbino ring device at QHE.



# Chapter 7

## Summary

The revolutionary advances of the information technology in the past decades have greatly changed our daily life. This process was initiated by developments in the physics of condensed matter, which enabled the industry to manufacture ultrafast circuits smaller and more stable. An essential element of this process is the dramatic increase of the purity of crystals, which led to the observation of the two most important effects in semiconducting materials in the past three decades—the integer and the fractional quantum Hall effect (IQHE and FQHE). Both effects were observed in ultrathin interfaces between semiconductors or between semiconducting and metallic layers at high magnetic fields. Such systems are also called two-dimensional electron gas (2DEG). Two Nobel prizes have been awarded for the discovery of these effects: one went to Klaus von Klitzing in 1985 and the other to Daniel Tsui, Horst Störmer and Robert Laughlin in 1998. Nowadays, the two QHEs can be observed in novel systems such as graphene and oxide interfaces as well as complex systems out of them.

Another special QHE has also been observed in the course of this development. If two of the aforementioned 2DEGs are brought to a spacing of few nanometers, while their densities and the magnetic field are set in such a way that the lowest Landau level in each layer is half filled, one can observe a QHE with filling factor of one. Intriguingly, one deals here with a correlated state between the layers, since each individual layer exhibits no QHE at the filling factor of  $\frac{1}{2}$ . For this reason, this effect is called the total filling factor one, or  $\nu_T = 1$  QHE.

Theoretically, the ground state of  $\nu_T = 1$  can be described as Bose condensate of inter-layer excitons, or as spontaneous magnetization of pseudospins. In the first picture, electrons (occupied states of the lowest Landau level) in one layer are bound to holes (vacancies of the lowest Landau level) of the adjacent layer and form excitons. Such excitons can condense at sufficiently low temperatures. In the second picture, the electrons have an extra degree of freedom – pseudospin – which describes in which layer they reside. In the ground state of  $\nu_T = 1$ , all the pseudospins are aligned so that a ferromagnetic order can be established.

The most spectacular feature of this effect is that it leads to a strongly enhanced interlayer

tunneling between the layers compared to the case without magnetic field. This effect prevails until a critical current is reached, beyond which the interlayer tunneling will be strongly suppressed. Due to its strong similarity to the Josephson effect in conventional superconductors, the interlayer tunneling at  $\nu_T = 1$  is called a Josephson-like tunneling effect.

The Josephson-like interlayer tunneling in bilayers at  $\nu_T = 1$  QHE has been extensively investigated, primarily in samples with 10 nm and 12 nm barrier thickness. Such systems show a symmetric-antisymmetric energy gap,  $\Delta_{SAS}$ , of up to  $100 \mu\text{K}$ <sup>1</sup>. The quantity  $\Delta_{SAS}$  is a measure of the coupling between the layers and thus the strength of interlayer tunneling. In this work, we extended the bilayer samples to include a barrier thickness of 8 nm, which has a  $\Delta_{SAS}$  of about 1 mK. In this sample, the interlayer tunneling in a configuration, in which the tunneling current also flows in the plane, has the same critical current as in pure in-plane transport. This is not the case in a sample with 10 nm barrier, where both critical currents strongly differ. In particular, the critical current in the plane which is associated with the breakdown of quantum Hall effect is of similar size to that in the 8 nm sample. Using a contact configuration, in which the current contacts for tunneling are vertically aligned, we observe a much larger critical current in the 8 nm sample. It is larger than the one observed in the 10 nm sample by several orders of magnitude. From these measurements, we conclude that the critical tunneling current of the 8 nm sample in the first configuration is caused by the breakdown of the  $\nu_T = 1$  QHE. This breakdown is solely driven by the quasi-particle current. The size of this breakdown current is primarily independent of the tunnel coupling  $\Delta_{SAS}$ . Furthermore, the large critical tunneling current observed in the 8 nm sample does not obey the quadratic dependence on  $\Delta_{SAS}$ , as predicted by Hyart et al. [36]. Its size seems to be similar to that predicted by the static vortices model by Eastham et al. [55].

The area dependence of the critical Josephson current has been discussed in earlier publications [52] [56]. The conclusions from these works are based on comparison between several samples with different material properties. In this work, we compare the critical Josephson currents at two separate edges within a single sample, which is structured in a Corbino ring geometry. The lengths of the two edges differ substantially. The critical currents measured at these two edges are, nevertheless, nearly identical. This result confirms that the Josephson tunneling in bilayers at  $\nu_T = 1$  is not an edge, but a bulk effect. In addition, it gives also evidence that tunneling is taking place all over the sample area where interlayer coherence is present. Using a picture similar to the Andreev-Reflection (AR), applying interlayer tunneling currents at different edges can be understood as excess excitons being injected through different edges. Such excess excitons will recombine through tunneling in the bulk. Since both edges share the same bulk, they show the same critical current.

One can further investigate this phenomenon by applying a second constant Josephson tun-

---

<sup>1</sup>The real energy gap can be determined by multiplying the temperature with the Boltzmann constant  $k_B$ .



neling current simultaneously to the first one at the opposite edge of the Corbino ring. Possible interplay between the two edges, or between the two Josephson currents, can be studied in this way. We observe that the tunneling I-V curve at one edge appears to be shifted vertically by the same amount of current as applied at the opposite edge. If both currents have the same direction, applying a second current leads to a decrease of the critical value of the first current. Otherwise, one observes an increase of the first critical Josephson current. Again, one can apply the AR-like picture to explain these observations: when applying two Josephson currents with opposite signs, one effectively injects excess excitons with opposite polarizations into the two edges. These excitons can recombine just by compensating themselves, thus opening up a second recombination channel in addition to the intrinsic tunneling. If the currents applied at both edges have the same sign, the injected excitons have the same polarization and have to recombine by tunneling. Hence, the maximum intrinsic tunneling current is shared by the two edges. Since the two edges are effectively isolated from each other in the  $\nu_T = 1$  state, our result provides the first experimental evidence for two separate electrical currents to couple via exchange of charge-neutral objects—bilayer excitons. Such a coupling prevails up to a second Josephson current of 16 nA. We attribute the breakdown of the coupling beyond this current value to parasitic voltages building up between the two edges, since the bulk is not perfectly insulating.

In the closing chapter of this work, experimental results regarding excitonic counterflow are shown and discussed. Such a counterflowing current consists of electrons moving in opposite directions in the two layers. One thus has a charge-neutral flow of excitons. We again use Corbino samples for the demonstration of counterflow, since having two edges provides access to the bulk. Two setups are studied in this work: series counterflow with a shunt resistor connecting the two layers at one edge of the Corbino ring; and drag counterflow with a shunt resistor connecting the two edges of one layer. Both setups show clear evidence of excitonic counterflow: While the series counterflow setup provides direct results, the drag counterflow setup requires tilting as a control experiment. In the first case, excitonic counterflow can be detected through the shunt resistor after the critical Josephson tunneling current has been reached. In the latter case, tilting the sample to 75 degrees completely suppresses interlayer tunneling at  $\nu_T = 1$ , which has qualitatively no influence on the excitonic counterflow observed without tilting. Both results mean that the presence of Josephson tunneling current is not a prerequisite for the observation of excitonic counterflow. Furthermore, it can be shown in the drag counterflow setup that a Josephson tunneling current possibly contributes a Hall potential (voltage drop between the edges). Combined with the intrinsic circular current of the system at  $\nu_T = 1$  QHE, this additional Hall potential might contribute to the breakdown of the QHE. This result might be the first indirect but quantitative analysis of circular currents predicted for the Corbino geometry at QHE.

In the outlook, we emphasize that in order to clarify the small yet finite interlayer resistance associated with the Josephson effect observed in all bilayer samples, local measurements such as deploying a Single Electron Transistor (SET) could be helpful. In particular, it might be possible to study the role of merons as well as their anticipated fractional charge of  $\frac{1}{2}e$ . Magneto-transport measurements could continue to be important, particularly for comparing the temperature dependence of the longitudinal current and the excitonic counterflow. Such a comparison can give insights into the mechanism for the interaction between merons and quasi-particles as well as between merons and bilayer excitons, which is predicted to be similar by some models [36]. Finally, the large critical tunneling current exceeding  $1 \mu\text{A}$  should be further investigated. Last but not least, time dependent measurements should be developed to microscopically study the exciton picture as well as the Andreev-Reflection mechanism for the  $\nu_T = 1$  state.

# Chapter 8

## Deutsche Zusammenfassung

In den letzten Jahrzehnten hat die Revolution der Informationstechnologie die Art und Weise, wie die Menschen leben und arbeiten, drastisch verändert. Dieser Prozess ging einher mit den Fortschritten in der Physik kondensierter Materie, die es ermöglicht haben, ultraschnelle Schaltungen extrem klein und stabil herzustellen. Essentiell in diesem Prozess ist die Erhöhung der Kristallreinheit, auf die die Entdeckung der beiden wichtigsten Effekte in Halbleitersystemen der letzten drei Jahrzehnten—der geradzahlige und der fraktionelle quantisierte Hall Effekt (IQHE und FQHE)—zurückzuführen sind. Beide Effekte wurden in ultradünnen Grenzflächen zwischen Halbleitern bzw. zwischen Halbleiter und Metall bei hohen Magnetfeldern entdeckt, weshalb ein solches System zwei-dimensionales Elektronengas (2DEG) genannt wird. Zur Entdeckung beider Effekte wurden zwei Nobelpreise vergeben: an Klaus von Klitzing im Jahr 1985 sowie an Daniel Tsui, Horst Störmer und Robert Laughlin im Jahr 1998. Heutzutage lassen sich die beiden QHEs in neuartigen Systemen wie Graphen und Grenzflächen zwischen Oxiden sowie aus diesen zusammengesetzten komplexen Systemen realisieren.

Mitten in dieser Entwicklung ist auch ein besonderer QHE entdeckt worden. Wenn man zwei oben genannte 2DEGs in einen Abstand von nur wenigen Nanometern zusammenbringt und die Dichte in den beiden Dünnschichten sowie das Magnetfeld so einstellt, dass jeweils das niedrigste Landau-Niveau halb gefüllt ist, stellt sich ein QHE mit Füllfaktor eins ein. Erstaunlicherweise handelt es sich um einen korrelierten Zustand zwischen den Schichten, da jedes 2DEG allein bei Füllfaktor  $\frac{1}{2}$  keinen QHE aufweist. Daher wird dieser Effekt auch als ein QHE mit totalem Füllfaktor eins,  $\nu_T = 1$ , bezeichnet.

Theoretisch lässt sich der Grundzustand des  $\nu_T = 1$  Effektes sowohl als Bose-Kondensat von Interlagen-Exzitonen, als auch als spontane Magnetisierung von Pseudospin beschreiben. Im ersten Bild gehen Elektronen (besetzte Zustände des niedrigsten Landau-Niveaus) in einer Schicht mit den Löchern (unbesetzte Zustände des niedrigsten Landau-Niveaus) eine exzitoni-sche Bindung ein, die bei tiefen Temperaturen kondensiert. Im zweiten Bild fügt man jedem Ladungsträger einen weiteren Freiheitsgrad—Pseudospin—zu, der angibt, in welcher der beiden

Schichten sich dieser befindet. Im Grundzustand des  $\nu_T = 1$  werden alle Pseudospins ausgerichtet, so dass ein ferromagnetischer Zustand entsteht.

Das Spektakulärste an diesem Effekt ist der Interlagentunneleffekt, bei dem die Tunnelleitfähigkeit zwischen den beiden Schichten um Größenordnungen erhöht wird im Vergleich zum Tunneln ohne Magnetfeld, wobei es sich beim Letzteren um Tunneln von unkorrelierten Elektronen handelt. Der Tunnelstrom weist darüber hinaus einen kritischen Wert auf, nach dessen Überschreitung das Interlagentunneln drastisch unterdrückt wird. Aufgrund der starken Ähnlichkeiten zum Josephson-Tunneleffekt in konventionellen Supraleitern wird der in Doppellagen beobachtete Tunneleffekt als Josephson-like (Josephson-ähnlich) bezeichnet.

Bis zur Entstehung dieser Arbeit wurde der  $\nu_T = 1$  Josephson-Effekt an Doppellagensystemen mit Barrierendicke zwischen 10 nm und 12 nm untersucht. Diese Systeme weisen eine Symmetrie-Antisymmetrie-Energielücke  $\Delta_{SAS}$ , eine für die Tunnelstärke charakteristische Größe, von bis zu 100  $\mu\text{K}$  auf<sup>1</sup>. In dieser Arbeit wurden Doppellagenproben mit einer Barrierendicke von 8 nm untersucht, die ein  $\Delta_{SAS}$  von 1 mK aufweist. Der dadurch verstärkte Tunneleffekt führt in einer Kontaktgeometrie, in der der Tunnelstrom auch in der Probenebene fließt, dazu, dass der kritische Strom dem des longitudinalen Transports exakt gleich ist. In einer Probe mit 10 nm Barrierendicke lassen sich die beiden kritischen Ströme um eine Größenordnung unterscheiden. Der kritische Strom in der Ebene, der mit dem Durchbruch des QHEs zusammenhängt, ist ähnlich groß wie bei der tunnelstärkeren Probe. Eine alternative Kontaktgeometrie, in der die Kontakte für Stromzu- und -abfuhr genau übereinander liegen, führt zu einem gigantischen kritischen Josephson-Strom, der um drei Größenordnungen größer ist als in der 10 nm Probe. Aus diesen Messungen kann man schlußfolgern, dass der Durchbruch von  $\nu_T = 1$ -QHE alleine durch die Quasiteilchen-Ströme verursacht wird. Außerdem hängt die Größe des Durchbruchstroms primär nicht von  $\Delta_{SAS}$  ab. Der gigantische kritische Josephson-Strom scheint nicht mehr der quadratischen  $\Delta_{SAS}$ -Abhängigkeit aus dem Modell von Hyart et al. [36] zu gehorchen, könnte jedoch durch ein auf statischen Vortizes beruhendes Modell von Eastham et al. [55] erklärt werden.

Die Flächenabhängigkeit des kritischen Josephson-Stroms wurde bereits in älteren Arbeiten gezeigt [56] [52]. Diese Studien basieren jedoch auf Vergleich mit mehreren Proben, die alle unterschiedliche Materialeigenschaften besitzen. In dieser Arbeit wurde ein Vergleich des kritischen Stroms an zwei Rändern mit deutlich unterschiedlichen Längen in einer einzigen Probe durchführt. Die daraus resultierenden kritischen Ströme sind nahezu identisch. Dies bestätigt einerseits, dass der Josephson-Tunneleffekt in Doppellagen bei  $\nu_T = 1$  tatsächlich kein Randsphänomen sondern ein Flächeneffekt ist, und andererseits dass das Tunneln über der gesamten Fläche stattfindet, auf der die  $\nu_T = 1$ -Kohärenz präsent ist. In einem Bild, welches dem Andreev-Reflexion aus der Supraleitung ähnlich ist, lässt sich dieses Resultat dadurch veranschaulichen, dass die

<sup>1</sup>Die tatsächliche Energielücke wird aus Multiplikation mit der Boltzmann-Konstante  $k_B$  ermittelt.

an den Rändern injizierten Exzitonen sich über das gesamte Doppellagensystem verteilen, wobei sie durch Tunneln rekombinieren können. Da Tunneln ein Flächeneffekt ist, spielt es keine Rolle, an welchem Rand man die Exzitonen injiziert.

Dieses Phänomen kann man weiter studieren, indem man neben einem Josephson-Tunnelstrom einen zweiten Tunnelstrom am gegenüberliegenden Rand des Corbino Rings anlegt. Dabei lässt sich ein Wechselspiel zwischen den beiden Rändern bzw. zwischen den beiden Josephson-Strömen beobachten: die an einem Rand der Corbino-Probe gemessene Tunnelkurve verschiebt sich vertikal um genauso viel wie die Größe des zweiten kontaktierten Josephson-Stroms. Wenn beide Ströme dasselbe Vorzeichen haben, verringert sich der kritische Wert des ersten Stroms; im anderen Fall nimmt dieser zu. Darüber hinaus ändert sich die Form der Tunnelkurve kaum. Diese Beobachtungen lassen sich mit dem Austausch von Exzitonen zwischen den Rändern erklären: bei entgegengesetzten Strömen werden entgegengesetzt polarisierte Exzitonen an beiden Rändern injiziert, die sich aufheben können, was einen zweiten Rekombinationskanal neben dem intrinsischen Josephson-Tunneln öffnet. Bei gleich polarisierten Exzitonen wird der maximale Tunnelstrom von beiden Rändern bezogen, also sinkt der kritische Strom des einen Randes. Angesichts der Isolatoreigenschaft des Corbino-Volumenmaterials bei  $\nu_T = 1$  zeigt diese Beobachtung zum ersten Mal, dass zwei elektrisch getrennte Ströme durch Austausch von ladungsneutralen Objekten–Exzitonen miteinander wechselwirken können. Dieses Wechselspiel bleibt bei einem zweiten Josephson-Strom von bis zu 16 nA erhalten. Diese Begrenzung ist auf einen Ladungsstrom aufgrund eines parasitischen Potentialunterschieds zwischen den Rändern zurückzuführen.

Abschließend behandelt diese Arbeit den exzitonischen Counterflow, d.h. einen Strom, der in beiden Lagen in entgegengesetzten Richtungen fließt und deshalb ladungsneutral ist. Dazu wurden ebenfalls Corbino-Proben verwendet, die zwei Ränder besitzen und somit Zugang zum Probeninneren ermöglichen. Sowohl bei einer Beschaltungskonfiguration, in der ein externer Widerstand die Lagen am Innenrand kurzschließt (series counterflow) und ein Tunnelstrom angelegt wird, als auch bei einer anderen Konfiguration, in der ein Strom durch die obere Schicht und ein externer Widerstand die Ränder der unteren Schicht kurzschließt (drag counterflow), wurde ein Counterflow beobachtet. Während im ersten Fall ein direkter Nachweis durch ein zusätzliches Erdungsstück möglich war, musste im letzteren Fall die Probe verkippt eingebaut werden, um eine Magnetfeldkomponente parallel zur Probenebene einzuführen. Dieses parallele Magnetfeld unterdrückt den Josephson-Effekt vollständig. In beiden Messkonfigurationen wurde ein Counterflow beobachtet, während der Josephson-Tunneleffekt entweder teilweise oder ganz unterdrückt war. Dieses Ergebnis bedeutet, dass der  $\nu_T = 1$  Zustand nicht durch den Josephson-Tunnel charakterisiert wird. Nähere Untersuchungen bzgl. des Quasiteilchen-Stroms klären die Rolle des Josephson-Stroms ab: ein Tunnelstrom, der in der Probenebene fließt, führt zu einer Hallspannung, die mit der intrinsischen, dem Ringstrom entsprechenden Hallspannung

zusammen zum Durchbruch führt. Dieses Result stellt deshalb auch zum ersten Mal eine indirekte, jedoch quantitative Untersuchung des Ringstroms bei QHE in einer Corbino-Probe dar.

Im Ausblick auf zukünftige Untersuchungen erachten wir lokale Messungen zur Enthüllung des Meron-Konzeptes für besonders dringlich, da einige Erklärungen, u.a. der endliche Tunnelwiderstand bei  $\nu_T = 1$  damit zusammenhängen. Solche Messungen könnten mittels eines Einzelelektrontransistors (SET) realisiert werden, der zudem über die antizipierte fraktionelle Meronenladung von  $\frac{1}{2}e$  Aussagen liefern könnte. Auch normale Transportmessungen könnten weiterhin interessant sein, um beispielsweise die Temperaturabhängigkeit des longitudinalen Transportstroms mit der des exzitonischen Stroms zu vergleichen. Manche Modelle vermuten nämlich, dass sich die Meronen gleichermaßen auf den Transportstrom wie auf den Exzitonstrom wirken [36]. Weitere Messungen an Proben mit 8 nm bzw. noch kleinerer Barrierendicke könnten hilfreich sein, um den beobachteten Tunnelstrom von über  $1 \mu\text{A}$  näher zu studieren. Schließlich sind zeitabhängige Messmethoden zu entwickeln, um dem Exziton-Bild im Zusammenhang mit der Andreev-Reflektion auf den Grund zu gehen.

# Appendix A

## Additional Measurements

In this appendix, a few additional measurements will be shown which were not directly the focus in the previous measurement chapters but are either relevant to the background of those measurements or contain some phenomena which need to be clarified in future.

In Chap. 5 and Chap. 6, measurements with Corbino ring devices have been performed at the  $\nu_T = 1$  state. Fig. A.1 shows the full traces of the Coulomb drag in a sample from wafer #81981 (8 nm barrier). Both the current through the drive layer, as well as the voltages across the drive and drag layers are plotted. At  $\nu_T = 1$ , the current exhibits a minimum while the two voltages overlap completely and show a maximum. At higher filling factors, a similar effect can be observed. This effect is not seen in bilayer samples with larger barrier thickness, such as from wafer #81653. In samples from wafer #81981, to the contrary, this effect occurs whenever the top and bottom layers exhibit a QHE, no matter at which filling factors.

There exists fundamental difference between the Coulomb drag effect at  $\nu_T = 1$  and the effects at higher filling factors. The former effect results from the excitonic coupling between the layers, which is a consequence of the interlayer coherence, whilst the latter one results from the electrostatic coupling between the layers associated with single particle tunneling. This difference manifests itself as the much more profound overlap such as at  $\nu_T = 1$  then at other filling factors.

Tiemann et al. have shown that in a Hall bar bilayer sample, it is possible to detect the Hall resistance at filling factor one when applying a tunneling current at  $\nu_T = 1$  and measuring the interlayer voltage with voltage probes situated on separate sides of the tunneling current [56]. Fig. A.2 shows that such a Hall resistance can also be observed in a Corbino device: Interlayer current is applied at the outer edge while interlayer voltage is probed according to a *Hall* configuration. The value of the resulting slope is close to 26 k $\Omega$ . Besides providing a further evidence of the  $\nu_T = 1$  being a collective bilayer QHE, this result is intriguing since it occurs despite the hole in the middle of the Corbino ring device [64].

In Chap. 4, interlayer tunneling has been shown in two different contact configurations. For

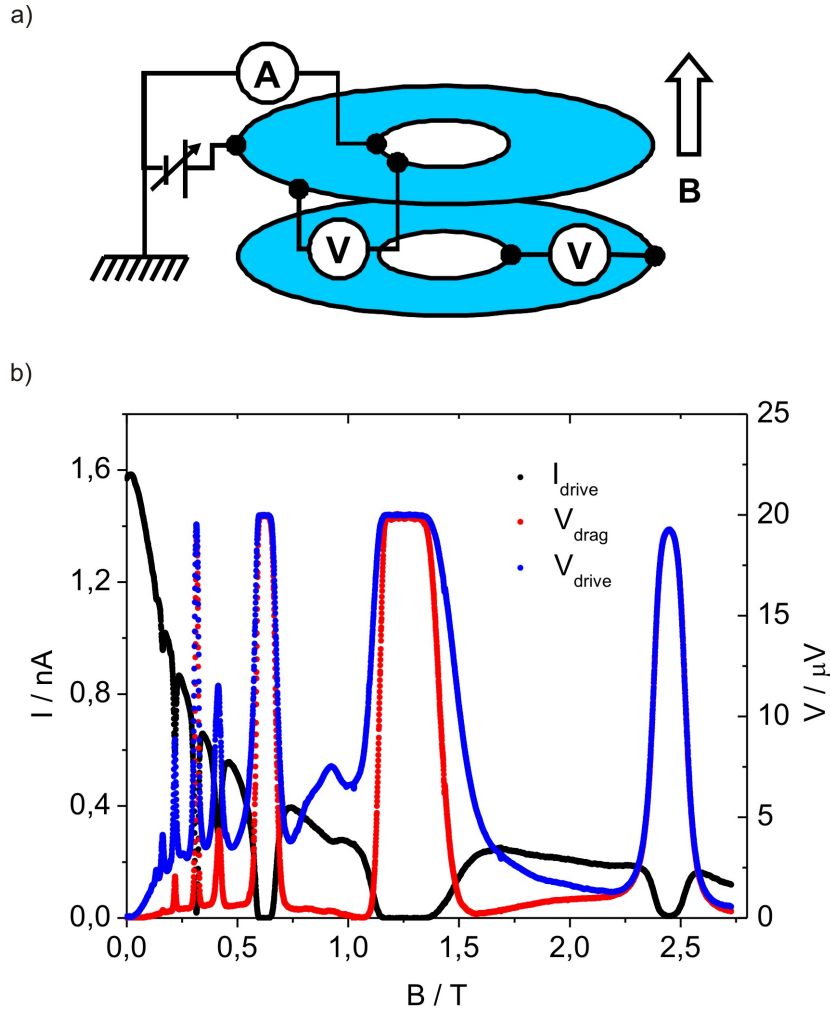


**Fig. A.1:** Coulomb drag in a Corbino ring sample from wafer #81981 (8 nm barrier) at 20 mK. The  $d/l_B$  ratio is set to 1.7. Densities are balanced between both layers. The Coulomb drag effect is clearly seen at  $\nu_T = 1$  at a magnetic field of 2.45 T. At other integer filling factors, the drag voltage is also close to the drive voltage, which is due to the strong coupling between the layers resulting in strong overlap of the wave functions.



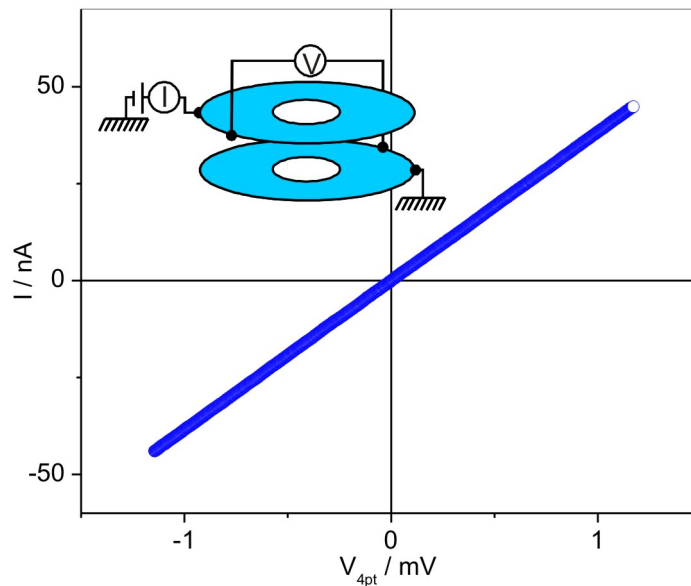


**Fig. A.2:** Interlayer tunneling at  $\nu_T = 1$ . The contacts at which the interlayer voltage is probed are situated on opposite sides of the current flow. The resulting interlayer resistance is close to  $26 \text{ k}\Omega$ , reminiscent of the quantum Hall resistance at  $\nu = 1$ .

sample HB-8, the tunneling configuration with source and drain contacts situated directly above each other exhibits a critical current three orders of magnitude larger than using the previous configuration enabling an in-plane current. Fig. A.3 shows the full tunneling trace. Surprisingly, the four-terminal interlayer voltage remains positive at negative source-drain voltage which leads to a negative interlayer current. This feature and the two minima at about  $V = -0.2 \text{ mV}$  and  $I = \pm 1 \mu\text{A}$  are currently not clear.

So far, the bilayer Josephson tunneling effect has been shown only up to a certain range of interlayer voltages, but not at even more elevated voltage bias. Fig. A.4 shows for the first time a more complete interlayer tunneling traces with four-terminal interlayer voltage up to  $\pm 4 \text{ mV}$ . This is shown for both the total filling factor  $\nu_T = 1$  (red trace) and the single filling factor  $\nu = 1$  (blue trace). The total filling factor is characterized by the zero-bias current, which does not occur at the single filling factor. In both cases, however, the interlayer current increases dramatically at higher voltages exceeding  $2 \text{ mV}$ , in both directions. The exact origin of such spikes are not known at the moment. Nonetheless, it is likely that this is not due to any collective many-body interaction, since it occurs for both the single and total filling factors of

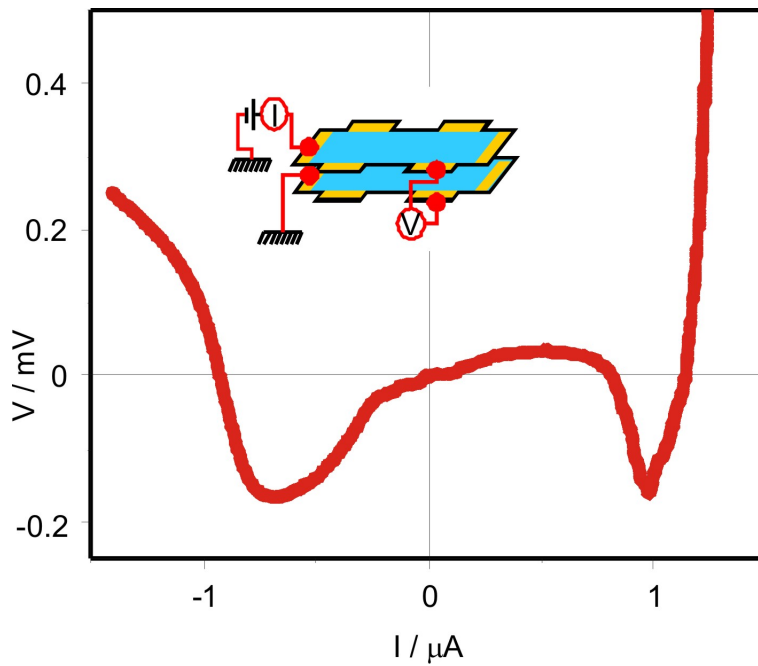


**Fig. A.3:** Tunneling I-V characteristic of sample HB-8 with the second contact configuration described in Chap. 4. In the negative current regime, the interlayer voltage is positive.

one.

In the drag counterflow experiment shown in Chap. 6, the currents have been plotted as a function of either the drive voltage  $V_{drive}$  or drag voltage  $V_{drag}$ . At  $\nu_T = 1$  state, the Coulomb drag effect leads to equal Hall voltages in both layers of a Hall bar, despite the current only being applied through the drive layer. It is the same effect that leads to the equal drive and drag voltages shown in Fig. A.5. In both sample CR-10 (a) and CR-8 (b),  $V_{drag}$  is plotted as a function of  $V_{drive}$  under both a large ( $3 \text{ G}\Omega$ ) and a small ( $1 \text{ k}\Omega$ ) shunt resistance. All traces are lying on the line  $y = x$ .

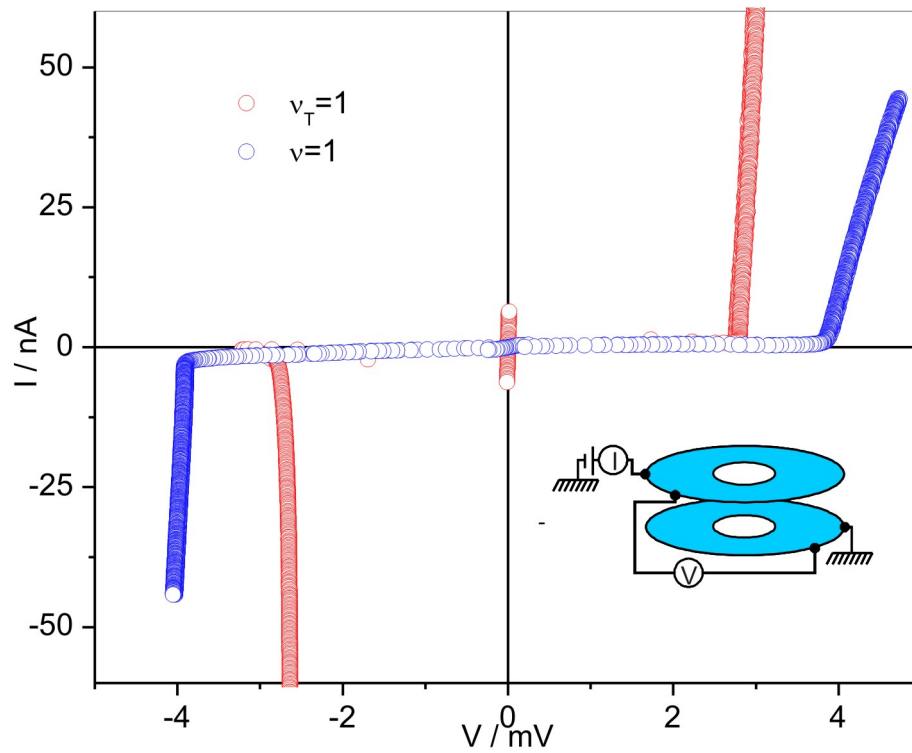


**Fig. A.4:** Interlayer I-V characteristics with four-terminal interlayer voltage up to  $\pm 4$  mV, measured at  $\nu_T = 1$  and  $\nu = 1$ . Both filling factors show spikes at higher voltages, which suggests that such spikes are not of a coherent nature. Their origin is, nonetheless, not known at the moment.

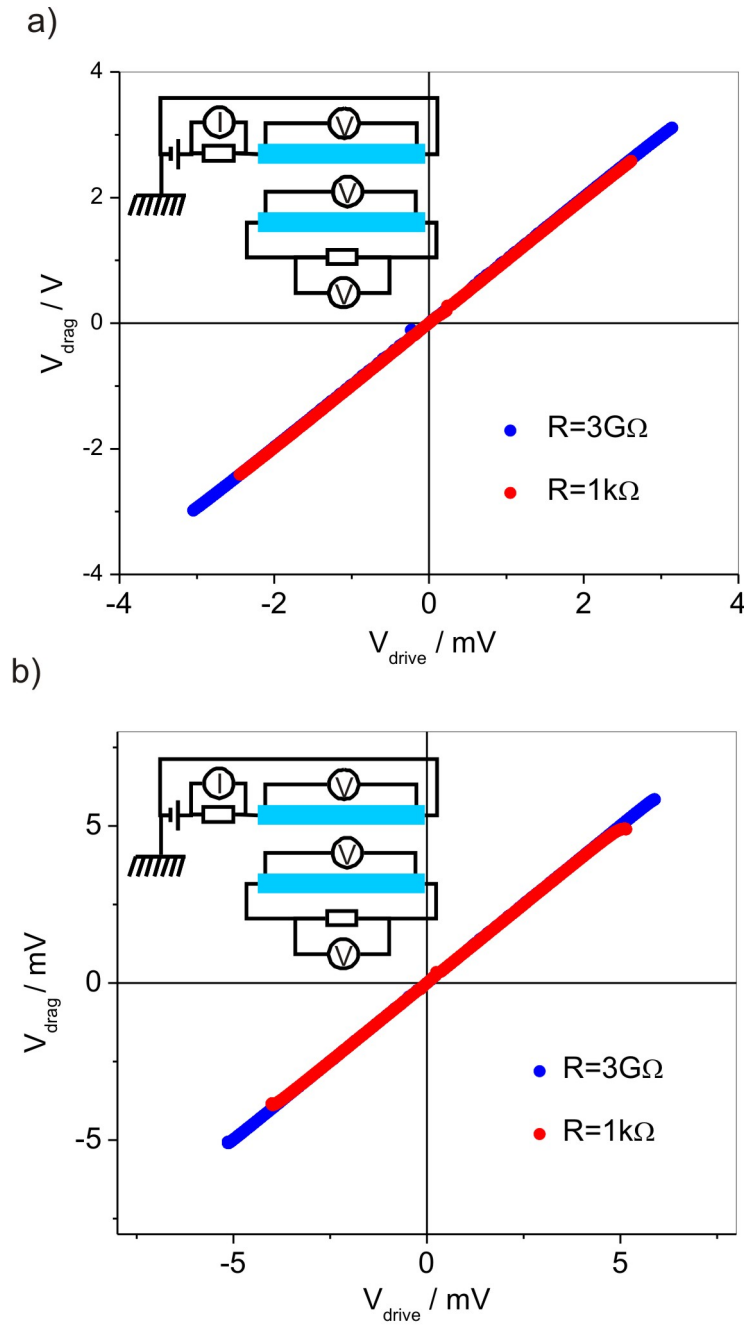


**Fig. A.5:** Load geometry in Corbino ring devices CR-10 (a) and CR-8 (b). In both graphs, the drag voltage (interedge voltage measured in the lower layer) is plotted versus the drive voltage. Both voltages are almost the same, indicating an established Coulomb drag effect.

# Appendix B

## Sample Fabrication and Measurement Setup

Within this work, bilayer samples based on GaAs have been fabricated. This chapter is dedicated to a description of the sample fabrication, which includes the sample structure and the fabrication process. Finally, the measurement setup will be introduced.

### B.1 Sample Fabrication

The growth of bilayer samples involves the pre-patterning of back gates, overgrowth of bilayer structure, etching of the mesa as well as evaporation of metallic ohmic contacts and front gates. First of all, a wafer with a back gate layer consisting of degenerately doped GaAs is pre-patterned into global and side back gates by photolithography and chemical wet etching. The pre-patterned backgate wafer is then cleansed and immediately brought into the chamber of molecular beam epitaxy (MBE), in which the desired double quantum well structure is overgrown. Again by means of photolithography and chemical wet etching, the mesa is structured into Hall bar or Corbino ring geometries. Ohmic contacts and global as well as side front gates are deposited on to the surface at the end. The contact alloy is also annealed so that it diffuses into the lower lying double quantum wells.

#### B.1.1 Sample Structure

Fig. B.1 shows a plan of MBE-overgrowth which has been applied in samples studied in some previous works [38] [65] and in this work. The double quantum wells, each with a width of 19 nm and separated by a superlattice barrier of typically 10 nm, are buried about 540 nm below the surface. The reason for the 2DES to be so deep is that a smaller spacer would lead to a higher electric field between the first doping layer and the upper quantum well, which under the same

doping would result in a higher charge carrier density. This would have the consequence that a larger front gate voltage would need to be applied in order to bring the system to a sufficiently low effective layer separation  $d/l_B$ . A second reason is that the two quantum wells need to be density-controlled individually, i.e. the global front/back gate should be responsible for only the upper/lower layer. A short spacer would increase the sensitivity for the global gates, so that the voltage difference for controlling the density in only one layer and both layers becomes small and the identification of depletion becomes more difficult. It might be helpful to have a shallow spacer for certain purposes, i.g. detection of the chemical potential of the 2DEG, which might be achievable by lowering the doping concentration at the same time. In order to change the interlayer coupling strength, the thickness of the insulating barrier between the two quantum wells can be varied by changing the number of the AlAs/GaAs cycles. Three different cycle numbers of 4, 5 and 6 have been used for this work, resulting in a barrier thickness of 8 nm, 10 nm and 12 nm. As will be explained in Chap. 4, such small difference in barrier thickness can lead to large difference in the properties of the  $\nu_T = 1$  state.

Two typical sample geometries used in this work are depicted in Fig. B.2(a) and (b). The Hall bar geometry (a) has a length of 0.88 mm and a width of 0.08 mm while the Corbino ring geometry (b) has an inner radius of 0.16 mm and an outer radius of 0.43 mm. The most important feature of our design that the two quantum wells can be separately contacted. This is enabled by deploying the FFP technique introduced by Fronius, Fischer and Ploog [66], which is schematically explained in Fig. B.2(c): after annealing, all ohmic contacts are connected to both the upper and lower quantum wells. By applying a negative voltage to the side front gates, the electronic layer in the contact arm directly below these front gates can be depleted, so that the connection between the upper layer and this contact is cut off. Similarly, a negative voltage applied to the side back gates can also disconnect the lower layer from specific contacts. Finally, one also has global front and back gates which are used to vary the electron densities of the bilayers individually.

### B.1.2 Fabrication Process

During the sample fabrication within this work, a number of technological difficulties have been encountered, in which all the components of the sample were involved. In the following, a summary about these difficulties as well as their solutions is described.

#### Backgate

The samples used for this work have differently grown back gate electrodes. For wafer #81653, the back gate has been grown by MBE while for wafer #81981, the back gate has been grown by the Metalorganic Chemical Vapor Deposition (MOCVD) technique. While there is no physical



**Fig. B.1:** Wafer growth plan of the samples used in this work. The two wafers differ in the number of AlAs/GaAs superlattice cycles for the interlayer barrier as well as the spacer superlattice between the second doping layer and the back gate.

difference between the two types of wafers, the surface of the MOCVD wafers seems to be generally cleaner than the MBE wafers, as can be seen in Fig. B.2. This is possibly due to the difference in the way how the wafers are grown: in the MOCVD procedure, individual atoms (Ga or As) are formed via chemical reactions, after which the target atoms are absorbed on the surface of the substrate forming the desired crystal, while the waste products diffuse away from the surface. This naturally results in a high material purity. In the MBE procedure, the wafer purity is controlled mainly by the purity of the material (Ga and As target cells). Provided that in both procedures, the vacuum quality of the growth chamber is similar, the use of material of less purity can lead to more defects visible on the surface. During the fabrication of back gates, while the pre-patterning steps including the surface cleansing immediately before the MBE-overgrowth of bilayer structures were well controlled, a considerable fraction of the back gates have shown two major problems: 1. The leakage currents were unacceptably high already

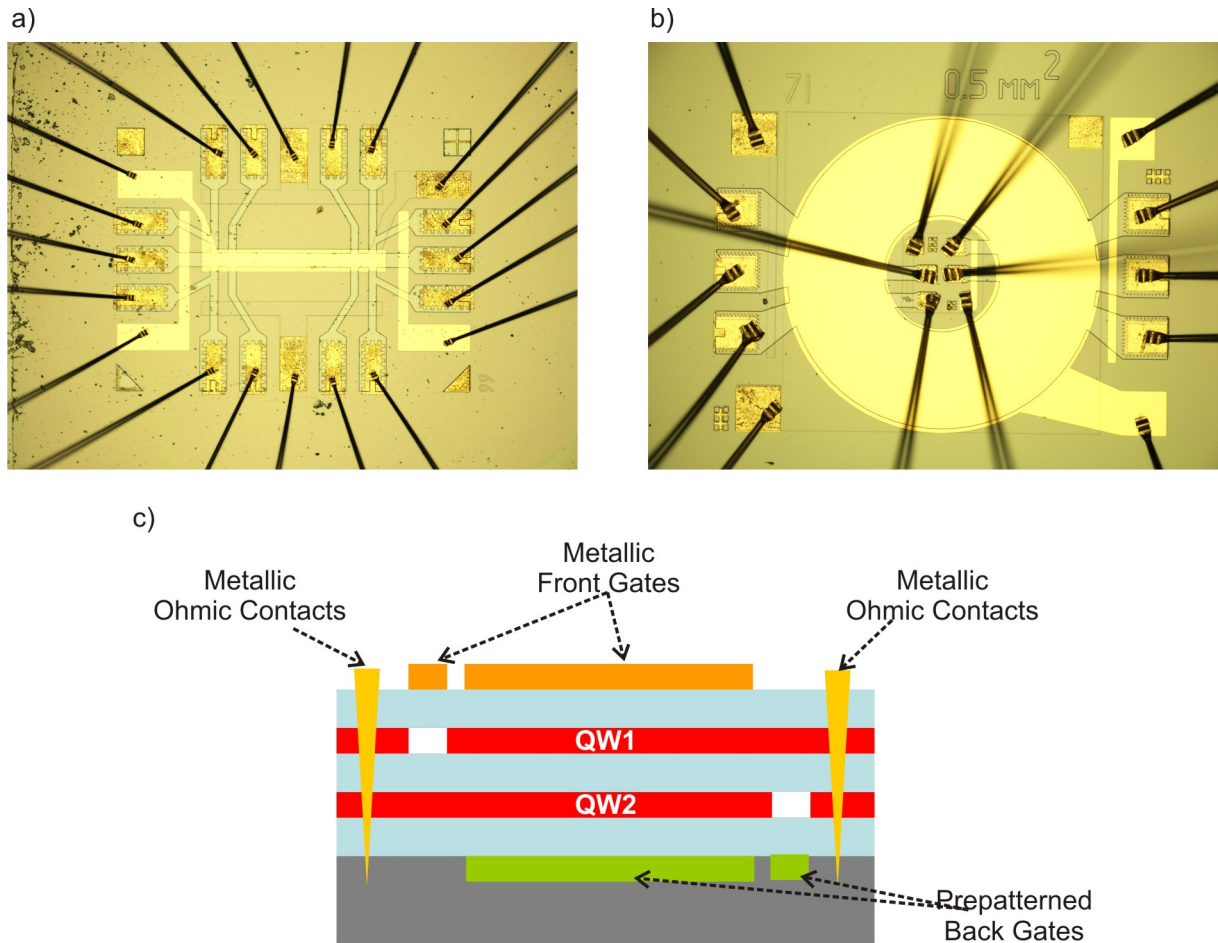


**Fig. B.2:** Microscopic pictures of the sample geometries used in this work: (a) Hall bar device with length 0.88 mm and width 0.08 mm. The back gate wafer shown here is grown by MBE. (b) Corbino ring device with outer diameter 0.86 mm and inner diameter 0.32 mm. The back gate wafer is grown by MOCVD. (c) Illustration of the selective depletion technique. After applying negative voltages to the front and back gates, the left contact is effective only to the lower and the right contact only to the upper layer.



within the depletion gate voltage, shown by the red curve in Fig. B.3b. 2. The charge carrier depletion under gate voltage application did not give clear steps for the side back gates which should mark the depletion of the two quantum wells. The latter is visible through the blue curve in Fig. B.3(c). The circuitry for the current biased depletion measurement is sketched in Fig. B.3(a), where the two-terminal voltage across the 2DES is measured while sweeping the back gate voltage.

Leakage current between the bilayer and the back gate is usually due to the poor insulating properties of the spacer between them. There are several ways to improve the insulating, such as increasing the mole fraction of Al in the superlattice in order to increase the DX center concentration or introducing a layer of low temperature (LT-) GaAs. The DX center concentration usually becomes significant at compositions close to the boundary between direct and indirect band gap, which is about  $x = 37\%$  for  $Al_xGa_{1-x}As$ . One thus cannot use an Al mole fraction of more than  $\sim 35\%$ . On the other hand, an Al mole fraction which is too small will also sacrifice the conduction band discontinuity. In current samples, the Al mole fraction is chosen to be 33% in the  $Al_xGa_{1-x}As$  layers. In a modified growth plan which includes a layer of AlGaAs in the superlattice between the lower doping layer and the back gate, while the overall thickness of the spacer remains similar to the previously used one. As shown by the red curve in Fig. B.3(b), the leakage current endurance has been increased to below  $-1.0V$ . The second alternative incorporating LT-GaAs has not been tried within this work. Since this method is also based on increasing the defect concentration, it should lead to similar effect as the first method.

The draw back of higher DX-center concentration is that the back gates become hysteretic when being swept back and forth. DX-centers are known as trapping centers for the charge carriers, which capture electrons being removed from the lower quantum well under a negative back gate bias voltage. When reversing the voltage, such electrons remain in the DX-centers and can only be thermally excited back into the quantum well.

Selective depletion of lower sharpness can have diverse reasons such as high density of defects in the back gate layer, in the overgrown structure or deviating process parameters. However, some of the fabricated bilayer samples indeed show fairly sharp depletion curves under negative back gate voltages. This means that the second problem is not a global but a local one. One of the most obvious local sources of problems is the gluing of samples to the chip carriers. The samples were first glued using a high vacuum grease called *Fixogum*. This material is viscous which easily has a rough surface, especially when too much of it is applied when gluing the samples. Due to the difference in stiffness between the grease and the chip carrier as well as sample, local stress might occur during the cooling process down to cryogenic temperatures. Although not fully understood on a microscopic basis, it can be anticipated that the bending of the sample can be compared with defects which might disturb the delocalization of electron wave functions in the plane. *PMMA*, a liquid photoresist which is largely used for

the electron-beam lithographic technique, is used to substitute the vacuum grease. Besides its enhanced gluing property at reduced thickness which means only a very thin layer is needed when gluing the sample, its liquid phase at room temperature enables a more homogeneous surface. This results in improved depletion characteristic manifested in sharper steps in the same two-terminal measurement at liquid helium temperature, shown by the red curve in Fig. B.3(c).

## Frontgate

The performance of the fabricated front gates is generally better than the back gates: they are less leaky, the depletion steps are sharper. However, some of the front gates also pose a problem depicted in Fig. B.4. Since the deposited front gate layer has a thickness of only 200 nm, much smaller than the thickness of the etched mesa of over 1  $\mu\text{m}$ , surface roughness especially at the etched mesa edges easily affects the front gates. Due to the difference of etching anisotropy concerning the crystallographic directions between different materials, the mesa edge profile after etching exhibits step-like structures, with rather clear roughness at the positions of the two doping layers. It has been found that such roughness leads to discontinuity of the front gates when this stretches across the contact arms, as highlighted in the left panel in Fig. B.4. This problem can be overcome by tilting the sample during the deposition of front gates.

## Ohmic Contact

AuGeNi alloys are the most widely used metal alloy for contacting GaAs-based electron systems. It was originally chosen because of its low eutectic point (360 °C) [67]. After deposition of the alloy onto the GaAs surface, it is heated up to above the eutectic point, so that it melts and diffuses into the GaAs. This enables also the gallium to out-diffuse into the gold and the germanium to settle onto gallium vacancies, thereby becoming a donor. Subsequent cooling down recrystallizes the GaAs and freezes in the dopants and defects. The use of nickel is mainly aimed at improving the wetting and enhancing the solubility of GaAs. However, nickel itself can diffuse effectively and become an acceptor. Therefore, the amount of nickel should generally be held small.

Typical resistance for the fabricated contacts is about 1.5 k $\Omega$  per 100  $\mu\text{m}$   $\times$  100  $\mu\text{m}$ , measured at liquid helium temperature and zero magnetic field. In presence of perpendicular magnetic field, however, some of the ohmic contacts show almost infinitely high temperature which indicates that they are not conducting. This is shown in the left panel of Fig. B.5 for the contact labeled B in the right panel. Therefore, something has to happen which changes the conducting properties of the contacts. Closer analysis has revealed that the problematic contacts share a property which is already visible under an optical microscope: as the right panels of Fig. B.5 show, contacts whose alloy covers the entire edge of the mesa, like the case of contact A, shows

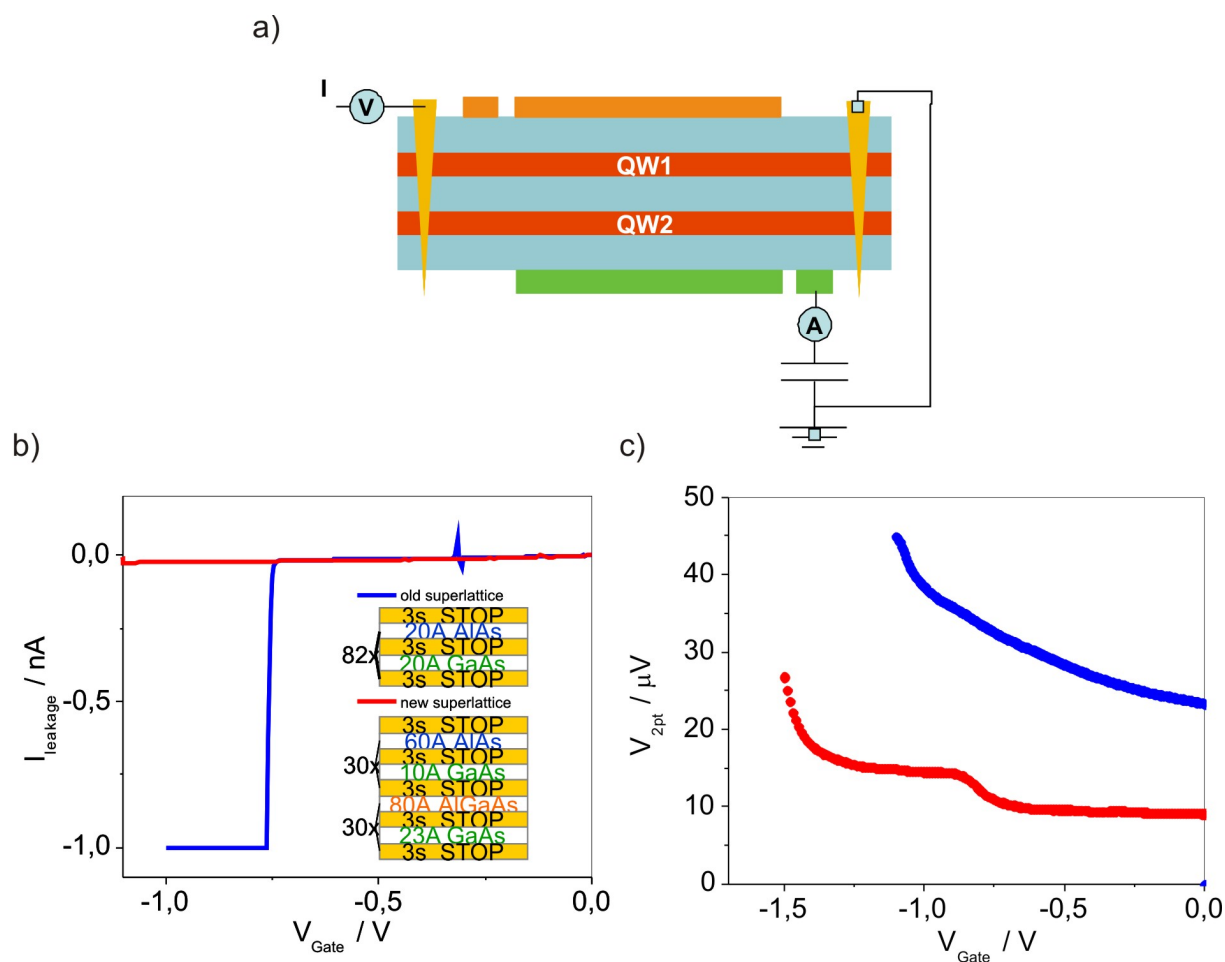


**Fig. B.3:** (a) Two-terminal depletion measurement: voltage across the 2DES is measured under current-bias while a back voltage is swept in the negative bias regime. (b) Improvement of the backgate endurance by modifying the superlattice structure between the second doping layer and the backgate layer. Adding AlGaAs instead of alternating AlAs and GaAs layers enables application of backgate voltage beyond  $-1V$ . (c) Improvement of the depletion effect after using *PMMA* instead of vacuum grease.

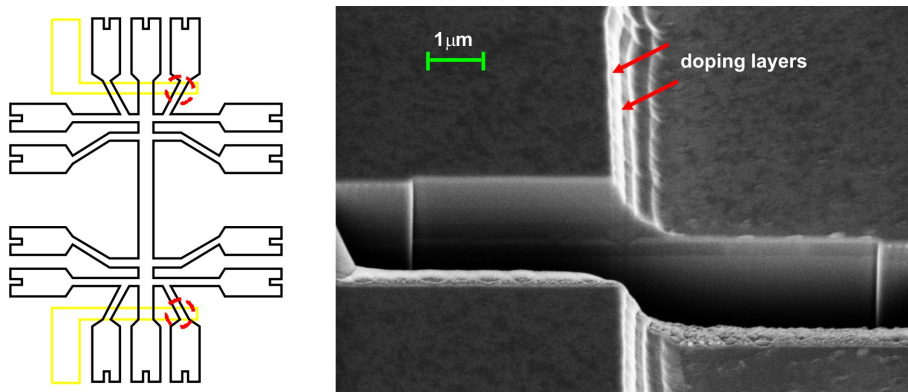


**Fig. B.4:** SEM image of the mesa profile after chemical wet etching. The edge shows discontinuous layered structures resulting from inhomogeneous etching rates for different materials. Front gates above such regions, shown in the left picture, can be broken.

normal resistance under magnetic field, while contacts whose alloy is deposited apart of the mesa edge with a distance of  $\geq 10 \mu\text{m}$  are almost insulating under the same magnetic field. This can be caused by the Corbino problem at sufficiently high magnetic fields, where the current flows around the edge regions of the mesa. Since such regions are normally formed within less than  $5 \mu\text{m}$  from the edge, one needs to move the alloy further beyond the mesa edge to make sure that the edges are fully covered.

Fig. B.6 shows the solution to the problematic described above. Magneto-transport curves are shown for both the top and bottom layers. In the left picture, metal alloy is beyond the mesa edge for contacts connecting the bottom layer but not covering the mesa edge for those of the top layer. In the right picture, a modified lithography mask which includes contact structures enabling the metal alloy to be diffused beyond the mesa edge has been used. The ohmic contacts for both the top and bottom layers show normal behavior.

## B.2 Measurement Setup

Due to the fragility of the  $\nu_T = 1$  quantum Hall state associated with the relatively small activation energy gap of the order of  $\sim 1 \text{ K}$  [38], it is crucial to have extremely low temperatures, in order to approach the ground state of the bilayer system. This is provided by a  $He^3/He^4$  dilution refrigerator, in which superconducting magnets are embedded. The principle of the dilution cooling is based on the mixing enthalpy of  $He^3/He^4$  mixture. As the phase diagram in Fig. B.7(a) shows, when cooling the  $He^3/He^4$  mixture below  $0.9 \text{ K}$ , a coexistence of two

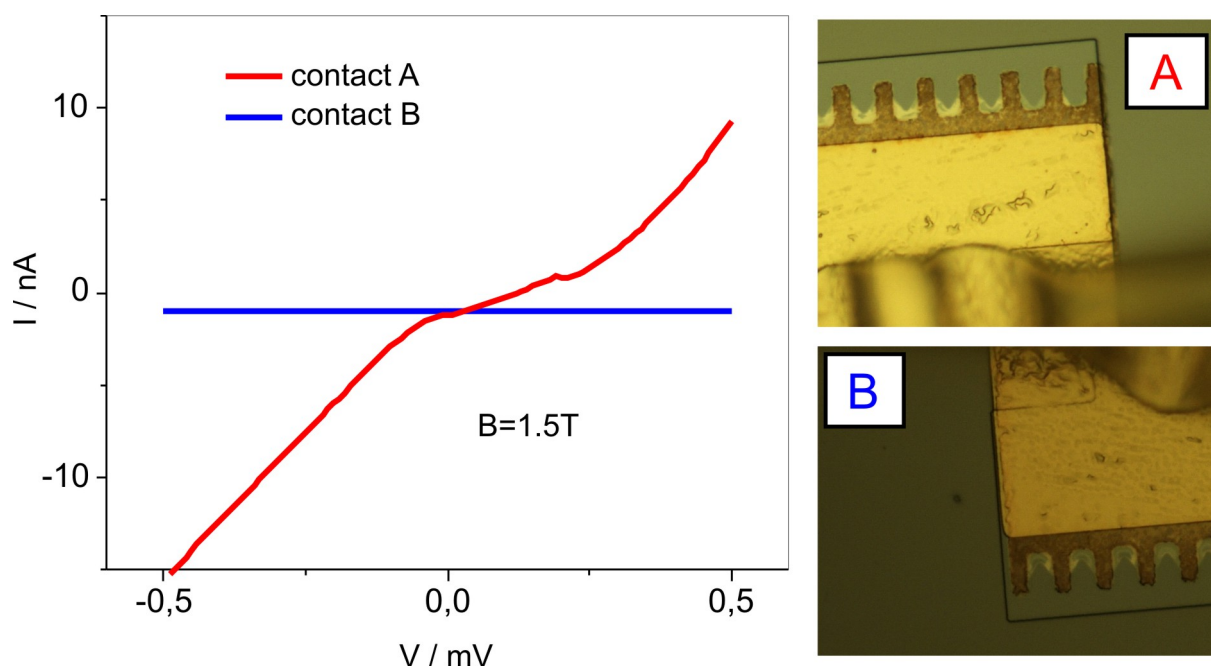


**Fig. B.5:** Ohmic contacts with different results of alloy evaporation exhibit large difference in resistance in presence of perpendicular magnetic field: for contact A, the metal alloy was evaporated across the (right) edge, resulting in a normal contact resistance ( $\sim 50 \text{ k}\Omega$ ); for contact B, the metal alloy was evaporated before reaching the (left) edge, resulting in an almost infinite resistance.

phases occurs: one phase with a very low  $He^3$  fraction and another phase with almost 100% of  $He^3$ . At such a low temperature, the  $He^4$  becomes a superfluid, which provides an environment for the  $He^3$  atoms as if they are in their gas phase. Therefore, when  $He^3$  atoms diffuse from the concentrated phase into the diluted phase, heat can be absorbed from the environment to support the quasi-evaporation process. This heat is called the mixing enthalpy, which needs to be paid or created when mixing two pure chemical substances together. Thermodynamically, the mixing enthalpy for  $He^3/He^4$  mixture occurs out of two reasons: firstly,  $He^3$  atoms are larger than  $He^4$  atoms so that in the diluted phase more van-der-Waal binding can take place between the two isotopes than between  $He^3$  atoms, which saves up energy; secondly, since  $He^3$  atoms are fermions, the Fermi energy in the diluted phase will be lower than in the concentrated phase, which means more energetic states can be occupied thermally in the diluted phase.

After crossing the phase boundary, as sketched in Fig. B.7b, the  $He^3$  atoms in the diluted phase will need to be pumped away so that further  $He^3$  atoms can cross the phase boundary and the cooling process can be maintained. However, the vapor pressure of  $He^3$  is low at low temperatures. A local heater called *Still* is therefore used to locally heat up the gas to about  $1K$

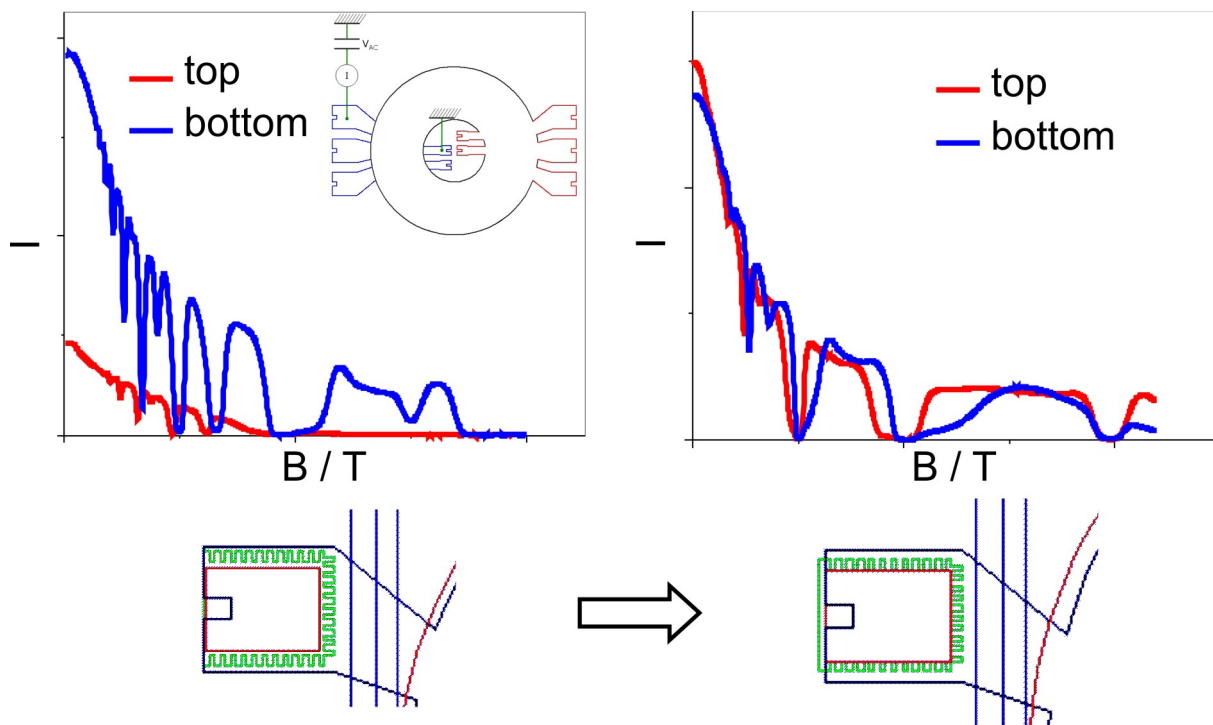


**Fig. B.6:** Contact mask has been modified to enable evaporation of metal alloy across the edge, as shown by the right sketch. All contacts tested with this modified geometry have shown normal resistance in magnetic field.

to increase the vapor pressure, which is followed by mechanical pumps in the mixing chamber pumping line. Finally, the  $He^3$  is condensed and sent back to the concentrated phase in the mixing chamber. As the phase diagram tells, there is 6% of  $He^3$  in the diluted phase even at absolute zero temperature. Therefore, nature provides a mixture which theoretically can cool down to the absolute  $0K$ . However, this is usually limited by the thermal shielding, the heat exchange efficiency as well as the pumping power of the system. Furthermore, shielding from high frequency rays as well as proper grounding during the entire measurement procedure (including sample loading) have proven crucial for reaching the lowest possible base temperature. In the dilution refrigerator used for this work, the lowest mixing chamber temperature is typically  $\sim 10mK$ .

Fig. B.8 explains how the different components are set up for the low temperature measurements involved in this work. The sample is mount in a sample holder and connected to a switch box via electrically shielded cables. Low noise lock-in amplifiers and preamplifiers are used for magneto-transport and interlayer tunneling measurements. The read-out is enabled by digital multimeters. All devices including the sample are grounded to a common ground via the

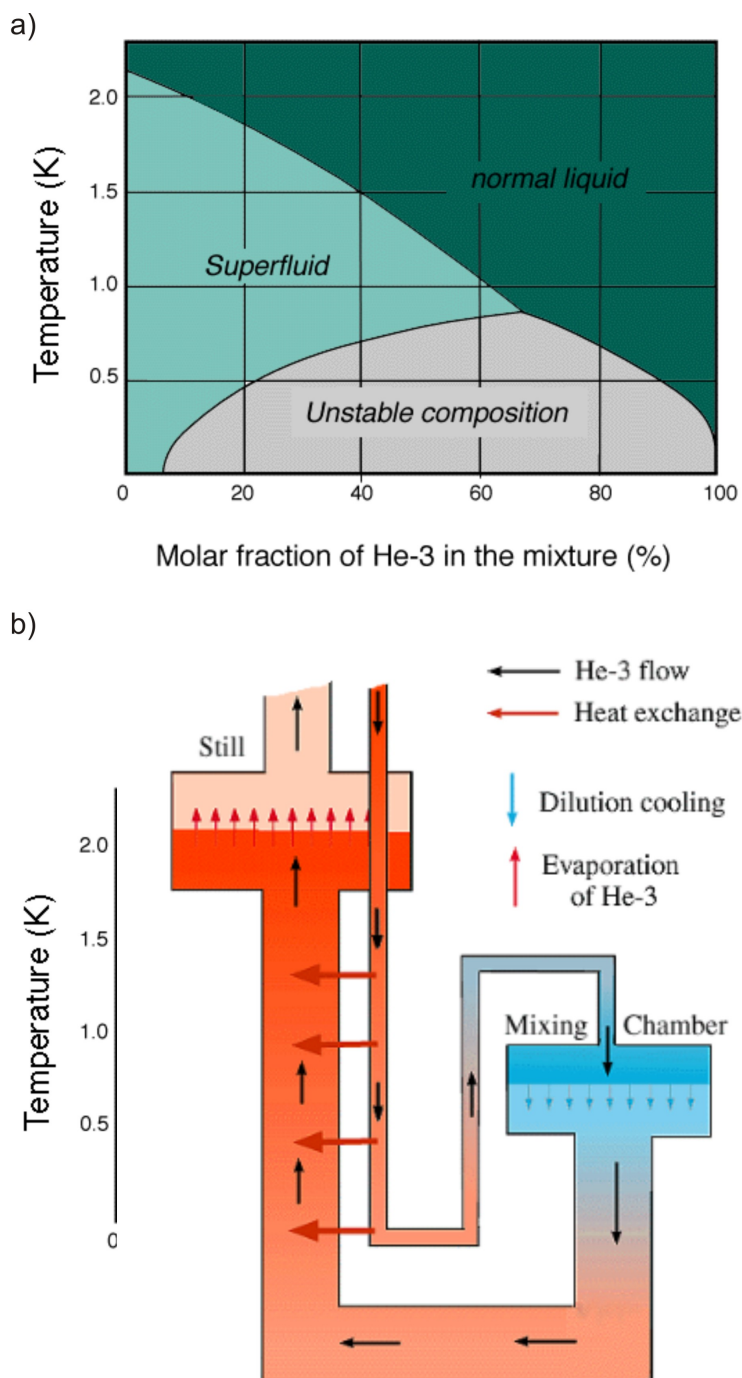


**Fig. B.7:** Working principle of a dilution fridge: (a) Phase diagram of  $He^3/He^4$  mixture which shows coexistence of a  $He^3$ -rich and  $He^3$ -poor phase below  $0.9K$ . (b)  $He^3$  flow and heat exchange inside a typical  $He^3/He^4$  dilution refrigerator.

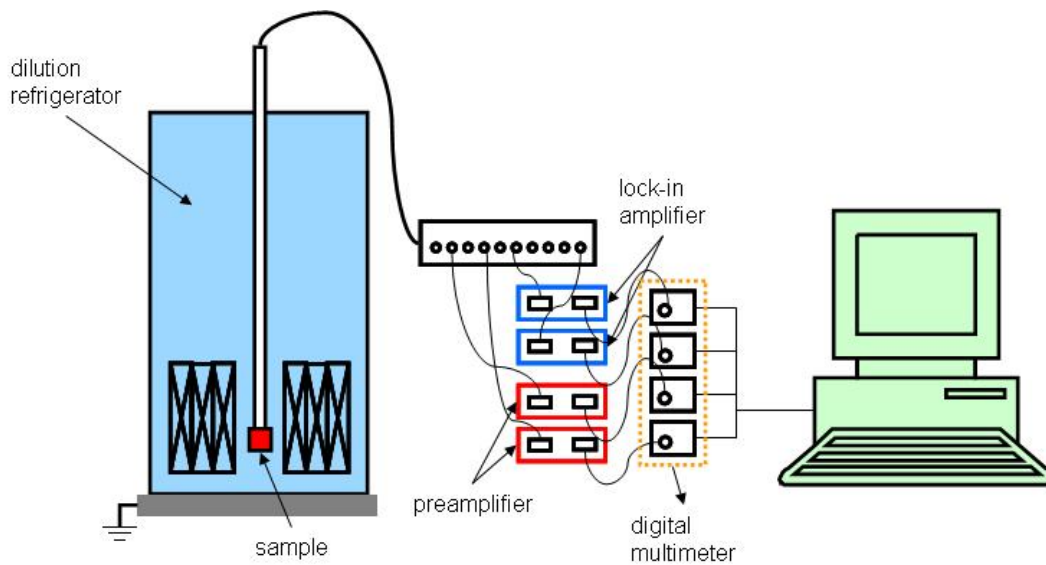


**Fig. B.8:** Schematic illustration of the measurement setup. The  $He^3/He^4$  dilution refrigerator with built-in superconducting magnets provides a sample temperature of down to  $\sim 20mK$  and a magnetic field up to  $21.5T$ . Data are collected using standard lock-in as well as preamplifiers, which are connected to digital multimeters. Communication with the computer is realized via GPIB environment.



surface of the dilution refrigerator. The data are retrieved via GPIB environment.

### B.3 Sample Fabrication Parameters

Back Gates		Parameters
Mask	Cleaning	piranha ( $\text{H}_2\text{O}_2:\text{H}_2\text{SO}_4 = 1:2$ ) ~2 min
Wafer Backside	Removal of Gallium	(grade 1), tissue with acetone
	Front side removal	acetone onto front side, $\text{N}_2$ drying
Back Gate	Cleaning	acetone in USB – 4 min → Isopropanol – 1 min
	S1805 (Positive PR)	4500 rpm – 30 sec
	Baking	85 °C – 20 min, uncovered
	Exposure	7.5 sec using MJB3, hard mode
	Develop (AZ726)	60 sec → DI Water
	Etching	$\text{BHF}:\text{H}_2\text{O}_2:\text{H}_2\text{O} = 20:120:1200 \rightarrow 120 \text{ nm}$ (~20% below the BG) [PR removal: 3 hours NMP @ 80°C]
Wafer Cleansing	Pre-cleansing	boiling acetone → 10 min
	Etching	$\text{H}_2\text{SO}_4$ in USB → 10 min
	Cleansing	DI- $\text{H}_2\text{O}$ in USB → 10 min
	Oxide removal	semicoclean → 2 min
	Cleansing	DI- $\text{H}_2\text{O}$ in USB → 10 min
		DI- $\text{H}_2\text{O}$ without USB → 1 min
		DI- $\text{H}_2\text{O}$ OFF → 1 min
	Drying	80 sec at 200 rpm → 70 sec at 1000 rpm
Oxide formation		
MBE		
Wafer Backside	Removal of Gallium	(grade 1), tissue with acetone
	Front side removal	acetone onto front side, $\text{N}_2$ drying
Protection spin coating	Cleansing	acetone in USB – 4 min → isopropanol – 1 min
	S1805 (Positive PR)	4500 rpm – 30 sec
	Baking	85 °C – 10 min, uncovered
Scribing		

Fig. B.9: Fabrication parameters for the pre patterning of back gates.

### B.4 Wafer Growth Parameters

Mesa, Contacts and Front Gates		Parameters
Mesa	S1805 (Positive PR)	30 sec @ 6000 rpm
	Bake	2 min @ 90 °C
	Exposure	8.0 sec, hard mode MA6, alignment gap 30 μm
	Develop (AZ726)	40 sec → DI Water
	Etching	H <sub>2</sub> SO <sub>4</sub> :H <sub>2</sub> O <sub>2</sub> :H <sub>2</sub> O = 0.5:4:200 (ml) → 1150 nm (~9 min 10 sec) After preparing the solution, stir it quickly for 3 min, then slowly for 3 min. Then stop stirring and pour 25 ml to a separate measuring jug to do the test etching.
Ohmic Contact	AZ5214E (Negative PR)	30 sec @ 6000 rpm
	Bake	4 min @ 90 °C
	Exposure	8.0 sec, hard mode MA6, alignment gap 30 μm
	Post Bake	1 min @ 122 °C
	Flood Exposure	60 sec, flood mode MA6
	Develop (AZ726)	45 sec → DI Water
	Etching	H <sub>2</sub> SO <sub>4</sub> :H <sub>2</sub> O <sub>2</sub> :H <sub>2</sub> O=0.5:4:200 (ml) → 180 nm (~1 min 30 sec)
	Oxide Removal	semicoclean 2 min → H <sub>2</sub> O 5 sec → HCl 5 sec → H <sub>2</sub> O 5 sec
	Metallization	Au: front left; Ge: front right; Ni: back wall; overnight pumping, rotate sample gently 1.) Ni: 1.0 Å/s (I~95A) → 120 Å (m <sub>Ni</sub> ~150 mg), 180° 2.) Ge: 2.3 Å/s (I~6A) → 1584 Å (m <sub>Ge</sub> ~200 mg), 50° 3.) Au: 3.3 Å/s (I~7.5A) → 3216 Å (m <sub>Au</sub> ~1500 mg), 50° 4.) Ni: 1.0 Å/s (I~95A) → 480 Å, 180°
	Lift-off	Δt <sub>acetone</sub> ~5 min, then rinse the sample with acetone before putting it into isopropanol. This will usually be sufficient.
	Annealing with 20% H <sub>2</sub> & 80% N <sub>2</sub>	Users/Monika/az500 120 sec @ 370 °C → 50 sec @ 440 °C → 2 sec @ 100 °C
Front Gate	AZ5214 (Negative PR)	30 sec @ 6000 rpm
	Bake	4 min @ 90 °C
	Exposure	8.0 sec, hard mode MA6, alignment gap 30 μm
	Post Bake	1 min @ 122 °C
	Flood Exposure	60 sec, flood mode MA6
	Develop (AZ726)	45 sec → DI Water
	Oxide Removal	semicoclean 2 min → H <sub>2</sub> O 5 sec
	Metallization	Cr: left; Au: right; pumping for 3 hours, sample maximally tilted and gently rotated 1.) Cr: 0.5 Å/s (SP1~33%, SP2~38%) → 100 Å 2.) Au: 2.0 Å/s (SP1~35%, SP2~42%) → 1800 Å (m <sub>Au</sub> ~700 mg)
	Lift-off	If the lift-off method used for ohmic contacts does not work out here, especially for the inner part of Corbino ring, then try: Δt <sub>NMP</sub> ~20 min @ 80 °C, then rinse with acetone before isopropanol.

Fig. B.10: Fabrication parameters for mesa, ohmic contact and front gates.

Tab. B.1: Growth parameter of wafer #81653 (upper table) and of wafer #81981 (lower table)

material	thickness
GaAs	200 Å
AlGaAs	2000 Å
AlGaAs:Si	400 Å
AlGaAs	2800 Å
GaAs	187 Å
GaAs/AlAs SL	2.8 Å/17 Å × 5
GaAs	190 Å
AlGaAs	3000 Å
AlGaAs:Si	350 Å
AlGaAs	300 Å
GaAs/AlAs	20 Å/20 Å × 82
GaAs	1000 Å
GaAs	200 Å
AlGaAs	2000 Å
AlGaAs:Si	400 Å
AlGaAs	2800 Å
GaAs	187 Å
GaAs/AlAs SL	2.8 Å/17 Å × 4
GaAs	190 Å
AlGaAs	3000 Å
AlGaAs:Si	350 Å
AlGaAs	300 Å
GaAs/AlGaAs	23 Å/80 Å × 30
GaAs/AlAs	10 Å/60 Å × 30
GaAs	1000 Å



# Appendix C

## Calculation of $\Delta_{SAS}$

There are different ways to calculate the symmetry-antisymmetry gap  $\Delta_{SAS}$ . One can start from the energy band diagram and perform the self-consistent numerical calculation [59] [56]. One can also determine it from the tunneling I/V characteristic at B=0. This method is based on the assumption that the tunneling conductance at  $\nu_T = 1$  shows a Lorentzian shape according to

$$G = \frac{I}{V} = G_0 \frac{1}{1 + (eV/\Gamma)^2} \quad (\text{C.1})$$

where

$$G_0 = e\rho_0 A \frac{T^2}{\hbar} \frac{2e}{\Gamma}. \quad (\text{C.2})$$

The parameters are listed in Tab. C.1.

Hence, if the conductance and its broadening at B=0 are given, one can calculate the tunneling amplitude T and thus  $\Delta_{SAS}$ . This has been done for the wafer #81981 by using a Corbino sample, whose tunneling I/V characteristic is shown in Fig. C.1:

The interlayer resistance at V=0 can be determined by the slope of the I-V curve and is approximately 4 k $\Omega$ , which corresponds to a conductance peak of 250  $\mu\text{S}$ . The broadening is

parameter	meaning
G	conductance
$G_0$	conductance at B=0
$\Gamma$	broadening at B=0
$\rho_0 := m^*/\pi\hbar^2$	density of states
A	sample area
T ( $\Delta_{SAS} = 2T$ )	tunneling amplitude

Tab. C.1: Parameters for estimation of  $\Delta_{SAS}$ .

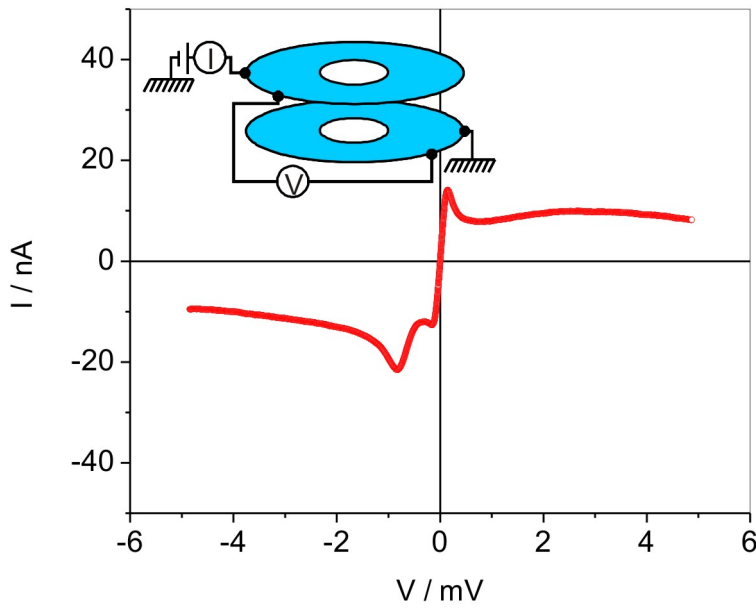


**Fig. C.1:** Interlayer tunneling in a Corbino ring sample CR36 from wafer #81981 at zero magnetic field and a mixing chamber temperature of 20 mK. The densities of both layers are balanced to  $3 \times 10^{10} \text{cm}^{-2}$ , giving a  $d/l_B$  ratio of  $\sim 1.7$ .

about  $140 \mu\text{eV}$ . Using Eq. C.2, the  $\Delta_{SAS}$  can be determined to 1 mK. The second minimum in the negative voltage branch is currently unclear.

# References

- [1] U. Klass, W. Dietsche, K. von Klitzing and K. Ploog, *Zeitschrift für Physik B* **82**, 351 (1991).
- [2] K. Koch, *Phys. Rev.* **82**, 460 (1951).
- [3] M. Büttiker, *Phys. Rev. B* **38**, 9375 (1988).
- [4] P. Weitz, E. Ahlswede, J. Weis, K. von Klitzing and K. Eberl, *Physica E: Low-dimensional Systems and Nanostructures* **1-4**, 247 (2000).
- [5] D. Chklovskii, B. Shklovskii and L. Glazman, *Phys. Rev. B* **46**, 4026 (1992).
- [6] D. Chklovskii, K. Matveev and B. Shklovskii, *Phys. Rev. B* **47**, 12605 (1993).
- [7] K. Lier and R. Gerhardts, *Phys. Rev. B* **50**, 7757 (1994).
- [8] K. Güven and R. Gerhardts, *Phys. Rev. B* **67**, 115327 (2003).
- [9] A. Siddiki and R. Gerhardts, *Phys. Rev. B* **70**, 195335 (2004).
- [10] J. Weis and K. von Klitzing, *Philosophical Transactions of the Royal Society* **369**, 3954 (2011).
- [11] G. Nachtwei, *Physica E* **4**, 79 (1999).
- [12] K. Panos, **to be published**, (2012).
- [13] S. Kawaji, H. Hirakawa and M. Nagata, *Physica B* **184**, (1993).
- [14] N. Balaban, U. Meirav and H. Shtrikman, *Phys. Rev. B* **52**, R5503 (1995).
- [15] S. Komiyama, Y. Kawaguchi, T. Osada and Y. Shiraki, *Phys. Rev. Lett.* **77**, 558 (1996).
- [16] G. Nachtwei, Z. Liu, G. Lütjering, R. Gerhardts, D. Weiss, K. v. Klitzing and K. Eberl, *Phys. Rev. B* **57**, 9937 (1998).

- [17] D. Tsui, H. Störmer and A. Gossard, *Phys. Rev. Lett.* **48**, 1559 (1982).
- [18] J. Jain, *Phys. Rev. Lett.* **63**, 199 (1989).
- [19] J. Jain, *Physics Today* **53**, 39 (2000).
- [20] R. Willett, J. Eisenstein, H. Störmer, D. Tsui, A. Gossard and J. English, *Phys. Rev. Lett.* **59**, 1776 (1987).
- [21] B. Halperin, *Helv. Phys. Acta* **56**, 75 (1983).
- [22] D. Zhang, Master's thesis, University of Stuttgart, 2010.
- [23] S. Murphy, *Phys. Rev. Lett.* **72**, 728 (1994).
- [24] K. Yang, K. Moon, L. Belkhir, H. Mori, S. Girvin, A. MacDonald, L. Zheng and D. Yoshioka, *Phys. Rev. B* **54**, 11644 (1996).
- [25] H. Fertig, *Phys. Rev. B* **40**, 1087 (1989).
- [26] A. MacDonald and E. Rezayi, *Phys. Rev. B* **42**, 3224 (1990).
- [27] J. Bardeen, L. N. Cooper and J. R. Schrieffer, *Phys. Rev.* **108**, 1175 (1957).
- [28] Z. Ezawa and A. Iwazaki, *Phys. Rev. Lett.* **70**, 3119 (1993).
- [29] Z. F. Ezawa and A. Iwazaki, *Phys. Rev. B* **47**, 7295 (1993).
- [30] Z. Ezawa and A. Iwazaki, *I.J.Mod.Phys.* **8**, 2111 (1994).
- [31] J. Blatt, K. Böer and W. Brandt, *Phys. Rev.* **126**, 1691 (1962).
- [32] K. Kowalik-Seidl, X. Vögele, B. Rimpfl, G. Schinner, D. Schuh, W. Wegscheider, A. Holleitner and J. Kotthaus, *Nano Letters* **12**, 326 (2012).
- [33] A. High, J. Leonard, A. Hammack, M. Fogler, L. Butov, A. Kavokin, K. Campman and A. Gossard, *Nature* **483**, 584 (2012).
- [34] S. Girvin, *Physics Today* **53**, 39 (2000).
- [35] I. Spielman, J. Eisenstein, L. Pfeiffer and K. West, *Phys. Rev. Lett.* **87**, 036803 (2001).
- [36] T. Hyart and B. Rosenow, *Physical Review B* **83**, 155315 (2011).
- [37] M. Kellogg, I. Spielman, J. Eisenstein, L. Pfeiffer and K. West, *Phys. Rev. Lett.* **88**, 126804 (2002).



- [38] R. Wiersma, J. Lok, S. Kraus, W. Dietsche, K. von Klitzing, D. Schuh, M. Bichler, H. Tranitz and W. Wegscheider, *Phys. Rev. Lett.* **93**, 266805 (2004).
- [39] B. Josephson, *Physics Letters* **1**, 251 (1962).
- [40] D. McDonald, *Physics Today* **54**, (2001).
- [41] S. Shapiro, *Phys. Rev. Lett.* **11**, 80 (1963).
- [42] I. Spielman, J. Eisenstein, L. Pfeiffer and K. West, *Phys. Rev. Lett.* **84**, 5808 (2000).
- [43] L. Tiemann, W. Dietsche, M. Hauser and K. von Klitzing, *New Journal of Physics* **10**, 045018 (2008).
- [44] J. Eisenstein and A. MacDonald, *Nature* **432**, 691 (2004).
- [45] K. Park and S. Das Sarma, *Phys. Rev. B* **74**, 035338 (2006).
- [46] A. Stern, S. Girvin, A. MacDonald and N. Ma, *Phys. Rev. Lett.* **86**, 1829 (2001).
- [47] M. Fogler and F. Wilczek, *Phys. Rev. Lett.* **86**, 1833 (2001).
- [48] Y. Joglekar and A. MacDonald, *Phys. Rev. Lett.* **87**, 196802 (2001).
- [49] M. Kellogg, J. Eisenstein, L. Pfeiffer and K. West, *Phys. Rev. Lett.* **93**, 036801 (2004).
- [50] E. Tutuc, M. Shayegan and D. Huse, *Phys. Rev. Lett.* **93**, 036802 (2004).
- [51] Y. Yoon, L. Tiemann, S. Schmult, W. Dietsche, K. von Klitzing and W. Wegscheider, *Phys. Rev. Lett.* **104**, 116802 (2010).
- [52] L. Tiemann, Y. Yoon, W. Dietsche, K. von Klitzing and W. Wegscheider, *Phys. Rev. B* **80**, 165120 (2009).
- [53] D. Fil and S. Shevchenko, *Journal of Physics: Condensed Matter* **21**, 215701 (2009).
- [54] J. Su and A. MacDonald, *Phys. Rev. B* **81**, 184523 (2010).
- [55] P. Eastham, N. Cooper and D. Lee, *Phys. Rev. Lett.* **105**, 236805 (2010).
- [56] L. Tiemann, Dissertation, University of Bielefeld, 2008.
- [57] W. Eisenmenger, hrsg. von W. P. Mason and R. N. Thurston (Academic Press, ADDRESS, 1976).
- [58] A. Finck, A. Champagne, J. Eisenstein, L. Pfeiffer and K. West, *Phys. Rev. B* **78**, 075302 (2008).

- [59] I. Spielman, Dissertation, California Institute of Technology, 2004.
- [60] K. Yang, Phys. Rev. B **58**, R4246 (1998).
- [61] J. Su and A. MacDonald, Nature Physics **4**, 799 (2008).
- [62] A. Finck, J. Eisenstein, L. Pfeiffer and K. West, Phys. Rev. Lett. **106**, 236807 (2011).
- [63] A. Finck, J. Eisenstein, L. Pfeiffer and K. West, Phys. Rev. Lett. **104**, 016801 (2010).
- [64] R. Mani, Europhysics Letters **36**, 203 (1996).
- [65] L. Tiemann, J. Lok, W. Dietsche, K. von Klitzing, K. Muraki, D. Schuh and W. Wegscheider, Physical Review B **77**, 033306 (2008).
- [66] A. Fronius, H. Fischer and K. Ploog, Journal of Applied Physics **25**, 137 (1986).
- [67] N. Braslau, Thin Solid Films **104**, 391 (1983).

# Acknowledgements

Through this opportunity, I'd like to thank all people who contributed directly or indirectly to the realization of this work. Without their support, it wouldn't have come true.

First of all, I'd like to thank Prof. Klaus von Klitzing for accepting me as a PhD student in this dynamic and exciting department. Our interesting and stimulating discussions always ended up in new ideas. From his sharp and critical views I learned to focus on the essential issues in the midst of details.

I want to thank Prof. Werner Dietsche for giving me the chance to join his group. His patience in times when things did not work out so well and his useful suggestions were essential in solving almost all technological problems. I'm indebtedly grateful for his support in my entire time at the institute.

I thank Prof. Bernd Rosenow for being my external supervisor and for his in-depth knowledge and ideas in explaining new findings.

I want to thank Prof. Tilman Pfau for being the second referee and Prof. Alejandro Muramatsu for being the chairman of my doctoral exam.

Special thanks go to Dr. Timo Hyart, from whose theoretical understanding of bilayer physics I benefited a lot.

I want to thank Prof. Allan MacDonald, Prof. Zyun F. Ezawa and Dr. Paul Eastham for stimulating conversations. I also thank Prof. Yongqing Li for the opportunity to visit the IOP and for his useful advices.

I thank all (former and current) members of the Dietsche group: Dr. Lars Tiemann for introducing the topic and the experimental basics to me; Maik Hauser for continuously growing excellent samples; Dr. Stefan Schmult and Dr. Youngsoo Yoon for sharing their expertise; Anastasia Valet for improving my French; Prof. Madeleine Msall for improving my presentation and writing skills; and finally, Dr. Jun Chen for his help as well as for our very stimulating conversations about physics and many other topics.

I want to thank our technician team, especially Marion Hagel for her excellent sample fabrication; special thanks also to Ulrike Waizmann, Achim Güth and Thomas Reindl for keeping the working atmosphere pleasant.

I thank the entire Jurgen Smet group for their help and support: Dr. Jurgen Smet for the

Friday discussions and for keeping me awake by suddenly showing up in my lab; Ding Zhang for our numerous conversations and sharing his insights both in physics and in graphics; Dr. Johannes Nübler for helping with dilution fridge, proofreading this manuscript and teaching me how to ski; Thomas Beringer for his help in various situations.

I also thank the entire Jürgen Weis group for their help and support: Prof. Jürgen Weis for helps in diverse things; Max Köpke for our interesting discussions as well as for his help during my application process; Konstantinos Panos, Marcel Mausser, Leonhard Schulz, Markus Rommel, Andreas Gauß and Jochen Weber for the nice working atmosphere.

I thank Ruth Jenz for her permanent readiness and capability to handle all the organizational issues.

Apart from the vK department, I also want to express my thanks to other people I got to know in this institute, especially: Andreas Eberlein for our friendship; Dr. Chilin Li for the many useful advices.

I want to thank my high school best friend, Di Niu, for being my friend for the last sixteen years; my fellow students from the TU München, Dr. Sebastian Neusser and Andreas Wild, for our good time in Munich and their help; my fellow believers and friends, especially Gefei Fu, Jiangyan Li, Ruth Schumacher, Jian Zhang, Zhe Lin, Qingyun Li, family Hui and family Roth, for encouraging me in faith.

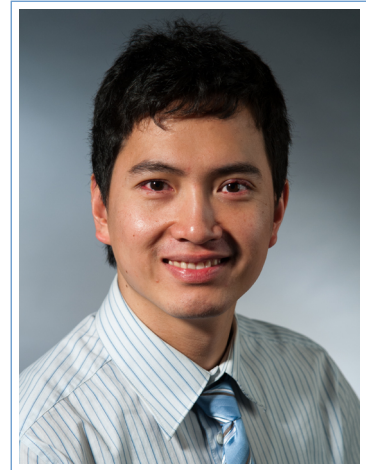
I want to thank my brother and sister, for their help and support and for the joyful moments they keep bringing me with their children. I also thank my entire family for the care and support in the past.

I'm most grateful to my parents, who have enabled me everything in my life. They have always been supporting me with and without words. Dear parents, your love is always a source of energy for me to become better.

I want to thank Renate, for her patience, support and care which wouldn't be possible without her love. Thank you also for introducing to me the healthier life style.

Finally, I want to thank my Lord and Savior, Jesus Christ, for everything.

# Lebenslauf



---

## Persönliche Daten

Name Xuting Huang  
Geburtsdatum 20.12.1982  
Geburtsort Guang Dong, China

---

## Ausbildung

2008-2012 Promotion  
Max-Planck-Institut für Festkörperforschung, Stuttgart  
2003-2008 Physikstudium  
Technische Universität München  
2006-2007 Physikstudium  
École Polytechnique Fédérale de Lausanne  
2002 Vorbereitungsstudium  
Studienkolleg München  
2001-2002 Physikstudium  
Harbin University of Science and Technology  
1995-2001 Chinesische Hochschulreife  
Shenzhen Experimental School



## Erklärung

des Doktoranden

Name:

Mit der Abgabe der Dissertation versichere ich, dass ich, abgesehen von den ausdrücklich bezeichneten Hilfsmitteln und den Ratschlägen von jeweils namentlich aufgeführten Personen, die Dissertation selbständig verfasst habe.

.....  
(Ort, Datum)

.....  
(Unterschrift)